MODELING OF GAMMA RAYS STREAMING THROUGH STRAIGHT RECTANGULAR DUCTS

by

KYLE RICHARD THOMPSON

B. S., Kansas State University, 1983

A MASTER'S THESIS

submitted in partial fulfillment of the

requirements for the degree

MASTER OF SCIENCE

Department of Nuclear Engineering

KANSAS STATE UNIVERSITY
Manhattan, Kansas

1985

Approved by:

Major Professor

LD
2668
.T4
1985
T476
c.2

TABLE OF CONTENTS

A11202 985647

Page

LIST OF FIGURES iii

LIST OF TABLES vi

1.0 INTRODUCTION 1

2.0 REVIEW OF DUCT STREAMING EXPERIMENT 5

2.1 Experimental Duct Configurations 5
2.2 Experimental Duct Wall Specifications 6
2.3 Gamma-Ray Sources used in the Experiment 11
2.4 The Gamma-Ray Detector used in the Experiment 20
2.5 Experimental Geometry 20
2.6 Experimental Data Reduction 22

3.0 DEVELOPMENT OF GAMMA-RAY STREAMING MODELS 25
3.1 Description of Gamma-Photon Interactions 26
3.1.1 Total Attenuation Coefficient for Concrete . . 28
3.1.2 Dosimetric Response Function 28
3.1.3 Klein-Nishina Scattering Cross Section 32
3.1.4 Buildup Factor 33
3.1.5 Albedo Formulation for Scattered Photons . . . 36
3.2 Direct Penetration Component 38
3.3 Lip Scattered Component 43
3.3.1 Expsoure Rate Contribution from the Near Lip 48
3.3.2 Exposure Rate Contribution from the Far Lip 53
3.3.3 Exposure Rate Contribution from the Top Lip 57
3.3.4 Exposure Rate Contribution from the Bottom Lip 60
3.4 Wall Scattered Component 60
3.4.1 Exposure Rate Contribution from Wall #1 61
3.4.2 Exposure Rate Contribution from Wall #2 65
3.4.3 Exposure Rate Contribution from the Top of the Duct 70
3.4.4 Exposure Rate Contribution from the Bottom of the Duct 73
3.5 Multiple Scattering from the Duct Walls 73
3.5.1 Exposure Rate Contribution from Double-1 Scatters 75
3.5.2 Exposure Rate Contribution from Double-2 Scatters 78

4.0 MODEL REFINEMENTS AND COMPARISONS TO EXPERIMENT 80
4.1 Prediction of Experimental Reduced Data 81
4.2 Correction for a Finite Sized Detector 83

Page

4.3 Buildup-Correction Factors 84
4.4 Elimination of Models Providing Insignificant Contributions. 87
4.5 Comparison of the Single-Scatter and Albedo Models. 88
4.6 Characteristics of the Principal Model Components 89
4.7 Compairson of the Models to the Experimental Data. 100
4.8 Effect of Duct Geometry on Transmitted Radiation. 103

5.0 CONCLUSIONS, MODEL LIMITATIONS, AND RECOMMENDATIONS FOR FURTHER STUDY 111
5.1 Conclusions. 111
5.2 Model Limitations. 112
5.3 Recommendations for Further Study. 113

6.0 ACKNOWLEDGEMENTS. 114

7.0 REFERENCES. 115

APPENDIX A 116

APPENDIX B 135

LIST OF FIGURES

Figure		Page
2.1	Experimental arrangement used in the Kansas State University gamma ray streaming experiment.	7
2.2	Concrete block stacking pattern used for the 50.8 cm thick duct walls	9
2.3	Duct wall in which the rectangular ducts were constructed.	10
2.4	Location of the 10 Ci gamma ray source in relation to the top of the J. L. Shepherd and Associates irradiator unit.	12
2.5	Dimensions of the lead collimator.	14
2.6	Shadow shield dimensions and position in relation to the source and collimator.	15
2.7	Collimator and shadow shield positions in relation to the source and irradiator unit top . . .	16
2.8	Collimation angles formed from the source, collimator, and shadow shield.	17
2.9	Illustration of the collimated beam shape and its dimensions	18
2.10	Experimental geometry used in the gamma-ray streaming experiment	21
3.1	General geometry used in the model development . . .	27
3.2	Scattering geometry used in the albedo formulation.	37
3.3	Illustration of the geometry used in the formulation of the direct penetration component.	39
3.4	Illustration of the possible paths directly penetrating radiation can have	42
3.5	Example of lip scatters.	44
3.6	Illustration of the geometry used in the formulation of the near lip 1 component.	49

Figure		Page
3.7	Comparison of the exposure rates predicted from Eq. (3.48) (dashed line) and Eq. (3.32) (solid line). The exposure rates are presented as reduced data, i.e., $\dot{X}\ \rho^2$/source strength.	54
3.8	Illustration of the geometry used in the formulation of the far lip component	55
3.9	Illustration of the top lip scattering geometry. . .	58
3.10	Scattering geometry used in the wall #1 component. .	62
3.11	Scattering geometry used in the wall #2 component. .	66
3.12	Illustration of the transparent corner used in the albedo formulation of the wall #2 component. . .	69
3.13	Scattering geometry used in the top of the duct scattering component	71
3.14	Illustration of the double-1 scattering geometry . .	74
3.15	Illustration of double-2 scattering geometry	76
4.1	Graphical comparison of the single-scatter and albedo modeling techniques. (Source angle = 33 degrees and Bc = 0)	90
4.2	Graphical comparison of the single-scatter and albedo modeling techniques. (Source angle = 45 degrees and Bc = 0)	91
4.3	Graphical comparison of the single-scatter and albedo modeling techniques. (Source angle = 60 degrees and Bc = 0)	92
4.4	Graphical comparison of the single-scatter and albedo modeling techniques. (Source angle = 33 degrees and Bc = 1)	93
4.5	Graphical comparison of the single-scatter and albedo modeling techniques. (Source angle = 45 degrees and Bc = 1)	94
4.6	Graphical comparison of the single-scatter and albedo modeling techniques. (Source angle = 60 degrees and Bc = 1)	95
4.7	Illustration of the contributions of the various model components (source angle = 33 degrees)	97

Figure		Page
4.8	Illustration of the contributions of the various model components (source angle = 45 degrees)	98
4.9	Illustration of the contributions of the various model components (source angle = 60 degrees)	99
4.10	Variation of the reduced data exposure rate fields as a function of the detector x-coordinate and source angle with the detector z-coordinate equal to 201.6 cm.	105
4.11	Variation of the reduced data exposure rate fields as a function of the detector x-coordinate and source angle with the detector z-coordinate equal to 251.6 cm.	106
4.12	Variation of the reduced data exposure rate fields as a function of the detector x-coordinate and source angle with the detector z-coordinate equal to 351.6 cm.	107
4.13	Variation of the reduced data exposure rate fields as a function of the detector x and z-coordinates with the source angle equal to 33 degrees	108
4.14	Variation of the reduced data exposure rate field as a function of the detector x and z-coordinates with the source angle equal to 45 degrees	109
4.15	Variation of the reduced data exposure rate fields as a function of the detector x and z-coordinates with the source angle equal to 60 degrees	110

LIST OF TABLES

Table		Page
2.1	Summary of straight rectangular duct configurations.	8
2.2	Cobalt-60 source strengths, effective 1 June 1979 . .	11
2.3	Dimensions of collimated beam at perpendicular distance X from the collimator face	19
2.4	Collimation angles.	19
2.5	Estimated percentage error in the reduced data for various differences in solid and ducted measurements.	24
3.1	A fit to the total attenuation coefficient for concrete.	29
3.2	A fit to the linear energy absorption coefficient for air	31
3.3	Comparison of Eisenhauer and Simmons buildup factors	34
4.1	Buildup correction factors determined for various duct configurations and detector locations	85
4.2	Correlation coefficients and R^2 statistics for various duct configurations and detector locations	102

CHAPTER 1

INTRODUCTION

The calculation of the radiation fields resulting from gamma-rays streaming through straight rectangular ducts is a problem that presents itself frequently in the design and analysis of radiation shields. Current solutions to this problem are usually complex computer codes based on Monte Carlo, albedo, and ray-analysis techniques. These codes generally require the use of large main-frame computers and are expensive to run. Simpler solutions to the gamma ray streaming problem are almost always restricted to the unrealistic conditions of either a plane or point gamma-ray source located at the duct entrance and a detector located at the center of the duct exit. Such simple solutions provide little flexibility for realistic source and detector locations and thus have limited usefulness.

Several simple modeling techniques have been developed to describe gamma-rays streaming through ducts. Simplest among these is the method suggested by Rockwell [1] which states that the gamma flux escaping the duct depends only on the geometry of the duct and the angular distribution of the source and that the model need not consider gamma-ray interactions or duct wall materials. Methods suggested by other authors [2-4] are slightly more complex and involve separating the duct streaming phenomena into different components, each of which is separately calculated.

LeDoux and Chilton [2] (whose primary duct work concerned two legged or L-shaped ducts) considered the problem as composed of two separate phenomenon, photons scattering from the duct walls and photons scattering from a duct lip region. LeDoux and Chilton used empirically

derived albedos (ratios of reflected to incident radiation) to calculate the exposure contributions due to backscatter from the different reflecting areas within a duct (i.e., the duct walls). For the lip region, LeDoux and Chilton proposed a technique which analytically integrated all single scatter photon interactions that occur in the lip region and contribute to the streaming radiation and which represented these scattered photons as being emitted at an equivalent single scatter point.

Kitazume et al. [3], in a study of gamma-ray streaming through straight cylindrical ducts, suggested, like LeDoux, that the gamma-ray streaming problem be decomposed into two phenomena. However, unlike LeDoux, Kitazume considered the two phenomena to be photons that directly penetrated the duct wall, and photons that scatter from the duct walls. Kitazume calculated the directly penetrating photon contribution using a ray-analysis technique (an analysis method which assumes that the transmission of a shield can be computed as if transmission along various paths were affected only by material which lies along that path). A semi-analytical Monte Carlo albedo method was used to describe the photon wall scatters.

Clifford [4], in a study of gamma-rays streaming through straight principally cylindrical ducts, divided the gamma-ray streaming problem into three different phenomena. These three phenomena are (i) photons that directly penetrate the duct wall, (ii) photons that scatter from duct walls, and (iii) photons that scatter from a duct lip region. Clifford treated the directly penetrating photons in a manner similar to that used by Kitazume. For the photons scattered from the duct wall, Clifford developed a new approach in which all photons scattering from a

duct wall were assumed to scatter from one effective point in the wall. To determine the number of photons scattering from this point that contribute to the streaming dose, Clifford integrated the number of photons incident upon the duct wall which scatter, on a line extending from the scatter point into the wall, to the gamma-ray detector. For the photons that scatter from a duct lip, Clifford used a method similar to that used by LeDoux.

In this work, a simple model will be developed to describe the radiation fields resulting from gamma rays streaming through straight rectangular ducts obliquely illuminated by monoenergetic photons. This new model is designed to be used with a small micro computer and to offer a large degree of flexibility. The model will allow for duct configurations with variations in the duct dimensions, as well as changes in the source and detector positions. Specifically, the model will be designed to emulate duct configurations in which a point gamma ray source obliquely illuminates the duct entrance and a point detector traverses the area on the exit side of the duct.

During the modeling process, single and multiple scattering, as well as direct penetration photon transmission phenomena will be addressed. In particular, the gamma-rays streaming through the duct will be divided into four groups or types. These groups are (i) directly penetrating photons, (ii) photons scattered from the duct lips, (iii) photons scattered from one of the duct walls, and (iv) photons which scatter between two duct walls. Two different techniques for modeling the contribution of the singly scattered photons to the overall gamma ray streaming radiation field are presented. One technique used to describe the single photon scatters is a modified version of

Clifford's lip-scatter method. The second technique is an albedo-based method that uses an empirical albedo formula.

The models developed in this work are compared to benchmark experimental data to test their validity. These experimental data were obtained from a gamma ray streaming experiment conducted earlier by the Department of Nuclear Engineering at Kansas State University. However, in order to make such a comparison, the duct model had to be altered slightly to describe the actual experimental conditions as closely as possible.

A brief description of the duct streaming experiment will be presented in Chapter 2. The development and description of the gamma-ray streaming models are then given in Chapter 3. In Chapter 4 the models are refined and compared to the experimental data. Included in these refinements are modifications to emulate the conditions of the KSU experiment, as well as, to eliminate model components that prove insignificant to the transmitted radiation field. The results of Chapter 4 also include a comparison of the predictions obtained from both the point-scatter and albedo models to the experimental data.

It is this author's belief that the model presented will be both reasonably accurate and economic to use for engineering analysis of gamma-ray streaming problems. Moreover, as discussed in Chapter 5, it appears that these models can readily be generalized to more complex duct geometries (e.g., cylindrical ducts, and detector and source at different elevations).

CHAPTER 2

REVIEW OF DUCT STREAMING EXPERIMENT

An extensive experimental program focusing on gamma ray streaming through straight ducts in concrete walls was conducted by the Department of Nuclear Engineering at Kansas State University (1979-1980). The outcome of this program was a large volume of data which could be used in the development of simplified models describing gamma ray streaming through ducts. This data represents the exposure rate fields produced by collimated Co-60 gamma rays obliquely incident upon ducts in a variety of configurations. Included in these different duct configurations were variations in duct length, size, and type, as well as multiple source strengths and positions.

Following is a brief description of the experimental program. A detailed report of the experiment can be found in references 4, 5, and 6.

2.1 Experimental Duct Configurations

Many duct configurations were used in the experiment. Two Co-60 gamma ray sources were employed throughout the experiment. These Co-60 sources were positioned atop a large irradiator unit. Due to the size of the irradiator unit the sources were restricted to movement in a horizontal plane (i.e., the source elevation did not vary). During the course of the experiment three concrete walls of different thicknesses (50.8, 101.6, and 152.4 cm) were constructed. In these walls straight cylindrical and rectangular ducts were formed. These ducts were oriented perpendicularly to the duct wall and had their centerline at

the same height as the sources. A detector measuring the gamma ray streaming exposure rate traversed the volume on the exit side of the duct. Figure 2.1 shows the general experimental arrangement.

The configurations to be considered in this study are restricted to rectangular ducts and detector traverses on the horizontal plane at the duct centerline elevation. Because of these restrictions, only experimental data for the 101.6 cm thick wall was available. Table 2.1 contains a summary of the various duct configurations that will be considered in developing the gamma ray streaming models in Chapter 3.

2.2 Experimental Duct Wall Specifications

The 101.6 cm thick duct wall was constructed as a combination of two 50.8 cm thick walls stacked next to one another. These thinner walls were formed of stacked rectangular blocks composed of ordinary concrete. The blocks were stacked in the pattern shown in Fig. 2.2. The two 50.8 cm walls were offset slightly so that the cracks between the blocks did not penetrate both walls. The wall dimensions are shown in Fig. 2.3.

A square void penetrating perpendicularly through the walls served as the "duct area". Different sized ducts could be formed by filling this duct area with varying sizes and shapes of concrete blocks. During the formation of the different ducts, care was taken to maintain the same duct centerline.

The concrete blocks were constructed of ordinary concrete. This concrete was composed of 300 kg cement per cubic yard of sand and aggregate (30 weight percent heavy aggregate and 70 percent sand). The concrete blocks were determined to have an average specific gravity of

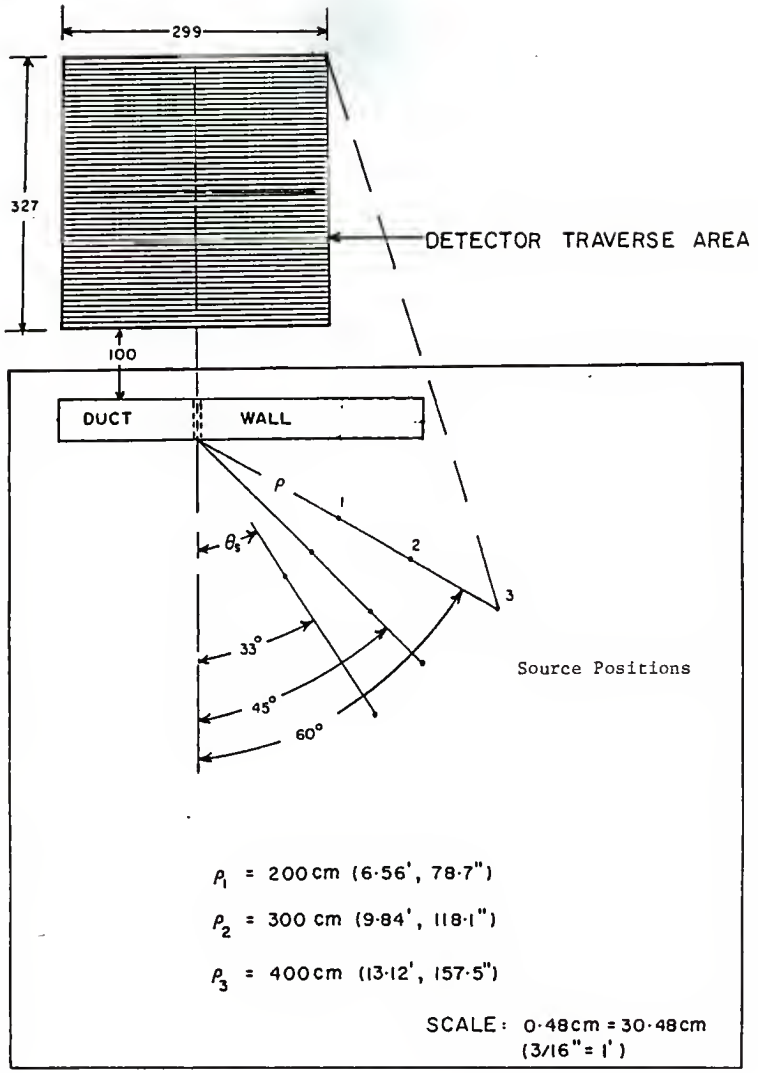

Fig. 2.1. Experimental arrangement used in the Kansas State University gamma ray streaming experiment. (all dimensions in centimeters)

Table 2.1 Summary of straight rectangular duct configurations (duct length is 101.6 cm and detector is at duct centerline elevation).

Source Strength (Ci)	Source Angle, θ_s * (degrees)	Source Dist.** (cm)	Duct Width (cm)	Duct Height (cm)
0.5	33	200	30.5	30.5
0.5	45	200	30.5	30.5
0.5	60	200	30.5	30.5
0.5	33	200	30.5	15.25
10	45	300	30.5	15.25
10	60	200	30.5	15.25

* Angle formed between duct center line and line from source to center of duct opening.

** Distance from source to center of duct opening.

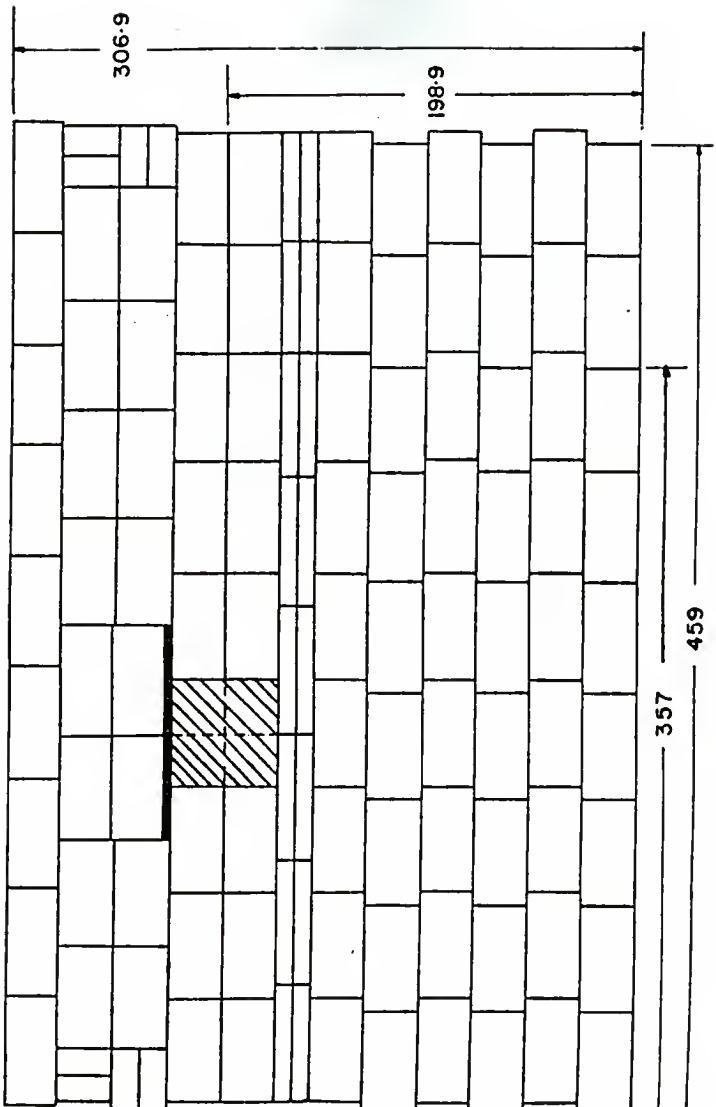

Fig. 2.2. Concrete block stacking pattern used for the 50.8 cm thick duct walls. (all dimensions in centimeters)

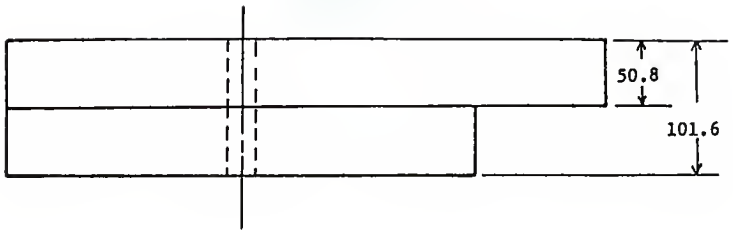

Top View

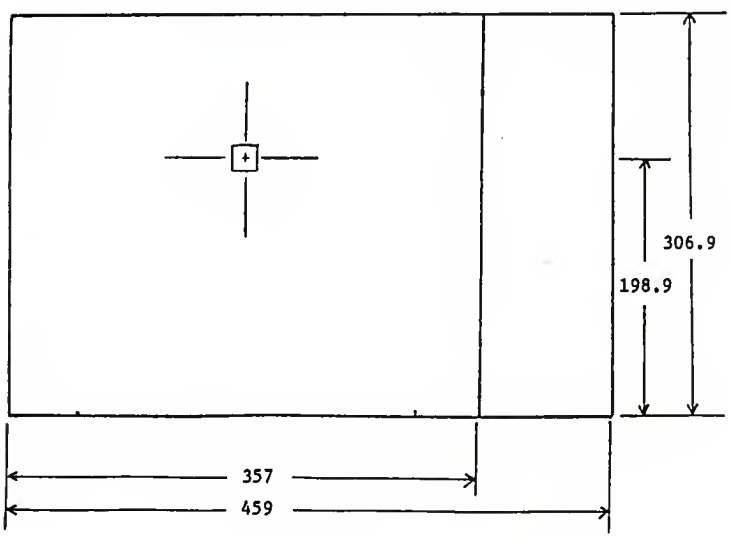

Front View

Fig. 2.3. Duct wall in which the rectangular ducts were constructed. (all dimensions in centimeters)

2.22 ± 2.1% [5]. This value was determined from weight and volume measurements of a representative sample of the blocks.

2.3 Gamma-Ray Sources Used in the Experiment

Two gamma ray sources, nominally 0.5 Ci and 10 Ci, were used in the experiment. The 10 Ci source was housed in a lead-shielded irradiator unit manufactured by J. L. Shepherd and Associates. When needed, the 10 Ci source was pneumatically raised and positioned 2.22 cm above the top of the irradiator and 5.08 cm from the irradiator's vertical centerline (see Fig. 2.4). When the 0.5 Ci source was used, it was placed in a wooden frame and mounted on the irradiator unit in a position identical to that used by the larger source.

The sources were in the shape of right cylinders and were positioned on their vertical axes. The 10 Ci gamma ray source was triply encapsulated in stainless steel (type 304) with a wall thickness of 0.264 cm and base thickness of 0.244 cm. The 10 Ci source dimensions (before encapsulation) were 0.693 cm in diameter and 0.635 cm long. The 0.5 Ci gamma ray source was a pencil source contained in a Technical Operations, Inc. Model 402 Gamma-Ray Projector [5].

The actual source strengths of the two sources are presented in Table 2.2.

TABLE 2.2 Cobalt-60 Source Strengths, effective 1 June 1979 [5].

Nominal Source Strength (Ci)	Actual Source Strength (Ci)
0.5	0.474 ± 4.5%
10	8.12 ± 4.8%

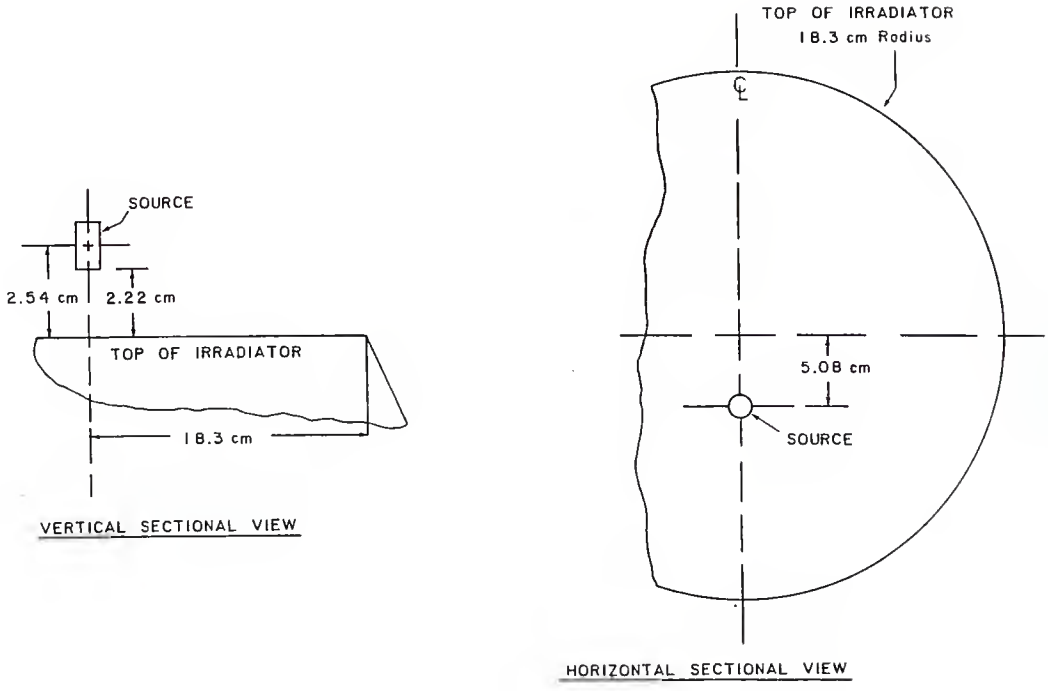

Fig. 2.4. Location of the 10 Ci gamma ray source in relation to the top of the J. L. Shepherd and Associates irradiator unit.

In order to eliminate skyshine (photons that scatter from the air around the source) and other unwanted scattered radiation from reaching the detector, both a collimator and shadow shield were employed. These devices caused the source gamma rays to be emitted in a narrow beam which illuminated the duct mouth. They were constructed of lead bricks (20.32 cm x 10.16 cm x 5.08 cm). The collimator and shadow shield dimensions are illustrated in Figs. 2.5 and 2.6, respectively. The collimator and shadow shield were placed on top the source irradiator unit with the collimator centerline displaced horizontally 2.54 cm from the irradiator centerline. (Note: The collimator was displaced because of physical limitations imposed by an unused source orifice at the irradiator's vertical centerline.) Figure 2.7 shows the top view of the collimator and shadow shield and their positions in relation to the source.

The degree or amount of collimation imparted by the collimator and shadow shield is determined from their dimensions, as well as those of the sources used. This degree of collimation can be expressed using collimation angles (angles describing the collimated beam shape based on the beam centerline). These collimation angles are illustrated in Fig. 2.8. The collimation angles were determined from measurements of the beam's cross section at various distances from the irradiator. Figure 2.9 shows the distances that were measured in the determination of the collimation angles. The measurements are presented in Table 2.3, and the resulting collimation angles are shown in Table 2.4. The average collimation angles presented in Table 2.4 insured that the duct mouth and surrounding area would be illuminated for all the different duct configurations.

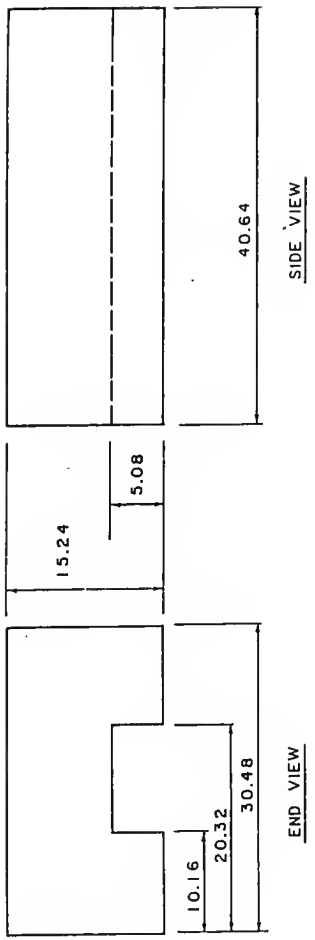

Fig. 2.5. Dimensions of the lead collimator.
(all dimensions in centimeters)

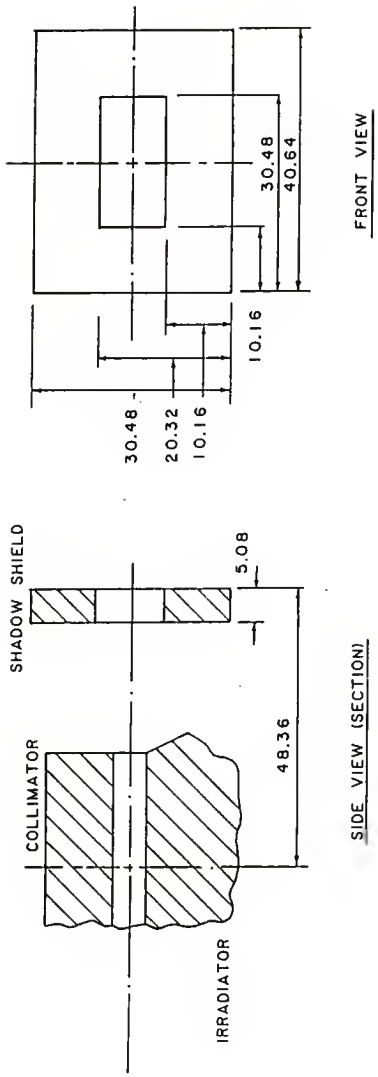

Fig. 2.6. Shadow shield dimensions and position in relation to the source and collimator. (all dimensions in centimeters)

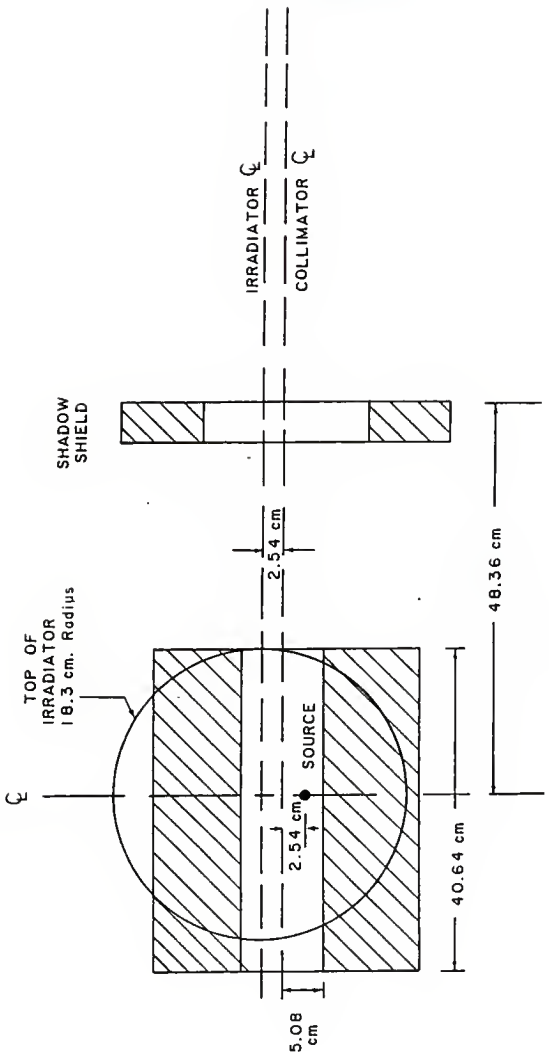

Fig. 2.7. Collimator and shadow shield positions in relation to the source and irradiator unit top.

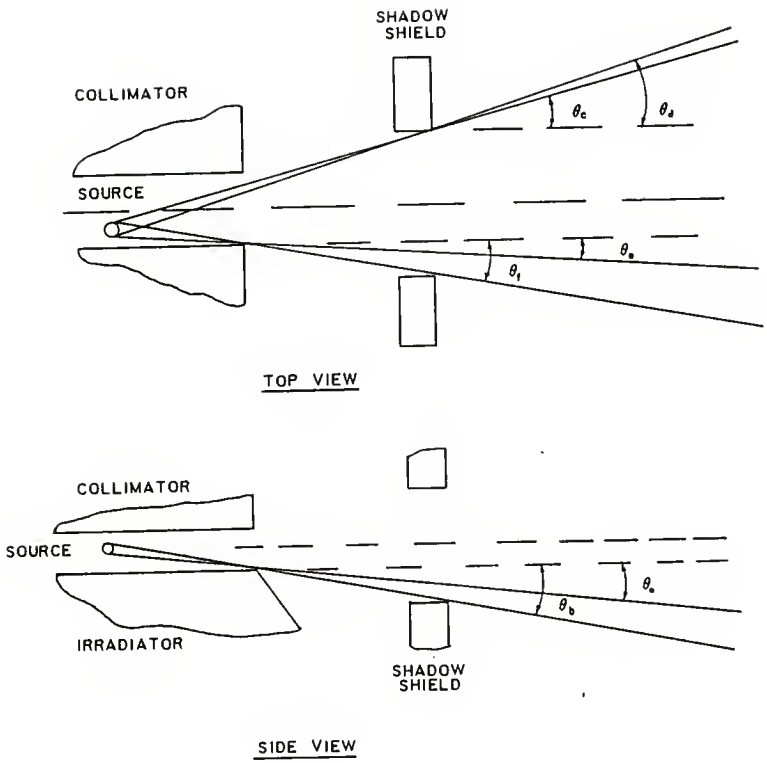

Fig. 2.8. Collimation angles formed from the source, collimator, and shadow shield.

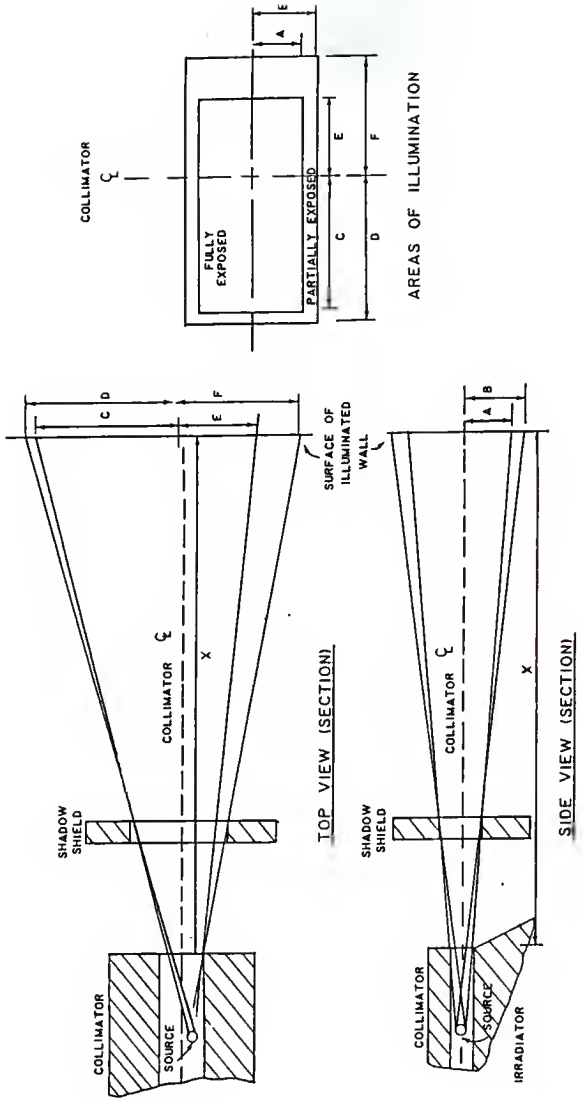

Fig. 2.9. Illustration of the collimated beam shape and its dimensions.

Table 2.3 Dimensions of collimated beam (in cm) at perpendicular distance X from the collimator face. Refer to Fig. 2.9 for definitions of dimensions.

X (cm)	A	B	C	D	E	F
91.44	13.46	17.27	41.40	44.96	16.00	19.56
121.9	17.02	22.10	53.59	58.42	19.81	24.38
182.9	24.38	31.75	77.98	84.84	27.18	34.04
243.8	31.75	41.40	102.4	111.5	34.29	43.69
304.8	38.86	51.31	126.5	138.2	41.66	53.34
457.2	57.15	74.17	187.2	204.7	59.94	77.47
609.6	75.44	99.82	247.9	271.0	78.23	101.6

Table 2.4 Collimation angles (in degrees). See Fig. 2.8 for angle definitions.

X (cm)	θ_a	θ_b	θ_c	θ_d	θ_e	θ_f
91.44	7.00	8.97	20.68	22.29	8.30	10.11
121.9	6.92	8.96	20.92	22.62	8.04	9.86
182.9	6.91	8.97	21.19	22.87	7.70	9.61
243.8	6.91	8.98	21.33	23.04	7.45	9.46
304.8	6.86	9.02	21.38	23.15	7.35	9.38
457.2	6.85	8.87	21.49	23.30	7.19	9.26
609.6	6.85	9.03	21.55	23.35	7.10	9.19
AVERAGE	6.90	8.97	21.22	22.95	7.59	9.55

2.4 The Gamma-ray Detector used in the Experiment

A sensitive high pressure ionization chamber ("HPIC") and its associated electronics were used to measure the radiation fields resulting from the streaming gamma rays. The HPIC was a Reuter-Stokes RSS-111 Area Monitor System calibrated by the manufacturer with Co-60 gamma rays to read directly in units of μR/h. (Note: Graphic output from the detector system was calibrated in units of μR/h. Digital output was in units of mV.) [5] A spherical (25.4 cm diameter) ion chamber with 0.30 cm thick stainless steel walls was used in the system. The chamber was filled with high-purity argon at a pressure of 25 atmospheres (2.5 MPa) at 0° C. The center electrode of the ion chamber was an aluminum sphere 5.08 cm in diameter. A 0.24 cm thick aluminum weather housing enclosed the system [7].

In order to obtain air equivalent exposure rate measurements (from the detector system digital output), the voltage readings from the detection system were multiplied by a correction factor of 0.25, i.e.,

$$\dot{X} = 0.25 \text{ (Measured instrument output voltage mV)}$$

where $\dot{X}$ is the exposure rate in units of μR/h. This correction factor took into account the energy sensitivity of the detector, a correction for the surrounding buildings and a voltage-to-exposure rate conversion factor [5].

2.5 Experimental Geometry

Figure 2.10 shows the geometry used in the experiment. The source position was defined by a two dimensional polar coordinate system (ρ,θ_s) with the origin located at the center of the duct entrance. The elevation of the source was at all times equal to that of the duct

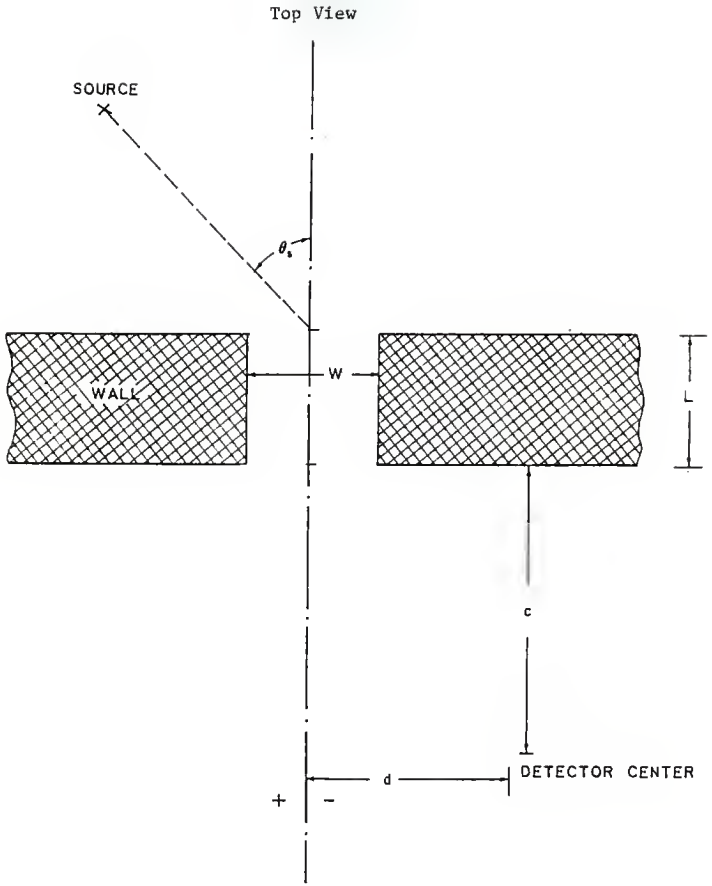

Fig. 2.10. Experimental geometry used in the gamma-ray streaming experiment.

centerline. The detector, on the other hand, employed all three dimensions in defining its location throughout the experiment. Two variables of the detector position, c and d, are illustrated in Fig. 2.10. The variable not shown is the detector elevation. This variable was measured from the duct centerline with measurements below the centerline being negative. Lastly, the duct size was defined by simple length (L), width (W), and height (H) variables. (Note: The duct height is not shown in the top view of Fig. 2.10).

2.6 Experimental Data Reduction

The exposure rate data obtained from the experimental program is meant to describe only the effect of a duct in a shielding wall, not the shielding properties of the wall itself. In order to produce data of this type ("reduced data"), exposure rate measurements were obtained with and without a duct in the wall. The difference between these two measurements were reported and referred to as "reduced data" [5]. These reduced data were then normalized to unit source strength and multiplied by the source distance squared (ρ^2) to account for the inverse-square geometrical attenuation between source and duct entrance. Multiplying by ρ^2 is not a theoretically correct method for eliminating the inverse-square geometrical attenuation of the source. But, if it is assumed that the area immediately surrounding the duct entrance acts as the source of the majority of the radiation measured as reduced data and that this area subtends a small solid angle from the source, then multiplying by ρ^2 should prove to be a good approximation. The resultant reduced data has units of m^2 μR/Ci h. It is these data that are used in this study to test various models for predicting the radiation field transmitted by the duct.

The amount of error involved in the reduced data is reported to vary with the differences in the duct and solid wall exposure rate measurements [5]. Large differences have small associated uncertainties and small differences have large uncertainties. Table 2.5 illustrates the error that can be associated with the reduced data. The error for large differences in the ducted and solid wall exposure rates is due almost entirely to the uncertainty in the source strengths (4.5% to 4.8%) and the source distance (< 0.5%).

Table 2.5 Estimated percentage error in the reduced data for various differences in solid and ducted measurements [5].

Ducted Wall Measurement - Solid Wall Measurement (μR/hr)	Percent Error in Reduced Data
10	29.1
25	13.3
50	8.9
100	7.9
300	7.0
500	6.9

CHAPTER 3

DEVELOPMENT OF GAMMA-RAY STREAMING MODELS

The calculation of the radiation fields resulting from gamma-rays streaming through straight rectangular ducts is becoming increasingly important in the design of shields used in modern nuclear reactors. Several methods for performing these calculations have been developed. Many of these methods result in very complex computer codes, requiring large amounts of computer time on mainframe-sized computers. The potential accuracy afforded by these complex codes is not needed for all areas of shielding analysis, i.e., preliminary design studies and on-site health physics calculations. From this arises the need for simple engineering models that can estimate the gamma radiation streaming through ducts and be evaluated on small micro-computers. Rockwell [1], LeDoux et al. [2], and Kitazume et. al. [3] have all studied the gamma ray streaming problem, presenting simplified Monte Carlo, albedo, and ray-analysis techniques which are thought to be useful. Invariably, however, these studies have been restricted to cases where the source is located in the center of the duct entrance and the detector is located in the center of the duct exit.

In this chapter a duct-streaming model is developed that is based upon the use of a distant collimated point source obliquely illuminating the duct entrance and a point detector traversing the area on the exit side of the duct. The basis for this model is the use of single scatter points to describe the single photon scatters that occur in regions near the duct entrance. As an alternative to the single scattering point methods, the albedo-based methods are also presented where applicable. The albedo-based method, which is widely used in

modeling photons streaming through ducts, will provide a standard to which the single-point scattering models can be compared. These two different approaches are then compared to each other and to experimental data in Chapter 4.

Gamma radiation transmitted through straight ducts can be divided into four components, namely, 1) directly penetrating radiation, 2) radiation that scatters once from the duct lips, 3) radiation that scatters from the duct walls, and 4) radiation that scatters from more than one duct wall.

The models presented in this chapter are designed specifically to describe the duct configurations listed in Table 2.1 (i.e., rectangular duct configurations used in the KSU gamma-ray streaming experiment). These configurations have the source and detector at the same elevation as the duct centerline and the source obliquely incident upon the duct mouth. Figure 3.1 shows the general geometry and some of the associated variables used in the model formulation. The source and detector positions were described using a Cartesian coordinate system with the origin at the center of the duct mouth. The parameters ρ, θ_s, c, and d used in this section are the same as the experimental variables (see Fig. 2.10).

3.1 Description of Gamma-Photon Interactions

Some elements of gamma-photon interactions that will be used throughout the model development in this chapter are: 1) an empirical fit to the total attenuation coefficient, 2) a dosimetric response function to convert the gamma flux to an exposure rate, 3) the Klein-Nishina scattering cross section, 4) an energy-dependent Berger buildup factor for a collimated source, and 5) an empirical exposure

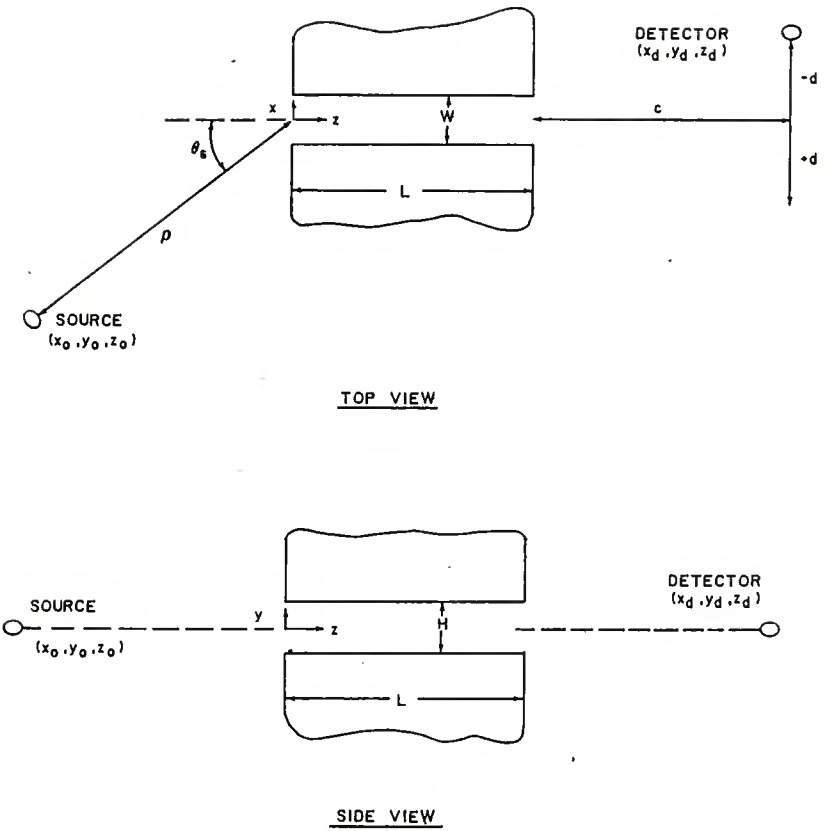

Fig. 3.1. General geometry used in the model development.

rate albedo. In the following subsections, explicit approximations of formulas for these five quantities are presented.

3.1.1 Total Attenuation Coefficient for Concrete

An energy-dependent total attenuation coefficient valid for ^{60}Co photons is required for the model development. The photon energy range of interest ranges from 1.33 MeV to around 100 keV. A least squares fit was performed [$\ell n(\mu/\rho)$ vs. $\ell n(E)$] using tabulated data for the total mass interaction coefficient [8]. This fit yielded the following equation

$$\frac{\mu(E)}{\rho} = 0.06381\ E^{-0.41851} \quad \left\{\frac{cm^2}{g}\right\} \tag{3.1}$$

where E is photon energy {MeV}, ρ is density of concrete {g cm^{-3}}, and $\mu(E)$ is total attenuation coefficient in concrete for photons of energy E.

Table 3.1 shows the data used in the fit, the values calculated using Eq. (3.1), and the percent difference between the two.

3.1.2 Dosimetric Response Function

The dosimetric response function is a factor which converts the photon flux to a dose related quantity, e.g., the exposure rate. The exposure rate $\dot{X}$ is given by

$$\dot{X} = R_X(E)\ \phi \tag{3.2}$$

where E is the photon energy {MeV}, ϕ is the photon flux of energy E {$cm^{-2}\ s^{-1}$}, and $R_X(E)$ is dosimetric response function for photons of energy E {$\mu R\ cm^2\ s/h$}.

Since one Roentgen (R) is equivalent to the creation of 2.58×10^{-4} coulombs (C) of static charge in a kilogram of dry air, and since

Table 3.1 A fit to the total attenuation coefficient for concrete.

Energy (Mev)	$(\mu/\rho)^{\#}$ $\{cm^2/g\}$	Calculated* (μ/ρ)	Percent Difference
0.1	0.166	0.167	0.6
0.15	0.138	0.141	2.2
0.2	0.124	0.125	0.81
0.3	0.107	0.106	0.93
0.4	0.0954	0.0936	1.9
0.5	0.0871	0.0853	2.1
0.6	0.0806	0.0790	2.0
0.8	0.0707	0.0700	0.99
1.0	0.0636	0.0638	0.31
1.5	0.0518	0.0538	3.9

From Reference 8

* $\mu/\rho = 0.06381\ E^{-0.41851}$

1.602×10^{-19} coulombs of static charge is formed for each ion pair in dry air, then because 33.85 eV is needed to form an ion pair in air, the response function can be determined as

$$R_X(E) = \frac{1}{2.58\times10^{-4}} \{R\ kg(air)/C\} \cdot 1.602\times10^{-19} \{C/ion\ pair\}$$

$$\cdot \frac{1}{33.85} \{ion\ pair/eV\} \cdot 10^6\{eV/MeV\} \cdot 10^3\{g/kg\} \cdot E\ \{MeV\}$$

$$\cdot \left(\frac{\mu_{en}(E)}{\rho}\right)^{air} \{cm^2/g(air\} \cdot 10^6\{\mu R/R\} \cdot 3600\ \{s/h\}.$$

Simplifying, one obtains

$$R_X(E) = 66.04\ E \left(\frac{\mu_{en}(E)}{\rho}\right)^{air} \tag{3.3}$$

where $\left(\frac{\mu_{en}(E)}{\rho}\right)^{air}$ is the energy-dependent linear energy absorption coefficient with units $\{cm^2\ g^{-1}\}$.

To obtain an explicit energy-dependent expression for $R_X(E)$, a least-squares third-order polymonial fit was performed on linear energy absorption coefficient data [8]. The result was

$$\left(\frac{\mu_{en}(E)}{\rho}\right)^{air} = 0.01933 + 0.04397E - 0.05492E^2 + 0.01889E^3 \tag{3.4}$$

Table 3.2 shows the data used in the fit as well as a comparison to the predicted values. Combining Eqs. (3.3) and (3.4) then yields

$$R_X(E) = 66.04\ (0.01933 + 0.0437E - 0.05492E^2 + 0.01889E^3)\ E \tag{3.5}$$

Table 3.2 A fit to the mass energy absorption coefficient for air.

Photon Energy (MeV)	$(\mu_{en}/\rho)^{air}$ # {cm^2/g}	Calculated* Value $(\mu_{en}/\rho)^{air}$	Percent Difference
0.1	0.0227	0.0232	2.2
0.15	0.0247	0.0248	0.40
0.2	0.0265	0.0261	1.5
0.3	0.0287	0.0281	2.1
0.4	0.0294	0.0293	0.34
0.5	0.0298	0.0299	0.34
0.6	0.0295	0.0300	1.7
0.8	0.0287	0.0290	1.0
1.0	0.0278	0.0273	1.8
1.5	0.0254	0.0255	0.39

From Reference 8

* From Eq. (3.4)

3.1.3 Klein-Nishina Scattering Cross Section

The Klein-Nishina scattering cross section, $_{e}\sigma_{c}(E_o,\theta_{sc})$, is the differential scattering cross section for photons of unit energy about E_o, scattering through a unit solid angle about θ_{sc}. The Klein-Nishina cross section may be written as [9]

$$_{e}\sigma_{c}(E_o,\theta_{sc}) = \tfrac{1}{2} r_e^2 \, p[1 + p^2 - p\,(1 - \cos^2\theta_{sc})] \left\{\frac{cm^2}{sr\ electron}\right\} \quad (3.6)$$

in which

$$p = \frac{E_{sc}}{E_o} \quad (3.7)$$

and

$$E_{sc} = \frac{E_o}{1 + \frac{E_o}{0.511}\,[1 - \cos\theta_{sc}]} \quad (3.8)$$

where E_o is the energy of the photon prior to the scatter {MeV}, E_{sc} is the energy of the photon after the scatter, θ_{sc} is the scattering angle (i.e., angle between incident photon path and scattered photon path), and r_e is the classical electron radius ($r_e = 2.818 \times 10^{-13}$ cm) [9].

In the duct-model development it is useful to use the macroscopic Klein-Nishina cross section given by

$$\Sigma_k(E_o,\theta_{sc}) = {}_{e}\sigma_{c}(E_o,\theta_{sc}) \frac{\rho N_a}{A} Z \quad (3.9)$$

where ρ is the density of the scattering medium {g/cm^3}, N_a is Avogadro's number {molecules/g-mole}, A is the molecular mass {g/g-mole}, and Z is the number of electrons {electrons/molecule}. For concrete, which is principally composed of SiO_2, a value of $\frac{1}{2}$ can be used for the average (Z/A) value. Equation (3.9) can thus be written as

$$\Sigma_k(E_o,\theta_{sc}) = 0.01196\ p\ [1 + p^2 - p(1 - \cos^2\theta_{sc})]\ \rho \quad (3.10)$$

3.1.4 Buildup Factor

A buildup factor is widely used along with the uncollided flux density to describe the accumulation of secondary or scattered photons transmitted through thick materials. The buildup factor B is defined as

$$B = \frac{\text{observed dose rate}}{\text{dose rate due to uncollided radiation}}$$

or

$$B = 1 + \frac{\text{dose rate due to scattered radiation}}{\text{dose rate due to uncollided radiation}} . \qquad (3.11)$$

Throughout the following model development a modified Berger-type buildup equation is used. In this form, recommended by C. E. Clifford [4], the photon energy-dependence is shown explicitly, namely

$$B(E,\lambda) = 1 + \lambda k_1 E^{k_2} \exp[\lambda k_3 \exp(k_4 E)], \qquad (3.12)$$

where λ is the number of mean free paths traveled by the photon, E is the photon energy {MeV}, and the k_n are constants.

In order to obtain values for the constants k_n, Eq. (3.12) was fit to Eisenhauer and Simmons buildup factor data for a point isotropic source in an infinite concrete medium [10]. This fit yielded k_1 = 1.2858, k_2 = -0.4560, k_3 = 0.09739, and k_4 = -0.8319. Table 3.3 presents the Eisenhauer and Simmons data that was used in the fit, as well as values obtained with Eq. (3.12).

Equation (3.12) and its associated constants represent an infinite medium buildup factor. In order to predict photon buildup in a small concrete region for a collimated source, a modification must be made to Eq. (3.12). This modification takes the form

Table 3.3 Comparison of Eisenhauer and Simmons buildup factors (concrete medium, air response function) to values generated using Eq. (3.12) [10].

(a) Eisenhauer and Simmons

Penetration (mfp)	Energy (MeV) 1.50	1.00	.80	.60	.50	.40	.30
0.00	1.00	1.00	1.00	1.00	1.00	1.00	1.00
1.50	1.39	1.45	1.48	1.53	1.57	1.61	1.68
2.00	1.85	1.98	2.06	2.18	2.27	2.37	2.52
3.00	4.00	4.72	5.18	5.82	6.26	6.80	7.42
4.00	5.25	6.42	7.18	8.25	8.97	9.85	10.80
5.00	6.60	8.33	9.47	11.10	12.20	13.50	15.00
6.00	8.05	10.40	12.00	14.30	15.90	17.80	19.90
7.00	9.58	12.70	14.90	18.00	20.20	22.80	25.60
8.00	11.20	15.20	18.10	22.20	25.00	28.50	32.20
10.00	14.60	20.70	25.10	31.80	36.40	42.10	48.20
15.00	24.20	37.20	47.40	63.60	75.60	90.70	107.00
20.00	35.00	57.10	75.50	107.00	131.00	162.00	198.00

(b) Calculated

Penetration (mfp)	Energy (MeV) 1.50	1.00	.80	.60	.50	.40	.30
0.00	1.00	1.00	1.00	1.00	1.00	1.00	1.00
.50	1.54	1.66	1.73	1.84	1.91	2.01	2.16
1.00	2.10	2.34	2.50	2.72	2.88	3.09	3.40
2.00	3.26	3.80	4.15	4.65	5.01	5.49	6.18
3.00	4.49	5.38	5.96	6.81	7.42	8.22	9.39
4.00	5.78	7.09	7.96	9.22	10.12	11.33	13.06
5.00	7.15	8.95	10.14	11.91	13.16	14.84	17.27
6.00	8.58	10.95	12.53	14.89	16.56	18.81	22.06
7.00	10.10	13.11	15.15	18.19	20.36	23.28	27.51
8.00	11.69	15.44	18.00	21.84	24.59	28.31	33.68
10.00	15.14	20.65	24.48	30.32	34.53	40.25	48.55
15.00	25.39	37.43	46.25	60.10	70.36	84.48	105.23
20.00	38.39	61.03	78.48	106.90	128.51	158.81	204.10

Table 3.3 (Continued)

(c) The ratio of the calculated factors, using Eq. (3.12), to the Eisenhauer and Simmons buildup factors.

Penetration (mfp)	Energy (MeV) 1.50	1.00	.80	.60	.50	.40	.30
0.00	1.00	1.00	1.00	1.00	1.00	1.00	1.00
.50	1.11	1.14	1.17	1.20	1.22	1.25	1.28
1.00	1.13	1.18	1.21	1.25	1.27	1.31	1.35
2.00	1.14	1.17	1.20	1.22	1.24	1.27	1.33
3.00	1.12	1.14	1.15	1.17	1.18	1.21	1.27
4.00	1.10	1.10	1.11	1.12	1.13	1.15	1.21
5.00	1.08	1.07	1.07	1.07	1.08	1.10	1.15
6.00	1.07	1.05	1.04	1.04	1.04	1.06	1.11
7.00	1.05	1.03	1.02	1.01	1.01	1.02	1.07
8.00	1.04	1.02	.99	.98	.98	.99	1.05
10.00	1.04	1.00	.98	.95	.95	.96	1.01
15.00	1.05	1.01	.98	.94	.93	.93	.98
20.00	1.10	1.07	1.04	1.00	.98	.98	1.03

$$B(E,\lambda) = 1 + B_c \lambda k_1 E^{k_2} \exp[\lambda k_3 \exp(k_4 E)]. \tag{3.13}$$

where B_c is a "buildup-correction factor" that accounts for the source collimation and the finite dimensions of the shield. B_c is strictly an empirical factor and will be determined in Chapter 4 through comparison of the duct model to experimental data.

3.1.5 Albedo Formulation for Scattered Photons

An albedo, as referred to in gamma-ray scattering, is a measure of the reflective qualities of a surface. "Fundamentally, it expresses the ratio of the flow rate of radiation emitted from a small increment of surface to the flow rate of the radiation incident upon that surface under specific conditions." [9] The specific conditions refer to the incident direction and energy spectrum of the radiation, as well as the direction and energy of the emitted radiation. The geometric situation is illustrated in Fig. 3.2.

Chilton and Huddleston [11] reported the following semiempirical formula exposure-rate for the albedo:

$$\alpha_X(E_o,\theta_o;\theta,\psi) = \frac{C(E_o)\ {}_e\sigma_{ce}(E_o,\theta_{sc})\ 10^{26} + C'(E_o)}{1 + (\cos\theta_o/\cos\theta)} \tag{3.14}$$

where $C(E_o)$ and $C'(E_o)$ are constants dependent upon the incident photon energy and the reflecting medium, E_o is the incident photon energy {MeV}, θ_{sc} is the scatter angle, ${}_e\sigma_{ce}(E_o,\theta_{sc})$ is the Klein-Nishina energy scattering cross section, and α_X is the albedo. The Klein-Nishina energy scattering cross section is simply the product of Eqs. (3.6) and (3.7), i.e.,

$${}_e\sigma_{ce}(E_o,\theta_{sc}) = \tfrac{1}{2} r_e^2 p^2 [1 + p^2 - p(1-\cos^2\theta_{sc})]. \tag{3.15}$$

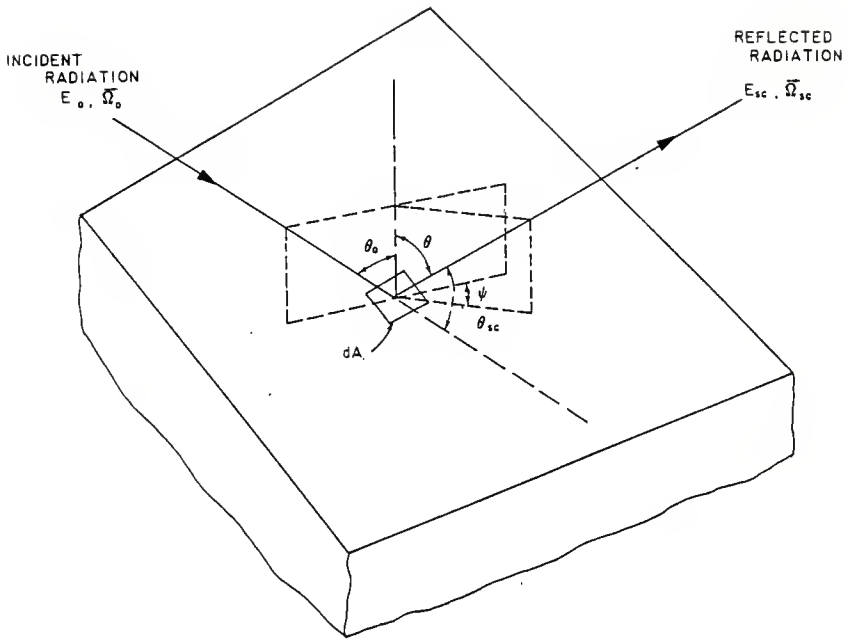

Fig. 3.2. Scattering geometry used in the albedo formulation.

The experimental incident photon energy for the present study is taken as 1.25 MeV (i.e., the average of the actual ^{60}Co source photon energies, 1.17 MeV and 1.33 MeV). Values for $C(E_o)$ and $C'(E_o)$ of 0.0586 and 0.0107, respectively, at E_o = 1.25 MeV were interpolated from values listed in reference [9].

The differential exposure rate resulting from reflected photons, expressed in terms of an albedo, is [9]

$$\dot{dX} = \frac{S_o \, R_X(E_o) \, \cos\theta_o \, \alpha_X(E_o, \theta_o; \theta, \psi) \, dA}{4\pi \, R_1^2 \, R_2^2} \tag{3.16}$$

where $\dot{dX}$ is the differential exposure, S_o is the source strength {photons/second}, $R_X(E_o)$ is the dosimetric response function evaluated at energy E_o, E_o is the initial energy of the photons, R_1 is the distance from source to scatter point, R_2 is the distance from detector to scatter point, and dA is the differential scattering area.

3.2 Direct-Penetration Component

The direct-penetration radiation is defined as the uncollided gamma rays which penetrate the duct walls. In the direct penetration component, a small amount of buildup will be associated with the directly-penetrating radiation. This associated buildup will be very small due to the fact that most of the actual buildup will be described in the gamma-ray scattering model components. The direct-penetration component can be described by using simple attenuation and buildup factor techniques. Further simplification can be achieved by restricting the source and detector to the duct centerline elevation.

Given the geometry defined in Fig. 3.3, let

x_o, y_o, z_o = source position,

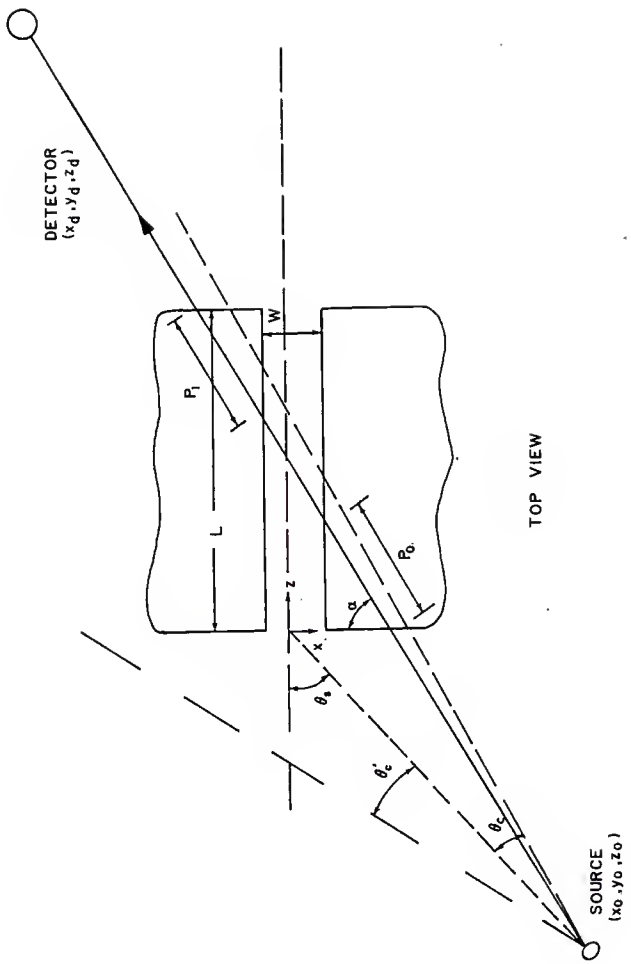

Fig. 3.3. Illustration of the geometry used in the formulation of the direct penetration component.

x_d, y_d, z_d = detector position,

S_o = source strength {photons/second},

θ_s = source angle,

θ_c and θ_c' = collimation angles,

L = length of the duct,

W = width of the duct, and

H = height of the duct (not shown in Fig. 3.3).

Since the source gamma rays are confined within the collimator angles, there is a negligible exposure rate whenever

$$\alpha < \frac{\pi}{4} - \theta_s - \theta_c' \equiv \alpha_{min} \tag{3.17}$$

or

$$\alpha > \frac{\pi}{4} - \theta_s + \theta_c \equiv \alpha_{max} \tag{3.18}$$

where

$$\alpha = \tan^{-1}\left(\frac{|z_d - z_o|}{x_o - x_d}\right) . \tag{3.19}$$

For the situation in which α is between these limits, the exposure rate resulting from the direct-penetration component can be written as

$$\dot{X}_D = \frac{R_X(E_o)\, S_o}{4\pi R^2} \exp[-\mu(E_o)P]\, B(E_o,\lambda), \quad \alpha_{min} < \alpha < \alpha_{max} \tag{3.20}$$

where

$\dot{X}_D$ = exposure rate due to direct penetration,

R = distance from the source to the detector,

$\mu(E_o)$ = attenuation coefficient for concrete for photons of energy E_o,

P = the path length the photons travel through the concrete ($P_o + P_1$ in Fig. 3.3),

and λ = number of mean free paths traveled by the photons $\{\mu(E_o)\, P\}$.

The source-to-detector distance R can be calculated from

$$R = [(x_o - x_d)^2 + (y_o - y_d)^2 + (z_o - z_d)^2]^{\frac{1}{2}}. \tag{3.21}$$

Direct-penetration photons can pass through the duct wall along five possible paths as illustrated in Fig. 3.4. Each of the possible paths present a different case for the calculation of the photon path length. For each case the angular range of α and the path length P is slightly different. Specifically, the results for the five cases are:

Case 1: This case is defined by

$$\tan^{-1}\left(\frac{-z_o}{x_o + W/2}\right) > \alpha > \tan^{-1}\left(\frac{L - z_o}{x_o - W/2}\right) \text{ , or } x_d \geq x_o. \tag{3.22}$$

For this case, the photon path length through the concrete is

$$P = \frac{L}{\sin\alpha} . \tag{3.23}$$

Case 2: This case is defined by

$$\tan^{-1}\left(\frac{L - z_o}{x_o - W/2}\right) > \alpha > \tan^{-1}\left(\frac{L - z_o}{x_o + W/2}\right) \text{ , and } \alpha > \tan^{-1}\left(\frac{-z_o}{x_o - W/2}\right) , \tag{3.24}$$

then

$$P = \left(x_o - \frac{W}{2} + \frac{z_o}{\tan\alpha}\right) \frac{1}{\cos\alpha} \tag{3.25}$$

Case 3: For this case is

$$\tan^{-1}\left(\frac{L - z_o}{x_o - W/2}\right) < \alpha < \tan^{-1}\left(\frac{-z_o}{x_o - W/2}\right) , \tag{3.26}$$

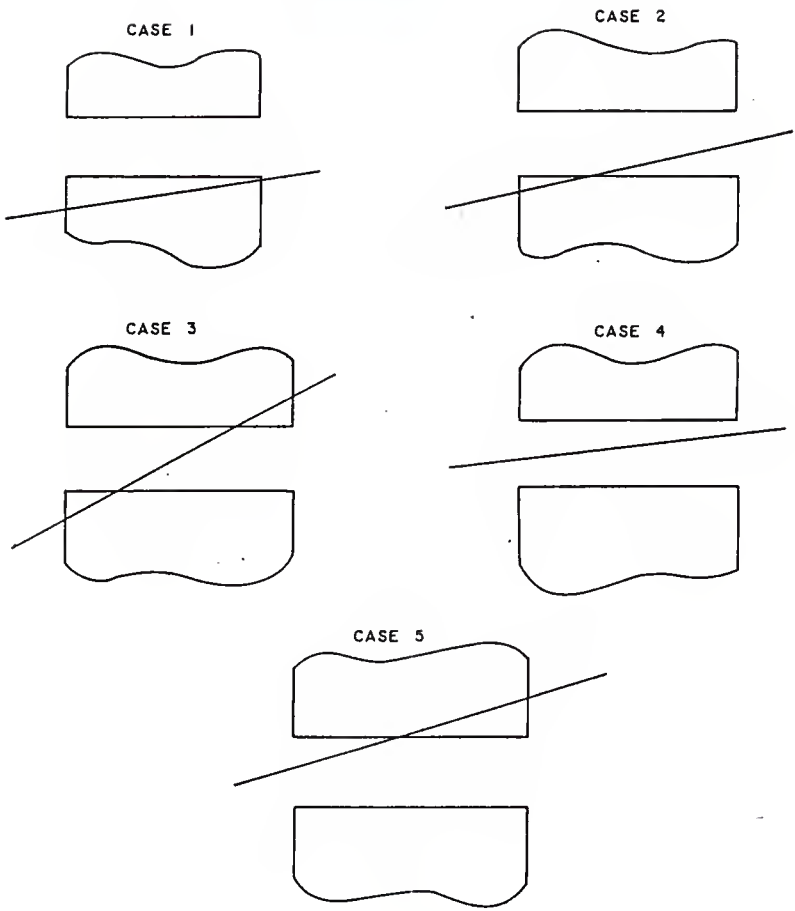

Fig. 3.4. Illustration of the possible paths directly penetrating radiation can have.

and the path length is defined by

$$P = \frac{L}{\sin\alpha} - \frac{W}{\cos\alpha} . \tag{3.27}$$

Case 4: In this case the photons travel completely in the duct so that

$$\tan^{-1}\left(\frac{L - z_o}{x_o - W/2}\right) > \alpha > \tan^{-1}\left(\frac{-z_o}{x_o - W/2}\right) , \tag{3.28}$$

and there is no path length in the concrete, i.e., P = 0.

Case 5: For this case

$$\tan^{-1}\left(\frac{L - z_o}{x_o - W/2}\right) > \alpha > \tan^{-1}\left(\frac{L - z_o}{x_o + W/2}\right) , \tag{3.29}$$

and

$$\alpha > \tan^{-1}\left(\frac{-z_o}{x_o + W/2}\right) , \tag{3.30}$$

and the path length is defined by

$$P = \left(\frac{L - z_o}{\tan\alpha} - x_o - \frac{W}{2}\right) \frac{1}{\cos\alpha} . \tag{3.31}$$

3.3 Lip Scattered Component

A "lip scatter" refers to a gamma ray which enters a portion of the wall, scatters once, then leaves through a wall surface that is perpendicular to the wall face through which the photon entered. Figure 3.5 illustrates different types of lip scattering. The "lip scattered component" refers to the exposure rate resulting from lip scattered photons and the buildup from photons scattered in the lip that pass through the duct wall.

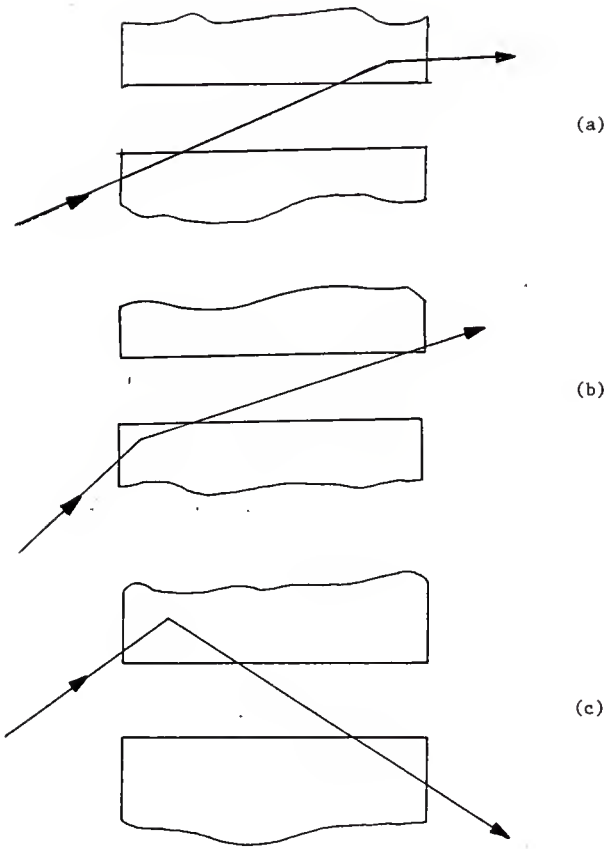

Fig. 3.5. Example of various lip scatters. Illustrated in (a) is a lip scatter that occurs on the detector side of the duct. A "near lip" scatter is shown in (b) and the scatter shown in (c) is a "far lip" scatter.

The general model development of lip scattering can be described as follows. Lip scattered photons are attenuated in the duct wall material before the lip scatter and undergo attenuation and buildup in the duct wall material after the scatter. A general expression of the exposure rate (at a detector outside the duct wall) resulting from a duct lip can be written as

$$\dot{X} = \iiint_V dV\ \phi\Sigma_s\ \exp(-\mu_i P - \mu_s P')\ B\ R \qquad (3.32)$$

where the integration is carried out over the lip volume, $\dot{X}$ is the exposure rate resulting from photons scattering in the lip region, dV is a differential volume element in the lip, ϕ is the photon flux (due to a source outside the duct wall) incident upon the differential volume, Σ_s is the scattering cross section for the incident photons scattering toward the detector, μ_i and μ_s are the attenuation coefficients of the photons before and after the scatter, P and P' are the photon path lengths in the wall material before and after the scatter, B is the buildup associated with the scattered photons, and R is a detector dosimetric response function. Equation (3.32) can be applied to any duct lip region to yield the exposure rate contribution from that lip region.

The source side of the duct (the "duct mouth") offers the only regions where the lip scattering can contribute significantly to the transmitted radiation field. As a result of numerous preliminary calculations, it was found that lip scattering that takes place in the duct lips on the detector side of the wall generally contribute a negligible amount to the overall exposure rate, especially if the duct height and width are small when compared to the duct length.

In the present development, there are four lip scattering regions that will be considered: (i) the duct-side lip, nearest to the source ("near lip"), (ii) the duct-side lip, farthest from the source ("far lip"), (iii) the duct top lip, and (iv) the duct bottom lip. Each lip scattering volume is bounded by an edge of the duct mouth, a portion of a wall, the plane of the duct mouth, and the two parallel planes extending from the duct walls on either side of the lip.

Three different techniques for modeling the lip regions were studied. The three techniques were: numerical integration of the lip regions, a method suggested by LeDoux [2], and a method suggested by Clifford [4]. All three techniques involved integration of the lip regions to determine the scattering sources presented by the lips. Both LeDoux's and Clifford's methods are simplified single-scatter techniques that use several geometric assumptions and represented the total lip scattering sources as single scattering points at the lip corners at the duct centerline elevation. The numerical integration method, on the other hand, is an exact method that uses no geometrical assumptions or simplifications. Calculations for determining the dose contribution from the near lip region were performed using all three techniques. The results of these calculations are summarized below.

The numerical integration technique developed in this study can be expected to yield the most accurate results. This technique involves the use of numerical quadrature to evaluate the volume integral in Eq. (3.32). Gaussian quadrature was used to evaluate the volume integral numerically, and it was found that a quadrature set of as low an order as five could be used with little error. A disadvantage of this

numerical integration technique over the simplified methods of LeDoux and Clifford is the comparatively large computational effort that is needed.

The method suggested by LeDoux provides an expression that can be evaluated easily and quickly. LeDoux suggested that the energy attenuation coefficient should be used in determining the photon attenuation. LeDoux further suggested that the same attenuation coefficient could be used for the photon path before and after the scatter. Use of the energy attenuation coefficient instead of the total attenuation coefficient provides a means of accounting for the photon buildup without introducing a buildup factor explicitly. The outcome of LeDoux's method was an expression in which the volumetric integration over the lip region could be evaluated analytically (using some geometrical assumptions). However, upon comparison of LeDoux's method and the numerically integrated model, it was found that LeDoux's method substantially underpredicted the dose and thus LeDoux's model was not used in this study.

The method suggested by Clifford [4] provided results that compared more favorably with the numerically integrated model than LeDoux's and was still computatively easy to evaluate. Clifford's method is very similar to LeDoux's. The main difference between Clifford's and LeDoux's methods is Clifford's use of a buildup factor and total attenuation coefficients. The addition of a buildup factor makes the models slightly more complex, but still allows the integration to be evaluated analytically (after some geometrical assumptions).

After reviewing the different methods, a modified version of Clifford's method was chosen to be used as the basis of the models of the duct lip regions in this work. This modification, which will be

referred to as the single-point scattering method, places the effective scatter point within the lip instead of at the corner as in Clifford's model. The exact position of the scattering point was determined by comparison of the Clifford based models to the numerically integrated model and by adjusting the scatter point location (i.e., moving the scatter point along the line that bisects the lip corner at the duct centerline elevation) until the exposure-rate peaks predicted by the two different models coincided. A comparison of values obtained using the single-point scattering method and the numerical integration method will be presented in the next section of this chapter.

In the experimental arrangement, the collimator and shadow shield allowed the duct mouth and duct lips to be fully illuminated, thus the effect of the source collimation can be ignored in the treatment of photon scattering by the lips. Nomenclature used throughout the scattering models are:

E_{sc} = scattered photon energy {MeV},

P_o = path length traveled by the photon before scattering,

P_1 = path length traveled by the photon after scattering and before leaving the lip,

P_2 = path length traveled by the photon after scattering and after leaving the lip,

R_1 = distance from source to the scatter point, and

R_2 = distance from the scatter point to the detector.

3.3.1 Exposure-Rate Contribution from the Near Lip

The geometry of scattering that occurs in the near lip is illustrated in Fig. 3.6. The near lip, of height H, extends from the duct corner to infinity in the x direction and over the length of the

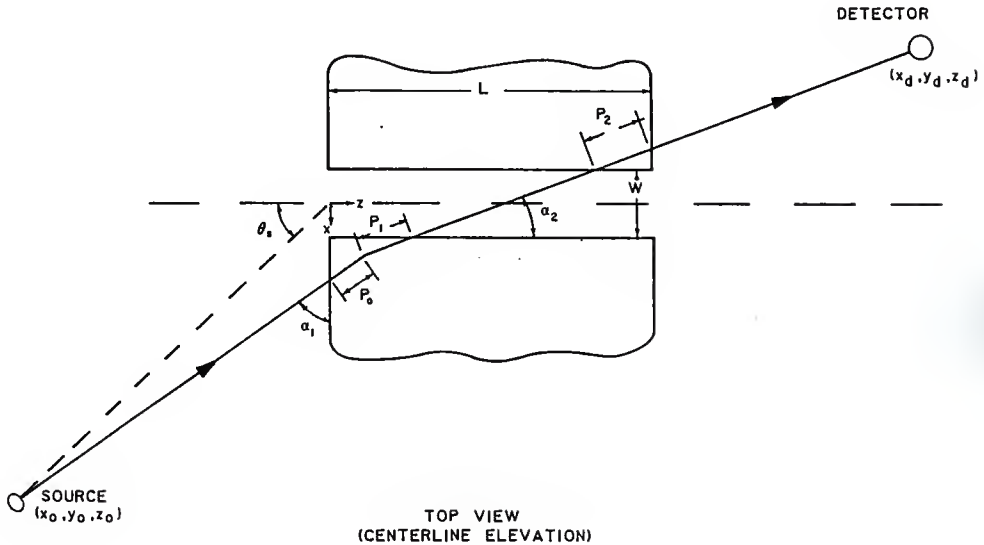

Fig. 3.6. Illustration of the geometry used in the formulation of the near lip component.

duct in the z direction. The near-lip exposure-rate contribution is composed of all photons that scatter in the near lip and their subsequent buildup that reaches the detector. The exposure rate resulting from these scatters occurring in the near lip, $\dot{X}_{NL}$, is

$$\dot{X}_{NL} = \frac{S_o}{4\pi} \int_{-H/2}^{H/2} dy \int_{0}^{L} dz \int_{W/2}^{\infty} dx \left(\frac{\Sigma_k(E_o,\theta_{sc})\ R_X(E_{sc})}{R_1^2\ R_2^2} \exp[-\mu(E_o)P_o] \right.$$

$$\left. \cdot \exp[-\mu(E_{sc})(P_1+P_2)]\ B(E_{sc},\mu(E_{sc})(P_1+P_2)) \right) \tag{3.33}$$

where

$$R_1 = [(x-x_o)^2 + (y-y_o)^2 + (z-z_o)^2]^{\frac{1}{2}}, \tag{3.34}$$

$$R_2 = [(x-x_d)^2 + (y-y_d)^2 + (z-z_d)^2]^{\frac{1}{2}}, \tag{3.35}$$

$$\theta_{sc} = \pi/4 - \alpha_1 - \alpha_2, \tag{3.36}$$

$$\alpha_1 = \tan^{-1}\left(\frac{z - z_o}{x_o - x}\right), \tag{3.37}$$

and

$$\alpha_2 = \tan^{-1}\left(\frac{x - x_d}{z_d - z}\right) . \tag{3.38}$$

Equation (3.33) is the explicit form of Eq. (3.32) for the near lip. This (Eq. 3.33) is also the form evaluated in the numerical integration method to yield the exposure-rate contribution from the duct near lip. If it is assumed that the lip scattered photons that contribute significantly to the radiation field leaving the duct are those which scatter near the lip corner and that this scattering volume near the lip corner is small when compared to the source and detector distance, then Eq. (3.33) can be greatly simplified. This assumption

allows that all scatters occurring in the lip can be represented by a single scattering point within the lip. This assumption also allows that all variables except those dealing with attenuation and buildup in the immediate scattering volume can be considered constant throughout the integration volume. Lastly, if one assumes the length of the near lip or duct height is small when compared to the source and detector distance, then the volume integral in Eq. (3.33) can be reduced to a surface integral independent of scattering point elevation. This leads to the following simplified equation.

$$\dot{X}_{NL} = C \int_0^L dz \int_{W/2}^{\infty} dx \left(\exp[-\mu(E_o)P_o] \exp[-\mu(E_{sc})P_1] \, B(E_{sc},\mu(E_{sc})P_1) \right) \tag{3.39}$$

where

$$C = \frac{S_o H \, \Sigma_k(E_o,\theta_{sc}) \, R_X(E_{sc})}{4\pi \, R_1^2 \, R_2^2} \exp[-\mu(E_{sc})P_2] \, B(E_{sc},\mu(E_{sc})P_2) \tag{3.40}$$

$$P_o = \frac{z}{\sin\alpha_1} , \tag{3.41}$$

$$P_1 = \frac{x - W/2}{\sin\alpha_2} , \text{ and} \tag{3.42}$$

$$P_2 = \begin{cases} \dfrac{L - z - \dfrac{(x + W/2)}{\tan\alpha_2}}{\cos\alpha_2} , & \text{if } \alpha_2 > \tan^{-1}\left(\dfrac{x + w/2}{L - z}\right), \\ 0, & \text{if } \alpha_2 \leq \tan^{-1}\left(\dfrac{x + W/2}{L - z}\right) . \end{cases} \tag{3.43}$$

Substituting Eqs. (3.13), (3.40) and (3.41) into Eq. (3.38) yields

$$\dot{X}_{NL} = C \int_0^L dz \exp[-\mu(E_o)\frac{z}{\sin\alpha_1}] \left[\int_0^\infty dx \exp\left[-\mu(E_{sc}) \frac{(x - \frac{W}{2})}{\sin\alpha_2}\right] + D \int_0^\infty dx \, (x - \frac{W}{2}) \exp[F \, (x - \frac{W}{2})] \right] \tag{3.44}$$

where

$$D = B_c \frac{k_1 \mu(E_{sc})}{\sin\alpha_2} (E_{sc})^{k_2} \tag{3.45}$$

and

$$F = \frac{k_3 \mu(E_{sc})}{\sin\alpha_2} \exp(k_4 E_{sc}) - \frac{\mu(E_{sc})}{\sin\alpha_2} . \tag{3.46}$$

Evaluation of the integrals in Eq. 3.37 leads to

$$\dot{X}_{NL} = -C \frac{\sin\alpha_1 \sin\alpha_2}{\mu(E_o) \mu(E_{sc})} \left[\exp\left(\frac{-\mu(E_o)L}{\sin\alpha_1}\right) - 1\right] \cdot \left[1 + \frac{k_1 (E_{sc})^{k_2}}{[k_3 \exp(k_4 E_{sc}) - 1]^2}\right] . \tag{3.47}$$

If one now assumes that $\frac{\mu(E_o)L}{\sin\alpha_1} >> 1$, then this result reduces to

$$\dot{X}_{NL} = C \frac{\sin\alpha_1 \sin\alpha_2}{\mu(E_o)\mu(E_{sc})} \left[1 + \frac{B_c k_1 (E_{sc})^{k_2}}{[k_3 \exp(k_4 E_{sc}) - 1]^2}\right] . \tag{3.48}$$

Equation (3.33) represents the exact ray-analysis technique for describing the near lip scattering region, while Eq. (3.48) represents a single-point scatter model for the same region. The validity of the geometric assumptions can be seen by comparing the exposure rates

obtained from Eq. (3.48) with those from Eq. (3.33). It was found that Eq. (3.33) could be evaluated numerically with good accuracy using only fifth order Gaussian Quadrature (numerical integration technique). The scatter point used for Eq. (3.48) in this comparison was (X = W/2 + 4 cm, y = 0, 2 = 4 cm), a point within the near lip that allowed the peak exposure rates of the two equations to occur at the same detector x-coordinate. The scatter point was found to be valid for all duct configurations that were considered. Based on this result, a corresponding point (X =-W/2 - 4 cm, y = 0, z = 4 cm) was used for the far lip models that are developed in the next section. Figure 3.7 shows a comparison of Eqs. (3.33) and (3.48) for three source angles, θ_s = 33°, 45° and 60°. Figure 3.7 shows that the single-point scattering method predicts values comparable to those obtained with the numerical integration. Consequently, Eq. (3.48), which is considerably simpler to use than the general result of Eq. (3.33), may be used with only a slight amount of error incurred.

3.3.2 Exposure-Rate Contribution from the Far Lip

The geometry of scattering in the far lip is shown in Fig. 3.8. Using the same assumptions that were presented in the previous section for the near lip, equations for the far lip component can be derived. The exposure rate resulting from scattering in the far lip, $\dot{X}_{FL}$, is (after applying the single-point scattering model assumptions)

$$\dot{X}_{FL} = C \int_{-\infty}^{-W/2} dx \exp[-\mu(E_{sc})P_1] \, B(E_{sc},\mu(E_{sc})P_1) \int_0^a dz \exp[-\mu(E_o)P_o] \qquad (3.49)$$

where

$$a = (-x - W/2) \tan\alpha_1, \qquad (3.50)$$

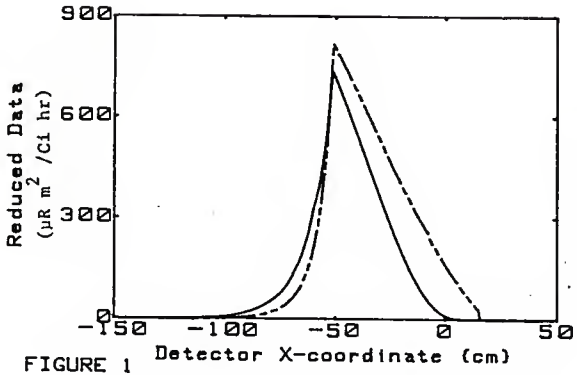

FIGURE 1

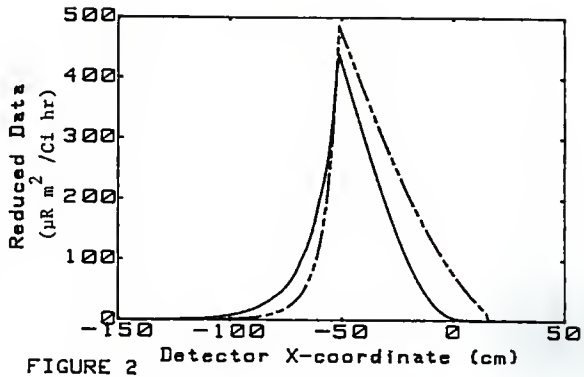

FIGURE 2

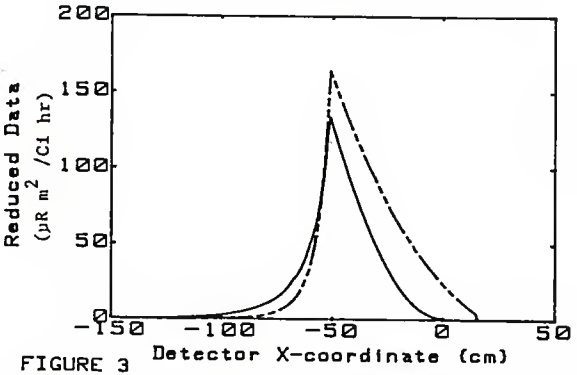

FIGURE 3

DUCT CONFIGURATION

Duct Height	= 30.5	cm
Duct Width	= 30.5	cm
Duct Length	= 101.6	cm
Source Distance	= 200	cm
Detector Elevation	= 0	cm
Detector Z-coordinate	= 200	cm
Buildup Correction Factor	= 0	cm
Source Angle (Figure 1)	= 33	degrees
Source Angle (Figure 2)	= 45	degrees
Source Angle (Figure 3)	= 60	degrees

Fig. 3.7. Comparison of the exposure rates predicted from Eq. (3.48) (dashed line) and Eq. (3.32) (solid line). The exposure rates are presented as reduced data, i.e., $\dot{X}\rho^2$/source

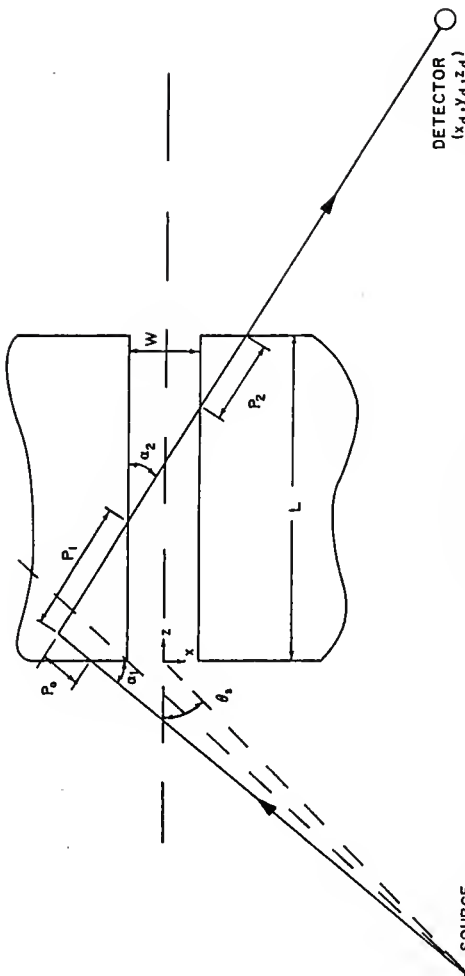

Fig. 3.8. Illustration of the geometry used in the formulation of the far lip component.

$$P_o = Z/\sin\alpha_1 \tag{3.51}$$

$$P_1 = -(X + W/2)/\sin\alpha_2 \tag{3.52}$$

$$\alpha_1 = \tan^{-1}\left(\frac{z - z_o}{x_o - x}\right), \tag{3.53}$$

$$\alpha_2 = \tan^{-1}\left(\frac{x_d - x}{z_d - z}\right), \tag{3.54}$$

$$C = \frac{S_o H\, \Sigma_k(E_o,\theta_{sc})\, R_X(E_{sc})}{4\pi\, R_1^2\, R_2^2} \exp[-\mu(E_{sc})P_2]\; B(E_{sc},\mu(E_{sc})P_2), \tag{3.55}$$

$$\theta_{sc} = \frac{\pi}{4} - \alpha_1 + \alpha_2\ , \tag{3.56}$$

and R_1 and R_2 are defined from Eqs. (3.34) and (3.35) respectively. Evaluation of the integrals in Eq. (3.49) yields

$$\dot{X}_{FL} = C \left\{ \frac{\sin\alpha_1 \sin\alpha_2}{\mu(E_o)\mu(E_{sc})} - \frac{\sin\alpha_1 \sin\alpha_2 \sin\alpha_1}{\mu(E_o)\mu(E_{sc})\cos\alpha_1 + \mu(E_o)^2 \sin\alpha_2} + \right.$$

$$\left. \sin\alpha_1\, B_c\, \frac{k_1 (E_{sc})^{k_2}}{\mu(E_o)} \left(\frac{\sin\alpha_2}{D^2 \mu(E_{sc})} - \frac{\mu(E_{sc})}{\sin\alpha_2} \left(\frac{\mu(E_{sc})}{\sin\alpha_2} D - \frac{\mu(E_o)}{\cos\alpha_1} \right)^{-2} \right) \right\}, \tag{3.57}$$

where

$$D = k_3 \exp(k_4 E_{sc}) - 1, \tag{3.58}$$

and

$$P_2 = \begin{cases} \dfrac{L - z + \dfrac{x - w/2}{\tan\alpha_2}}{\cos\alpha_2}\ , & \text{if } L - z + \dfrac{x - w/2}{\tan\alpha_2} > 0, \qquad (3.59) \\[2ex] 0\ , & \text{if } L - z + \dfrac{x - \frac{W}{2}}{\tan\alpha_2} \le 0. \qquad (3.60) \end{cases}$$

3.3.3 Exposure-Rate Contribution from the Top Lip

Figure 3.9 illustrates the geometry of lip scattering that occurs in the top lip. The exposure-rate contribution from this lip can be represented by (after applying the assumptions stated in Section 3.3.1)

$$\dot{X}_{TL} = C \int_0^L dz \int_a^\infty dy \exp[-\mu(E_o)P_o] \exp[-\mu(E_{sc})P_1] B(E_{sc},\mu(E_{sc})P_1) \qquad (3.61)$$

where

$$a = \frac{H}{2} - \frac{(zz_o)}{H/2} , \qquad (3.62)$$

$$P_o = \frac{z}{\sin\alpha_1} , \qquad (3.63)$$

$$P_1 = \frac{y - H/2}{\sin\alpha_2} , \qquad (3.64)$$

$$\alpha_1 = \sin^{-1}\left(\frac{y - y_o}{R_1}\right) , \qquad (3.65)$$

$$\alpha_2 = \sin^{-1}\left(\frac{y - y_d}{R_2}\right) , \qquad (3.66)$$

$$C = \frac{S_o W \Sigma_k(E_o,\theta_{sc}) R_X(E_{sc})}{4\pi R_1^2 R_2^2} \exp[-\mu(E_{sc})P_2] B(E_{sc},\mu(E_{sc})P_2), \qquad (3.67)$$

and

$$\theta_{sc} = \sin^{-1}\left(\frac{(x-x_o)(x_d-x) + (y-y_o)(y_d-y) + (z-z_o)(z_d-z)}{R_1 R_2}\right) , \qquad (3.68)$$

As before, the distances R_1 and R_2 are defined by Eqs. (3.33) and (3.34) respectively.

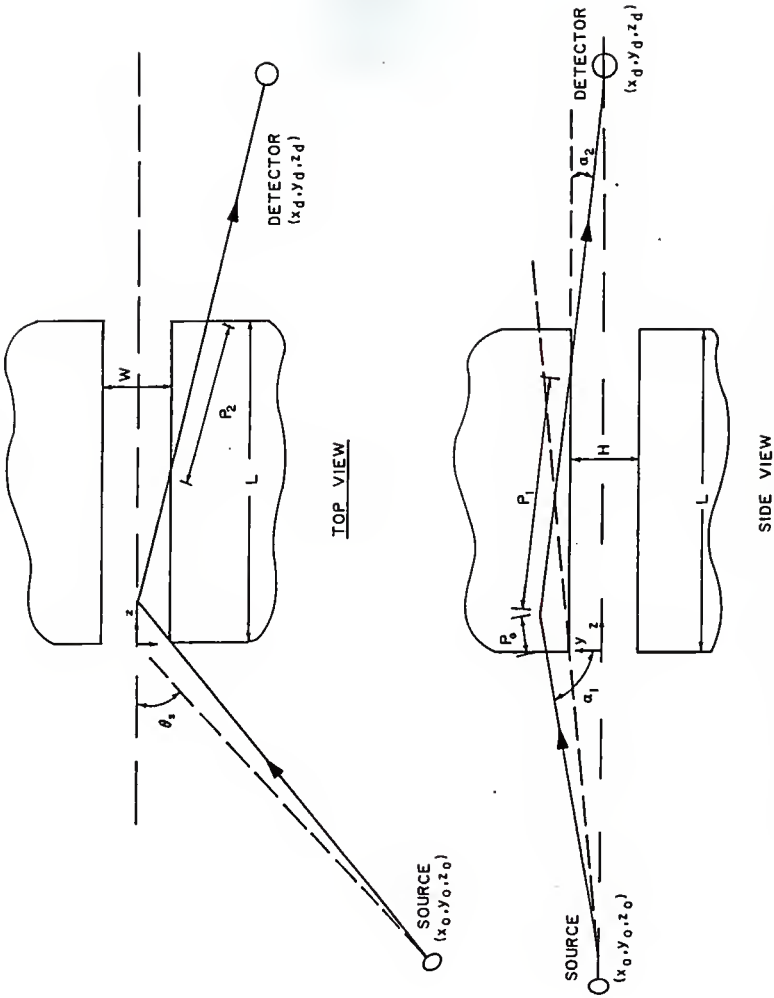

Fig. 3.9. Illustration of the top lip scattering geometry.

Analytic evaluation of the integrals in Eq. (3.61) then yields

$$\dot{X}_{TL} = C \left[\frac{\sin\alpha_2}{\mu(E_{sc})} \frac{1}{F} [\exp(LF) - 1] - \frac{D}{IG} \{\exp(LG)[L - \frac{1}{G} - \frac{1}{I}] + \frac{1}{G} + \frac{1}{I}\} \right], \quad (3.69)$$

where

$$D = B_c \, k_1 \, (E_{sc})^{k_2} \frac{\mu(E_{sc})}{\sin\alpha_2} , \quad (3.70)$$

$$I = \frac{\mu(E_{sc})}{\sin\alpha_2} (k_3 \exp(k_4 E_{sc}) - 1) , \quad (3.71)$$

$$F = \frac{\mu(E_o)}{\sin\alpha_1} + \frac{\mu(E_{sc})}{\sin\alpha_2} \frac{z_o}{H/2} , \text{ and} \quad (3.72)$$

and

$$G = \frac{-\mu(E_o)}{\sin\alpha_1} - \frac{z_o}{H/2} I . \quad (3.73)$$

If one assumes $-z_o > H/2$ and $L >> 1/\mu(E_o)$ then $-LF >> 1$. In Eq. (3.73), the dominant term is $-\mu(E_o)/\sin\alpha_1$, so that $-LG >> 1$. Equation (3.69) can then be simplified to

$$\dot{X}_{TL} = -C \left[\frac{\sin\alpha_2}{\mu(E_{sc})} \frac{1}{F} + \frac{D}{IG} \left(\frac{1}{G} + \frac{1}{E} \right) \right] . \quad (3.74)$$

To calculate C in the above expression, the path P_2 can be approximated by

$$P_2 \cong \left(\frac{L - z}{\cos\gamma} - \frac{W/2}{\sin\gamma} \right) \frac{1}{\cos\alpha_2} , \quad (3.75)$$

where

$$\gamma = \tan^{-1} \left(\frac{|x - x_d|}{z_d - z} \right) . \quad (3.76)$$

If the value obtained from Eq. (3.75) is negative, then one should set $P_2 = 0$, i.e., the path is entirely in the duct.

3.3.4 Exposure-Rate Contribution from the Bottom Lip

The exposure rates resulting from scatters in the bottom lip are equal to those from the top lip, if the detector and source are at the duct centerline elevation. Such is the case for all ducts considered in this study. Thus, Eq. (3.74) can be used to calculate the bottom lip exposure rate contributions.

3.4 Wall Scattered Component

A "wall scatter" refers to a gamma ray which enters a portion of the duct wall, scatters once, then leaves the duct wall. Unlike the lip scatters, the wall scattered photon's entry and exit points are on the same wall face. The wall scattered component refers to the exposure rate resulting from wall scattered photons and the buildup from photons scattered in the wall that pass through the duct.

The general model development of wall scattering is the same as that used in lip scattering, except the volume integration is now carried out over a wall volume.

Since the source photons are obliquely incident upon the duct mouth, they can scatter off only three of the four duct walls. These three walls can be divided into four distinct scattering regions. These regions are: (i) the portion of the duct side wall that is directly exposed to the source ("wall #1"), (ii) the portion of the duct side wall that is shielded by the near lip region ("wall #2"), (iii) the top wall of the duct that is directly exposed to the source, and (iv) the bottom wall of the duct that is directly exposed to the source.

Both the single-point scattering method and albedo technique were used to evaluate the exposure rates arising from the wall scattering regions. Chapter 4 will present a detailed comparison of results obtained from the single-point scattering and albedo modeling techniques.

The single-scattering technique, as applied to wall scattering uses many of the same assumptions previously employed in the lip scattering calculations. These assumptions can be restated as:

1) The wall scatters that lead to photons reaching the detector occur almost entirely in a thin layer (less than a mean free path) of the wall near the surface.

2) The scattering area and its associated distances from the source and detector are such that all scatters that occur in the wall can be represented by a single point in the wall.

The above assumptions can be applied in much the same way as those used in the lip scattering components to reduce the volume integrations to simpler equations.

The scattering points used in evaluation of the wall scatter models are located at the centroid of the illuminated wall surfaces.

3.4.1 Exposure-Rate Contribution from Wall #1

(a) Single Scatter Approach

The geometry of wall #1 scattering is illustrated in Fig. 3.10. In the wall #1 scattering region, only a single integration needs to be performed after the assumptions stated on the previous page are applied in the same manner as in the lip components. This is due to the fact that the path lengths in the scatter region before and after the scatter

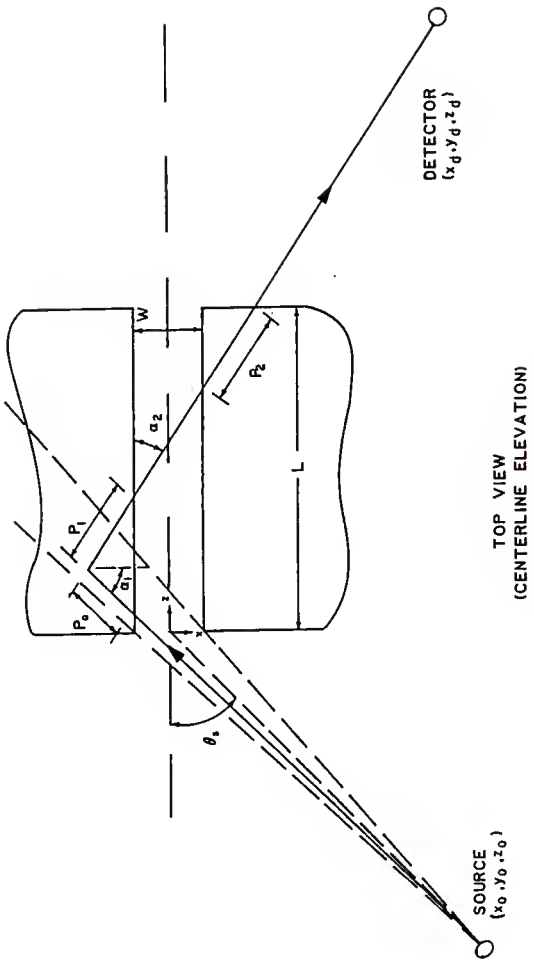

Fig. 3.10. Scattering geometry used in the wall #1 component.

depend only on the x-coordinate of the scatter point and the angles α_1 and α_2. The resulting exposure rate $\dot{X}_{W1}$ can be thus written as

$$\dot{X}_{W1} \cong C \int_{-\infty}^{-W/2} dx \exp[-\mu(E_o)P_o] \exp[-\mu(E_{sc}) P_1] B(E_{sc},\mu(E_{sc})P_1) \tag{3.77}$$

where

$$C = \frac{S_o H \Sigma_k(E_o,\theta_{sc}) R_X(E_{sc})}{4\pi R_1^2 R_2^2} W \tan\alpha_1 \exp[-\mu(E_{sc})P_2]B(E_{sc},\mu(E_{sc})P_2), \tag{3.78}$$

$$P_o = \frac{-x - W/2}{\cos\alpha_1} , \tag{3.79}$$

$$P_1 = \frac{-x - W/2}{\sin\alpha_2} , \tag{3.80}$$

$$\alpha_1 = \tan^{-1}\left(\frac{z - z_o}{x_o - x}\right) , \tag{3.81}$$

$$\alpha_2 = \tan^{-1}\left(\frac{x_d - x}{z_d - z}\right) , \tag{3.82}$$

and

$$\theta_{sc} = \frac{\pi}{4} - \alpha_1 + \alpha_2 . \tag{3.83}$$

The distances R_1 and R_2 are defined from Eqs. (3.34) and (3.35) respectively, and

$$P_2 = \begin{cases} \left(L - z + \dfrac{x - W/2}{\tan\alpha_2}\right) \dfrac{1}{\cos\alpha_2} , & \text{if } L - z + \dfrac{x - W/2}{\tan\alpha_2} > 0, \text{ or} \quad (3.83) \\ 0, & \text{if } L - z + \dfrac{x - W/2}{\tan\alpha_2} \leq 0. \quad (3.84) \end{cases}$$

Evaluation of the integral in Eq. (3.87) leads to

$$\dot{X}_{W1} = C \left[\frac{\cos\alpha_1}{\mu(E_o) + \mu(E_{sc})\frac{\cos\alpha_1}{\sin\alpha_2}} + \frac{B_c k_1 (E_{sc})^{k_2} \quad \mu(E_{sc})}{\left[\frac{\mu(E_{sc})}{\sin\alpha_2} D - \frac{\mu(E_o)}{\cos\alpha_1}\right]^2 \sin\alpha_2} \right] \tag{3.85}$$

where

$$D = k_3 \exp(k_4 E_{sc}) - 1 \tag{3.86}$$

(b) Albedo Approach

The dose from wall #1 region can be expressed, recalling Eq. (3.16), as

$$\dot{X}_{W1} = \frac{S_o R_X(E_o) \cos\alpha_1 \alpha_X(E_o,\alpha_1;\pi/4 - \alpha_2,0) HW \tan\alpha_1}{4\pi R_1^2 R_2^2}$$

$$\cdot \exp[-\mu(E_{sc})P_2] B(E_{sc}, \mu(E_{sc})P_2) \tag{3.87}$$

or, more simply as

$$\dot{X}_{W1} = \frac{S_o HW \sin\alpha_1 \alpha_X(E_o,\alpha_1;\pi/4 - \alpha_2,0) R_X(E_o)}{4\pi R_1^2 R_2^2}$$

$$\cdot \exp[-\mu(E_{sc})P_2] B(E_{sc},\mu(E_{sc})P_2, \tag{3.88}$$

where α_X is the albedo function defined in Eq. (3.14), P_2 is defined in Eqs. (3.59) and (3.60), and α_1 and α_2 are the same as defined in the single-point scatter approach for wall #1.

The above equations assume that the scattering point is at the same elevation as the source and detector and is on the duct wall surface $(x = -\frac{W}{2}, y = 0)$.

3.4.2 Exposure-Rate Contribution From Wall #2

(a) Single Scatter Approach

Figure 3.11 illustrates the geometry of the wall #2 scattering. The exposure rate resulting from wall #2, $\dot{X}_{W2}$, can be expressed as

$$\dot{X}_{W2} = C \int_{a}^{-W/2} dx \int_{b}^{c} dz \exp[-\mu(E_o)(P_o + P_1)] \exp[-\mu(E_{sc})P_2] B(E_{sc},\mu(E_{sc})P_2) \quad (3.89)$$

where

$$C = \frac{S_o H \Sigma_k(E_o,\theta_{sc}) R_X(E_{sc})}{4\pi R_1^2 R_2^2} \exp[-\mu(E_{sc})P_3] B(E_{sc},\mu(E_{sc})P_3), \quad (3.90)$$

$$a = W - \frac{L}{\tan\alpha_1}, \quad (3.91)$$

$$b = (\frac{W}{2} - x) \tan\alpha_1, \quad (3.92)$$

$$\alpha_1 = \tan^{-1}\left(\frac{z - z_o}{x_o - x}\right), \quad (3.93)$$

$$\alpha_2 = \tan^{-1}\left(\frac{x_d - x}{z_d - z}\right), \quad (3.94)$$

$$\theta_{sc} = \frac{\pi}{4} - \alpha_1 + \alpha_2, \quad (3.95)$$

$$P_o = \frac{z}{\sin\alpha_1} - \frac{(W/2 - x)}{\cos\alpha_1}, \quad (3.96)$$

$$P_1 = \frac{-x - W/2}{\cos\alpha_1}, \quad (3.97)$$

$$P_2 = \frac{-x - W/2}{\cos\alpha_2}. \quad (3.98)$$

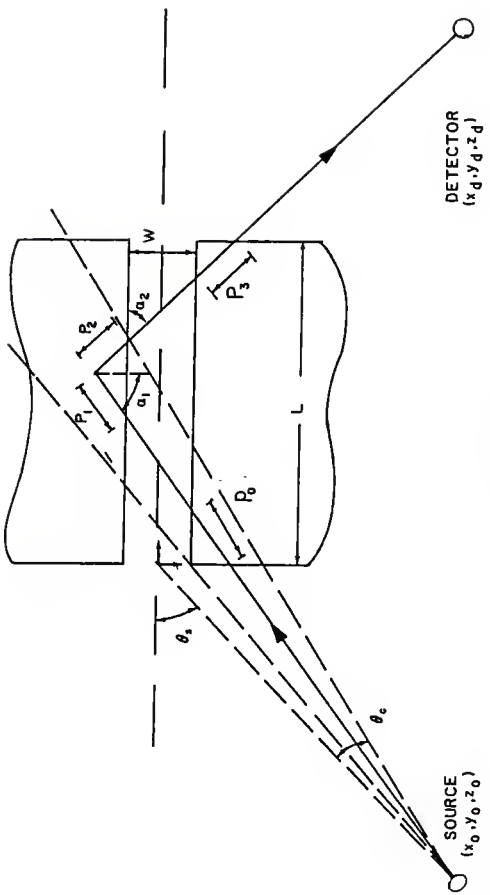

Fig. 3.11. Scattering geometry used in the wall #2 component.

The upper bound of the inner integral, c, can have two possible values, representing two cases, namely

Case #1:

$$c = L, \quad \text{if } z_o + (x_o + \frac{W}{2}) \tan(\frac{\pi}{4} - \theta_c - \theta_s) > L \tag{3.99}$$

Case #2:

$$c = z_o + (x_o - x) \tan(\frac{\pi}{4} - \theta_c - \theta_s), \quad \text{if not case 1.} \tag{3.100}$$

For Case #1

$$\dot{X}_{W2} = C \frac{\sin\alpha_1}{\mu(E_o)} \left[\frac{1}{A} \left(\exp\left(\left(\frac{L}{\tan\alpha_1} - \frac{3W}{2} \right) A \right) - 1 \right) \right.$$

$$\left. + \frac{F}{D+A} \left(\exp\left(\left(\frac{L}{\tan\alpha_1} - \frac{3W}{2} \right)(D+A) \right) \left(\frac{L}{\tan\alpha_1} - \frac{3W}{2} - \frac{1}{D+A} \right) + \frac{1}{D+A} \right) \right] \tag{3.101}$$

where

$$A = \frac{-\mu(E_o)}{\cos\alpha_1} - \frac{\mu(E_{sc})}{\sin\alpha_2}, \tag{3.102}$$

$$D = \frac{\mu(E_{sc})}{\sin\alpha_2} k_3 \exp(k_4 E_{sc}), \quad \text{and} \tag{3.103}$$

$$F = B_c k_1 (E_{sc})^{k_2} \frac{\mu(E_{sc})}{\sin\alpha_2}. \tag{3.104}$$

For Case #2,

$$\dot{X}_{W2} = C \frac{\sin\alpha_1}{\mu(E_o)} \left[\left(\frac{1}{A} \left(\exp\left(\left(\frac{L}{\tan\alpha_1} - \frac{3W}{2} \right) A \right) - 1 \right) \right) \right.$$

$$\left. + \frac{F}{D+A} \left(\exp\left(\left(\frac{L}{\tan\alpha_1} - \frac{3W}{2} \right)(D+A) \right) \left(\frac{L}{\tan\alpha_1} - \frac{3W}{2} - \frac{1}{D+A} \right) + \frac{1}{D+A} \right) \right)$$

$$- G\left(\frac{1}{A'}\left[\exp\left[\left(\frac{L}{\tan\alpha_1} - \frac{3W}{2}\right)A'\right] - 1\right] + \frac{F}{D+A'}\left[\exp\left[\left(\frac{L}{\tan\alpha_1} - \frac{3W}{2}\right)(D+A')\right]\right.\right.$$

$$\left.\left. \cdot \left(\frac{L}{\tan\alpha_1} - \frac{3W}{2} - \frac{1}{D+A'}\right) + \frac{1}{D+A'}\right]\right) \qquad (3.105)$$

where

$$A' = \frac{-\mu(E_{sc})}{\sin\alpha_2} - \frac{\mu(E_o)}{\sin\alpha_1}\tan\left(\frac{\pi}{4} - \theta_c - \theta_s\right) , \qquad (3.106)$$

and

$$G = \exp\left[\frac{\mu(E_o)}{\cos\alpha_1} W - \frac{\mu(E_o)}{\sin\alpha_1}\left[z_o + \left(x_o + \frac{W}{2}\right)\tan\left(\frac{\pi}{4} - \theta_c - \theta_s\right)\right]\right]. \qquad (3.107)$$

If the source distance is much greater than the duct width, then $G \cong 0$, and Case #1 and Case #2 become equivalent.

The distance P_3 is calculated from

$$P_3 = \begin{cases} \left(L - z + \dfrac{x - W/2}{\tan\alpha_2}\right)\dfrac{1}{\cos\alpha_2}, & \text{if } L - z + \dfrac{x - W/2}{\tan\alpha_2} > 0, \qquad (3.108) \\ 0, & \text{if } L - z + \dfrac{x - W/2}{\tan\alpha_2} \leq 0. \qquad (3.109) \end{cases}$$

(b) Albedo Approach

The albedo dose from the wall #2 region is approximated by assuming that the corner of the lip #1 region is transparent and that all radiation scattering from wall #2 passes through this transparent area. LeDoux and Chilton [6] suggest that the transparent area be bounded by a distance equal to one mean free path, λ, of an incident photon (see Fig. 3.12). The exposure rate from wall #2 is thus,

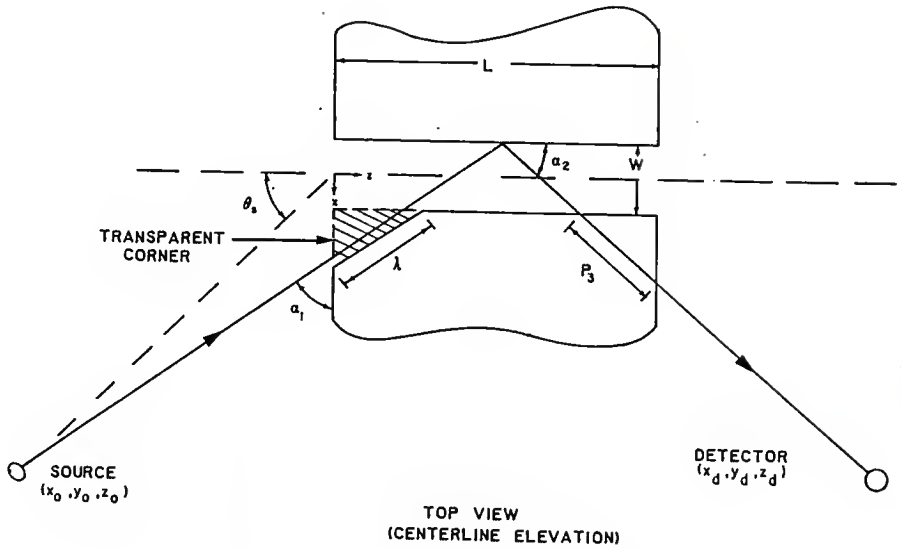

Fig. 3.12. Illustration of the transparent corner used in the albedo formulation of the wall #2 component.

$$\dot{X}_{W2} = \frac{S_o H \frac{\sin\alpha_1}{\mu(E_o)} \cos\alpha_1 \; \alpha_X(E_o,\alpha_1;\frac{\pi}{4} - \alpha_2, 0) \; R_X(E_o)}{4\pi \; R_1^2 \; R_2^2}$$

$$\cdot \exp[-\mu(E_{sc})P_3] \; B(E_{sc},\mu(E_{sc})P_3) \qquad (3.110)$$

where P_3 is defined from Eqs. (3.108) and (3.109).

3.4.3 Exposure-Rate Contribution from the Top of the Duct

(a) Single-Scatter Approach

Figure 3.13 shows the geometry of a scatter in the top of the duct. The illuminated surface of the top of the duct region is triangular. In order to simplify the integration of the scattering kernel, this surface was assumed to be a rectangle with an area equal to that of the actual illuminated triangular area. The exposure rate, denoted by by $\dot{X}_{TW}$, is thus given by

$$\dot{X}_{TW} = C \int_0^a dz \int_{H/2}^b dy \exp[-\mu(E_o)P_o] \exp[-\mu(E_{sc})P_1] B(E_{sc},\mu(E_{sc})P_1) \qquad (3.111)$$

where

$$a = \frac{W}{2} \tan\beta_1 \; , \qquad (3.112)$$

$$b = H/2 + z \tan\beta_2 \qquad (3.113)$$

$$C = \frac{S_o \; W \; \Sigma_k(E_o,\theta_{sc}) \; R_X(E_{sc})}{4\pi \; R_1^2 \; R_2^2} \exp[-\mu(E_{sc})P_2] B(E_{sc},\mu(E_{sc})P_2), \qquad (3.114)$$

$$P_o = \frac{y - H/2}{\sin\alpha_1} \; , \qquad (3.115)$$

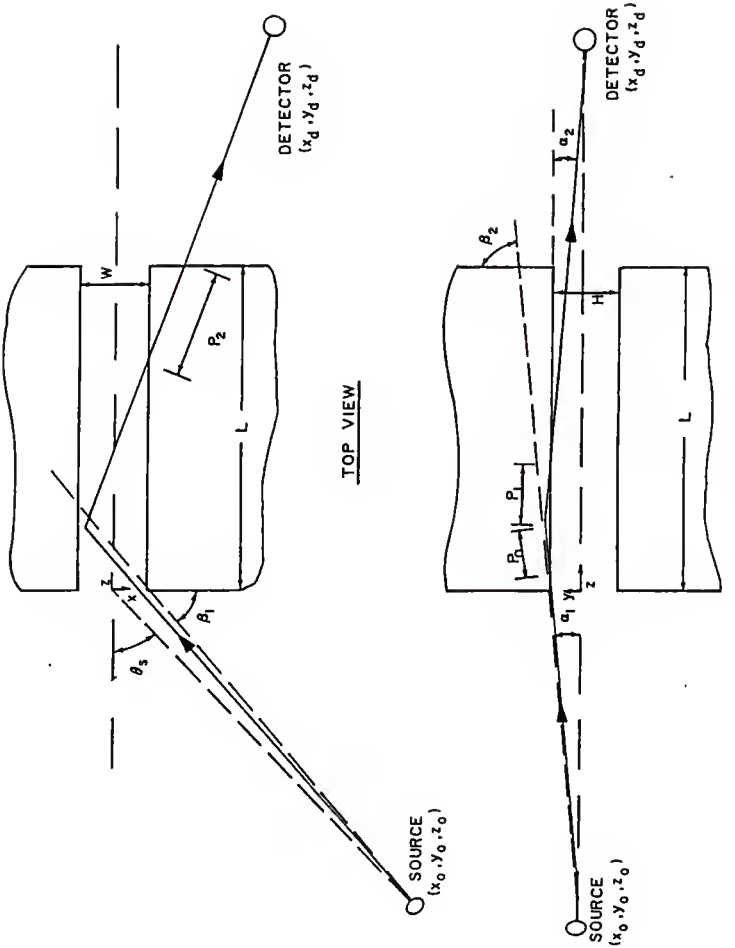

Fig. 3.13. Scattering geometry used in the top of the duct scattering component.

$$P_1 = \frac{y - H/2}{\sin\alpha_2} , \tag{3.116}$$

$$\alpha_1 = \sin^{-1}\left(\frac{y - y_o}{R_1}\right) , \tag{3.117}$$

$$\alpha_2 = \sin^{-1}\left(\frac{y - y_d}{R_2}\right) , \tag{3.118}$$

$$\beta_1 = \tan^{-1}\left(\frac{-z_o}{x_o - W/2}\right) , \tag{3.119}$$

$$\beta_2 = \tan^{-1}\left(\frac{-z_o}{H/2}\right) . \tag{3.120}$$

Again, R_1 and R_2 are defined in Eqs. (3.34) and (3.35), and P_2 is defined in Eq. (3.75).

Evaluation of Eq. (3.111) leads to

$$\dot{X}_{TW} = C \left\{ \frac{\exp(AF\tan\beta_2) - 1}{F^2\tan\beta_2} - \frac{A}{F} + \frac{D}{(G+F)^2} \right.$$
$$\left. \cdot \left[\exp[A(G+F)\tan\beta_2] \left(A - \frac{2}{(G+F)\tan\beta_2} \right) + A + \frac{2}{(G+F)\tan\beta_2} \right] \right\} \tag{3.121}$$

where

$$A = \frac{W}{2}\tan\beta_1 , \tag{3.122}$$

$$D = B_c k_1 (E_{sc})^{k_2} \frac{\mu(E_{sc})}{\sin\alpha_2} , \tag{3.123}$$

$$F = \frac{-\mu(E_o)}{\sin\alpha_1} - \frac{\mu(E_{sc})}{\sin\alpha_2} , \tag{3.124}$$

and

$$G = \frac{\mu(E_{sc})}{\sin\alpha_2} k_3 \exp(k_4 E_{sc}) \quad . \tag{3.125}$$

(b) Albedo Approach

The albedo formulation of the exposure rate from the top wall is

$$\dot{X}_{TW} = \frac{S_o W^2 \tan\beta_1 \sin\alpha_1 \alpha_X(E_o, \frac{\pi}{4} - \alpha_1; \frac{\pi}{4} - \alpha_2, \psi)}{8\pi R_1^2 R_2^2} R_X(E_o)$$

$$\cdot \exp[-\mu(E_{sc})P_2] B(E_{sc}, \mu(E_{sc})P_2) \tag{3.126}$$

where

$$\psi = \tan^{-1}\left(\frac{x_o - x}{z - z_o}\right) + \tan^{-1}\left(\frac{x_d - x}{z_d - z}\right) \quad , \tag{3.127}$$

and P_2 is defined in Eq. (3.75).

3.4.4 Exposure-Rate Contribution from the Bottom of the Duct

The exposure rates resulting from scatters in bottom of the duct are equal to those from top of the duct, if the detector is at the duct centerline elevation.

3.5 Multiple Scattering from the Duct Walls

Photons may scatter more than once from the walls of the duct before reaching the detector. The largest contribution of the dose resulting from such multiple scatters is due to double scatters. Therefore, only double scattering are considered in the following discussion.

There are two main types of double wall scatters. The first type ("double-1") is illustrated in Fig. 3.14 and represents radiation that experiences its first scatter or reflection in the near lip region and

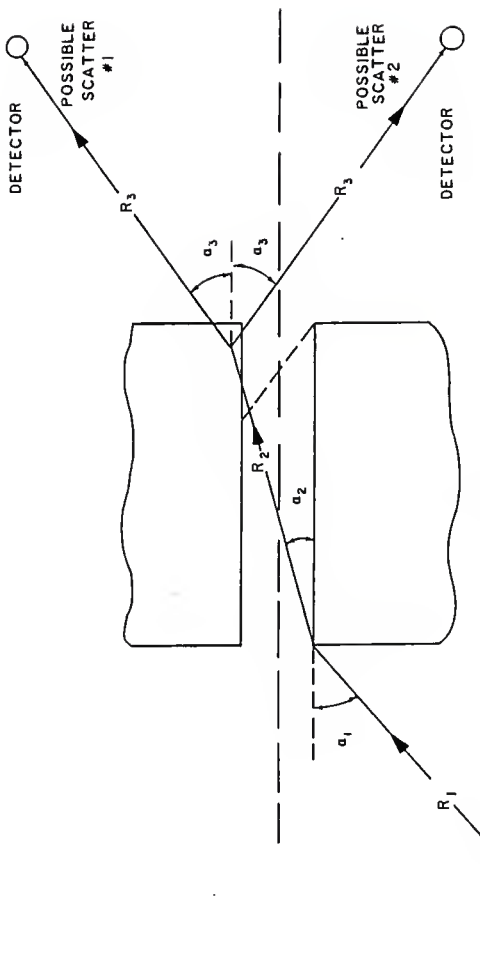

Fig. 3.14. Illustration of the double-1 scattering geometry.

then scatters again from the opposite side of the duct, on the detector side of the wall. The second type ("double-2"), shown in Fig. 3.15, has the photon first scatter from the wall #1 region and then again from the opposite side of the duct.

These double scatters are just combinations of lip and wall scatters. Thus, the appropriate equations developed in Section 3.3 and 3.4 can be used to calculate a resulting exposure rate at the detector due to double scatters. Before explicit expressions are presented for these double-scatter exposure rates, the following notation is introduced:

x, y, z = first scatter point,

x', y', z' = second scatter point,

E_{sc} = energy of photon after first scatter,

E'_{sc} = energy of photon after second scatter,

θ_{sc} = scattering angle of first scatter,

θ'_{sc} = scattering angle of second scatter,

R_1 = distance between source and first scatter,

R_2 = distance between scatter points, and

R_3 = distance from second scatter point to detector.

3.5.1 Exposure-Rate Contribution from Double-1 Scatters

The location of the first scatter of the double-1 is on the near lip, while the second scatter can be either a lip or wall scatter depending on the detector position. Figure 3.14 shows the two possible scattering paths of the second scatter, with "possible scatter #1" having a second lip scatter while "possible scatter #2" has a wall

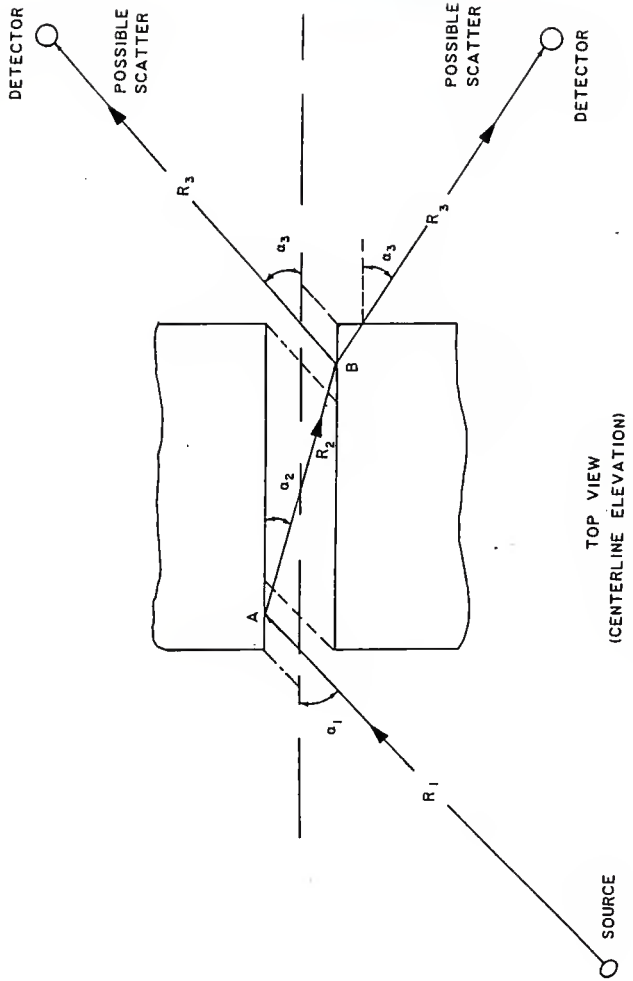

Fig. 3.15. Illustration of the double-2 scattering geometry.

scatter. The resulting exposure rates for these two scattering paths can be readily computed using the single-point scattering technique. The results are as follows:

(a) Possible Scatter #1 (defined by $x_d \leq -\frac{W}{2}$)

$$\dot{X}_{DB1} = C \frac{\cos\alpha_1 \, (\sin\alpha_2)^2 \cos\alpha_3}{\mu(E_o)\mu(E_{sc})^2\mu(E'_{sc})} (1+D) \tag{3.128}$$

where

$$C = \frac{S_o H^2 R_X(E'_{sc}) \; \Sigma_k(E_o,\theta_{sc}) \; \Sigma_k(E_{sc},\theta'_{sc})}{4\pi \; R_1^2 \; R_2^2 \; R_3^2} , \tag{3.129}$$

$$D = \frac{B_c k_1 (E'_{sc})^{k_2}}{[k_3 \exp(k_4 \; E'_{sc}) - 1]^2} , \tag{3.130}$$

$$\alpha_1 = \tan^{-1}\left(\frac{x_o - x}{z - z_o}\right) , \tag{3.131}$$

$$\alpha_2 = \tan^{-1}\left(\frac{x - x'}{z' - z}\right) , \tag{3.132}$$

$$\alpha_3 = \tan^{-1}\left(\frac{|x_d - x'|}{z_d - z'}\right) , \tag{3.133}$$

$$\theta_{sc} = \alpha_1 - \alpha_2 , \tag{3.134}$$

and

$$\theta_{sc}' = \alpha_3 - \alpha_2 . \tag{3.135}$$

(b) Possible Scatter #2 (defined by $x_d > -\frac{W}{2}$)

$$\dot{X}_{DB1} = C \frac{\cos\alpha_1 \; \sin\alpha_2}{\mu(E_o)\mu(E_{sc})} \left(\frac{\sin\alpha_2}{\mu(E_{sc}) + \mu(E'_{sc})\frac{\sin\alpha_2}{\sin\alpha_3}} + F\right) \tag{3.136}$$

where

$$C = \frac{S_o H^2 W\, R_X(E'_{sc})\, \Sigma_k(E_o,\theta_{sc})\, \Sigma_k(E_{sc},\theta'_{sc}) \tan\alpha_3}{4\pi\, R_1^2\, R_2^2\, R_3^2}, \tag{3.137}$$

$$F = \frac{B_c k_1 (E'_{sc})^{k_2}}{\left(\frac{\mu(E'_{sc})}{\sin\alpha_3} D - \frac{\mu(E_{sc})}{\sin\alpha_2}\right)^2} \frac{\mu(E'_{sc})}{\sin\alpha_3}, \tag{3.138}$$

$$D = k_3 \exp(k_4 E'_{sc}) - 1, \tag{3.139}$$

and

$$\theta'_{sc} = \alpha_2 + \alpha_3. \tag{3.140}$$

3.5.2 Exposure-Rate Contribution from Double-2 Scatters

The first scatter in double-2 is a wall #1 scatter. Figure 3.15 illustrates the two possible second scattering paths. "Possible scatter #1" is a second wall scatter and "possible scatter #2" is a lip scatter. The resulting exposure rates, $\dot{X}_{DB2}$, resulting from applying the single-point scattering technique are shown below.

(a) Possible Scatter #1 (defined by $x_d \leq \frac{W}{2}$)

$$\dot{X}_{DB2} = CG \left(\frac{\sin\alpha_2}{\mu(E_{sc}) + \mu(E'_{sc}) \frac{\sin\alpha_2}{\sin\alpha_3}} + F \right) \tag{3.141}$$

where

$$C = \frac{S_o H^2 W^2 \cot\alpha_1 \cot\alpha_3\, R_X(E'_{sc})\, \Sigma_k(E_o,\theta_{sc})\, \Sigma_k(E_{sc},\theta'_{sc})}{4\pi\, R_1^2\, R_2^2\, R_3^2}, \tag{3.142}$$

$$G = \frac{\sin\alpha_1}{\mu(E_o) + \mu(E_{sc}) \frac{\sin\alpha_1}{\sin\alpha_2}}, \tag{3.143}$$

$$F = \frac{B_c K_1 (E'_{sc})^{k_2}}{\left[\frac{\mu(E'_{sc})}{\sin\alpha_3} D - \frac{\mu(E_{sc})}{\sin\alpha_2}\right] 2} \frac{\mu(E'_{sc})}{\sin\alpha_3}, \tag{3.144}$$

$$D = k_3 \exp(k_4 E'_{sc}) - 1, \tag{3.145}$$

$$\alpha_1 = \tan^{-1}\left(\frac{x_o - x}{z - z_o}\right), \tag{3.146}$$

$$\alpha_2 = \tan^{-1}\left(\frac{x' - x}{z' - z}\right), \tag{3.147}$$

$$\alpha_3 = \tan^{-1}\left(\frac{|x' - x_d|}{z_d - z'}\right), \tag{3.148}$$

$$\theta_{sc} = \alpha_1 + \alpha_2, \text{ and} \tag{3.149}$$

$$\theta'_{sc} = \alpha_2 + \alpha_3. \tag{3.150}$$

(b) Possible Scatter #2 (defined by $x_d > \frac{W}{2}$)

$$\dot{X}_{DB2} = CG \frac{\sin\alpha_2 \cos\alpha_3}{\mu(E_{sc})\mu(E'_{sc})} \left(1 + \frac{B_c k_1 (E'_{sc})^{k_2}}{[k_3 \exp(k_4 E'_{sc}) - 1]^2}\right) \tag{3.151}$$

where

$$C = \frac{S_o H^2 W \cot\alpha_1 R_X(E'_{sc}) \Sigma_k(E_o, \theta_{sc}) \Sigma_k(E_{sc}, \theta'_{sc})}{4\pi R_1^2 R_2^2 R_3^2}, \tag{3.152}$$

$$G = \frac{\sin\alpha_1}{\mu(E_o) + \mu(E_{sc}) \frac{\sin\alpha_1}{\sin\alpha_2}}, \text{ and} \tag{3.153}$$

$$\theta'_{sc} = \alpha_3 - \alpha_2. \tag{3.154}$$

CHAPTER 4

MODEL REFINEMENTS AND COMPARISON TO EXPERIMENT

In this chapter, the models developed in Chapter 3 will undergo some refinements and be compared. The refinements will include modifications of the model to account for some non-ideal conditions present in the KSU gamma-ray streaming experiment, as well as to eliminate the model components that contribute a negligible amount to the gamma-ray streaming dose. Two comparison will be presented in this chapter. The first comparison will show how the point-scatter method for describing duct-wall scatters compares to the empirical albedo based method. Following the point-scatter and albedo method comparison, the characteristics of the various model components will be presented. These characteristics show how and where each component contributes to the overall gamma-ray streaming dose. In the second comparison, the model will be compared to the experimental data. Lastly, so that a fuller understanding of radiation streaming through ducts can be gained, the effects of changes in the duct geometry on the duct-streaming-radiation field will be presented.

In order to compare the model results to the experimental data, the calculated values must first be modified to emulate the experiment as closely as possible. There are three main differences between the idealized model (presented in the previous chapter) and the experimental program (discussed in Chapter 2). The first difference arises from the fact that the experimental data are expressed as "reduced data" (i.e., as normalized differences of exposure rates between walls with and without ducts present), whereas the models describe the exposure rate transmitted through the duct. The second difference is that the model

assumes a point detector (i.e., they predict the exposure rate at any point in the transmitted radiaton field) while the experimental program used a spherical detector with a 25.4 cm diameter. Lastly, the model is based on the use of infinite medium buildup factors while the actual experimental configuration indicates that photon buildup occurs in very restricted regions of the duct wall.

Thus it is necessary to modify the idealized model of the previous chapter to account for these three experimental complications before comparing experimental results to the different models. In the next three sections, methods for correcting the idealized model to the realities of the experiment are presented.

4.1 Prediction of Experimental Reduced Data

The results from the KSU gamma ray streaming experiment were expressed as reduced data (see Chapter 2). To obtain the reduced exposure rate at a particular observation location, the differences between the measured rates obtained through a wall with the duct and through a solid wall of the same thickness were computed. These differences were then divided by the source strength and multiplied by the square of the source-to-duct distances, ρ^2, to obtain the so-called "reduced exposure rate". In this way, data was reported that was independent of the source strength, only very weakly dependent on the source-to-duct distance, and independent of the effect of background (i.e., radiation that penetrates the solid portion of the duct wall).

In order to use the reduced data as a benchmark against which various duct penetration models can be verified, it is first necessary to modify the duct models so that they yield reduced exposure rates. Prediction of the reduced exposure rates requires that consideration be

given only to those photons that travel all or partly in the duct. Photons that penetrate the wall without ever entering the duct should be excluded from the calculated gamma-ray reduced dose. For the single-scatter models, this emphasis can be satisfied by requiring photons to scatter only in directions that enter the duct. With the direct-penetration model, on the other hand, one must calculate the actual differences between the ducted-wall and solid-wall exposure rates. No changes are needed for the double-scatter models since they are concerned only with photons traveling in the duct. The model modifications for the single-scatter and direct-penetration models are discussed below.

The change in the single-scatter models to predict reduced exposure rates take the following form. The single-scatter exposure rates are simply not evaluated for detector positions which require the photons to scatter deeper into the wall. This restriction could conceivably eliminate scatters which could contribute to the radiation field, i.e., wall scatters. But, these scattered photons would have to travel approximately the wall thickness before exiting and so would be almost entirely attenuated in the wall (assuming a wall several mean free paths thick), and hence should contribute little to the overall exposure rate.

In the direct-penetration model, buildup and attenuation through the entire wall is subtracted from Eq. (3.20). The resulting direct penetration model can thus be written as

$$\dot{X}_D = \frac{R_X(E_o)\ S_o}{4\pi R^2} \left\{ \exp[-\mu(E_o)P]\ B(E_o, \mu(E_o)P) - \exp[-\mu(E_o)P']\ B(E_o, \mu(E_o)P') \right\} \tag{4.1}$$

where P' is the photon path length in a solid concrete wall, and the other variables are as defined previously in Section 3.2.

The final change that needs to be made to the models in order to have them yield results in reduced data form is the normalization. The calculated values must be divided by the source strength (Curies) and multiplied by the square of the source distance.

4.2 Correction for a Finite Sized Detector

To account for the difference in the detector sizes used in the experiment and models, the calculated data will have to be averaged over a volume equivalent to that of the experimental detector. This averaging process acts to smooth out sharp peaks in the calculated data and will hereafter be referred to as "smoothing the data". A spatial weighting function corresponding to the detector sensitivity must be used in this smoothing. To simplify this process the following assumptions are made.

1) The spatial dependence of the exposure rate field is one-dimensional.
2) The detector sensitivity is constant throughout the detector volume (i.e., a weighted average of all point exposure rates calculated in the detector volume can be performed using equal weighting factors).

The exposure rate field dimensional dependence was taken to be along the x-axis (horizontal and parallel to the duct wall). The assumption of one dimensional dependence should incur little error since any sharp variations in the radiation field will occur in the

x-direction as long as the detector is at the duct centerline elevation and the duct height is greater than the detector diameter.

The assumption of equal weighting or constant spatial sensitivity throughout the detector will cause the peaks in the radiation field to be slightly lessened while raising any low areas or valleys. Calculations performed using different weighting functions (circular and parabolic weighting functions that are peaked at the detector center) showed that only at sharp peaks or steep valleys in the radiation fields did the radiation field profiles, calculated using different weighting functions, differ appreciably and this difference was small when compared to the peak magnitudes. For simplicity a constant weighting function was selected for the subsequent analysis. Specifically, all calculated values on both sides on a detector location within a distance of 12.7 cm (radius of the experimental detector) were added together and then divided by the number of values used (i.e., a simple average was computed). This resulting value was taken as the smoothed or experimentally equivalent value for the given point.

4.3 Buildup-Correction Factors

A buildup factor is applied as a multiplicative correction factor to the uncollided flux to account for secondary or scattered photons that are transmitted through material. These secondary photons are referred to as buildup. Generally, most of the buildup occurs in the volume immediately surrounding the path of the uncollided flux. A reduction in the material surrounding the uncollided path results in a reduction in the photon buildup.

As applied to the models in this study, the duct, as well as source collimation, acts to decrease the volume where buildup occurs. In the

scattering models developed earlier, buildup factor was an infinite medium used on the scattered leg of the photon's path. However, the buildup should be reduced because of the duct presence. In the direct-penetration model, the majority of the buildup occurs in the "near lip" on the source side of the wall and the "far lip" on the detector side of the wall from photons that are slightly deflected from their incident directions. (Note: The near lip model accounts for the direct-penetration buildup in the near lip.) Considering these facts the infinite medium buildup used in the scattered models can be expected to overpredict the exposure rates and should be reduced somewhat, while the buildup in the direct penetration model should be reduced substantially.

In the development of the buildup used in the duct models, a correction factor, B_c, was included. B_c represents the fraction of the total infinite-medium buildup that should be used in the models. Appropriate values for B_c are not easily obtained from theoretical considerations, and in this study they were determined through comparison of the models to some of the experimental data. This comparison involved adjusting the value of B_c until good visual agreement was found between plotted values of experimental data and calculated model results. A constant buildup-correction factor of 0.1 was found to be suitable for the direct penetration model. The buildup-correction factors for the scattering models were found to vary for each different duct configuration. Table 4.1 lists the values of B_c that were determined for the different duct configurations.

The variation in B_c for the scattering models can be contributed to the changes in the experimental geometry for the different duct

Table 4.1 Buildup Correction Factors determined for the various duct configurations and detector locations.

Source Strength (Ci)	Source Angle (degrees)	Source Dist. (cm)	Duct Width (cm)	Duct Height (cm)	Detector Z-coord. (cm)	B_c
0.5	33	200	30.5	30.5	201.6	0.85
0.5	33	200	30.5	30.5	251.6	0.60
0.5	33	200	30.5	30.5	351.6	0.35
0.5	45	200	30.5	30.5	201.6	0.80
0.5	45	200	30.5	30.5	251.6	0.65
0.5	45	200	30.5	30.5	351.6	0.30
0.5	60	200	30.5	30.5	201.6	1.00
0.5	60	200	30.5	30.5	251.6	0.80
0.5	60	200	30.5	30.5	351.6	0.60
0.5	33	200	30.5	15.25	201.6	0.60
0.5	33	200	30.5	15.25	251.6	0.50
0.5	33	200	30.5	15.25	351.6	0.30
10.0	45	300	30.5	15.25	201.6	0.55
20.0	45	300	30.5	15.25	251.6	0.45
20.0	45	300	30.5	15.25	351.6	0.35
20.0	60	200	30.5	15.25	201.6	0.35
20.0	60	200	30.5	15.25	251.6	0.30
20.0	60	200	30.5	15.25	351.6	0.20

configurations. The exact relation between the buildup-correction factor and the configuration geometry is not known, but some simple empirical approximations can be formed. Using the values for B_c in Table 4.1, two empirical expressions for the buildup-correction factor were developed (least squares fits). The scattering model buildup-correction factor for the square ducts (30.5 cm x 30.5 cm) can be approximated by

$$B_c = 0.75 + \frac{0.273}{\cos\theta_s} - 0.142\,\frac{c}{L} \qquad (4.2)$$

where c is the distance from the back of the duct wall to the detector, L is the duct length, and θ_s is the source angle. The buildup-correction factor in the scattering models used for the rectangular ducts (30.5 cm wide x 15.25 cm high) can be approximated by

$$B_c = 0.99\text{i} - \frac{0.232}{\cos\theta_s} - 0.142\,\frac{c}{L}\,. \qquad (4.3)$$

In effect B_c introduces a single free parameter to the duct penetration models. The values for this parameter (B_c) should be determined from comparison of the model results to experimental data. But, for calculations requiring only order-of-magnitude results, a constant value of B_c (between zero and one) can be choosen. Using a constant value of B_c should result in duct penetration model predictions that are within a factor of two for peak exposure rate regions.

4.4 Elimination of Models Providing Insignificant Contributions

Some of the models developed in Chapter 3 for different components of the exposure rate were found to contribute insignificantly to the

overall gamma-ray streaming. These models included the top and bottom lip models and both double-scatter models. The top and bottom lip models generally contributed less than one percent of the total reduced data values. The double-scatter models contributed slightly more, ranging from around two percent in the peak exposure regions to close to ten percent at the limits of the detector traverse (x_d = -150 cm and x_d = 150 cm). At the detector positions where the double-scatter models accounted for close to ten percent of the exposure rate the total exposure rate was usually very small (less than 10 $\mu R\ m^2/Ci\ h$). Since the above mentioned models have relatively negligible contributions to the overall gamma-ray streaming dose, they were not used. These models were included in the development in Chapter 3 in order that the overall model development should be complete.

4.5 Comparison of the Single-Scatter and Albedo Models

In order to compare the effectiveness of the single-scatter with the albedo wall scattering components developed in Section 3.4, these components were combined (separately) with the duct lip and direct penetration components and then compared to experimental data. These two composite models were evaluated with buildup-correction factors of 0.0 and 1.0 at detector x-locations ranging from -150 cm to 150 cm for duct configurations with source angles of 33, 45, and 60 degrees. The resulting reduced data were then plotted (separate plots for each duct configuration and B_c value) yielding a total of six plots. Included on each plot were the experimental data, the data obtained from the composite model with the single-scatterwall-scattering components, and data obtained from the composite model with the albedo based wall-scattering components. The duct configuration and the B_c value are

identified in the upper right corner of each plot. The plots are shown in Figs. 4.1 through 4.6.

Figures 4.1 through 4.6 show that the single-scatter model predicts the experimental results better than the albedo model. In Figs. 4.1 through 4.3 the models used no buildup ($B_c = 0$) and the single-scatter model predicted values which were slightly higher than those predicted by the albedo model and the experimental values were higher yet. Figures 4.4 through 4.6 ($B_c = 1$) show generally good agreement between the experimental data and the single-scatter models, but very poor agreement of the experimental data with the albedo models. It can be concluded from these comparisons that the models using the albedo technique, which have buildup at the scattering point incorporated in their empirical albedo formulas, are unresponsive to changes in the buildup correction factor, and that these albedo models predict values that are less than one half of the experimental reduced data values. The single-scatter models, on the other hand, are very responsive to changes in the buildup correction factor and can achieve good agreement with the experiment.

The single-scatter model will be used for all subsequent comparisons of experimental and predicted exposure rates since the albedo-based model is not as accurate as the former.

4.6 Characteristics of the Principal Model Components

The composite model used to predict the reduced exposure rate field is a sum of the various individual model components each of which predicts the reduced exposure rate arising from radiation transmitted by a different mechanism. Each of these model components predicts a different spatial contribution to the composite reduced exposure rate

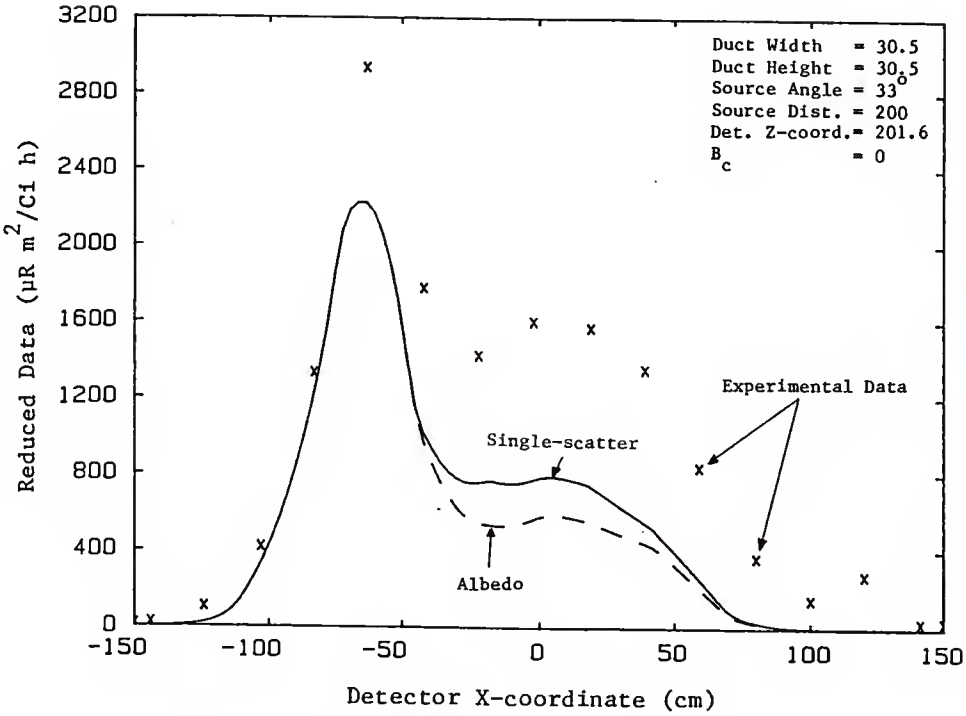

Fig. 4.1. Graphical comparison of the single-scatter based duct wall models vs. the albedo based duct wall models for a 101.6 cm thick duct wall.

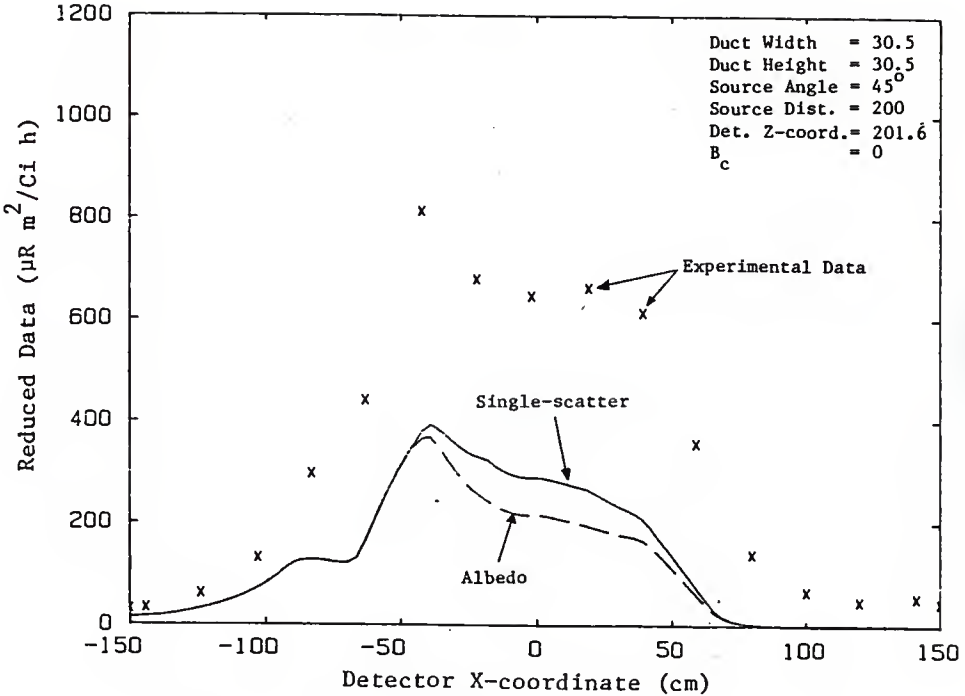

Fig. 4.2. Graphical comparison of the single-scatter based duct wall models vs. the albedo based duct wall models for a 101.6 cm thick duct wall.

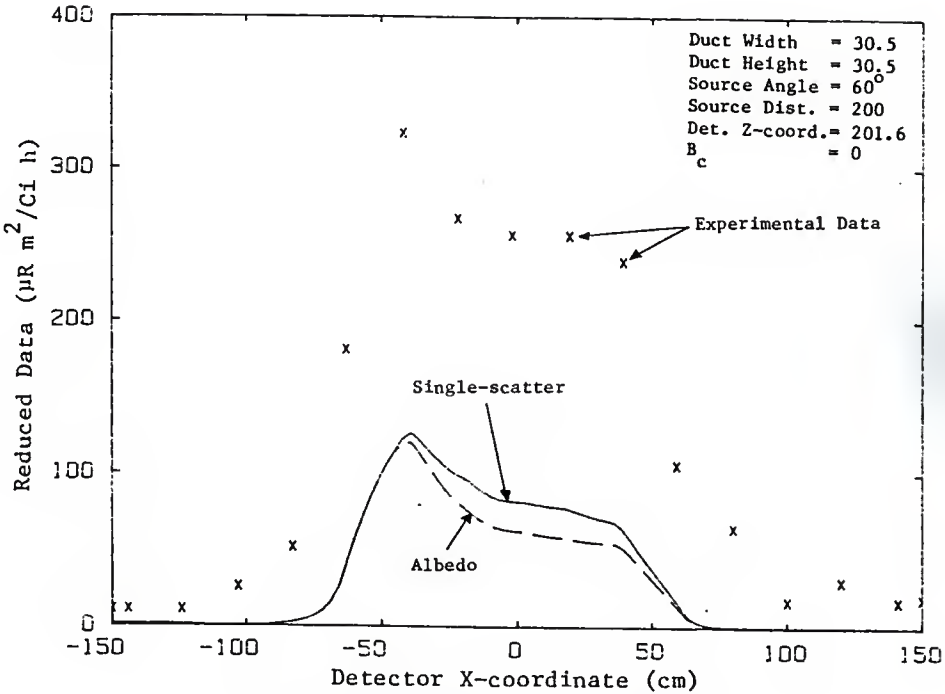

Fig. 4.3. Graphical comparison of the single-scatter based duct wall models vs. the albedo based duct wall models for a 101.6 cm thick duct wall.

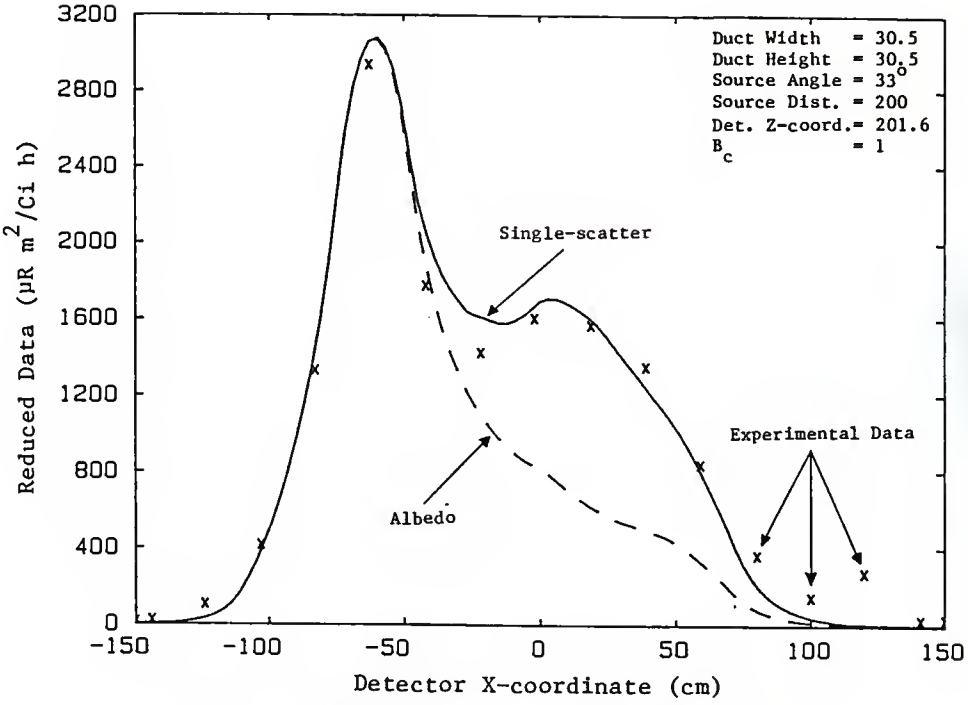

Fig. 4.4 Graphical comparison of the single-scatter based duct wall models vs. the albedo based duct wall models for a 101.6 cm thick duct wall.

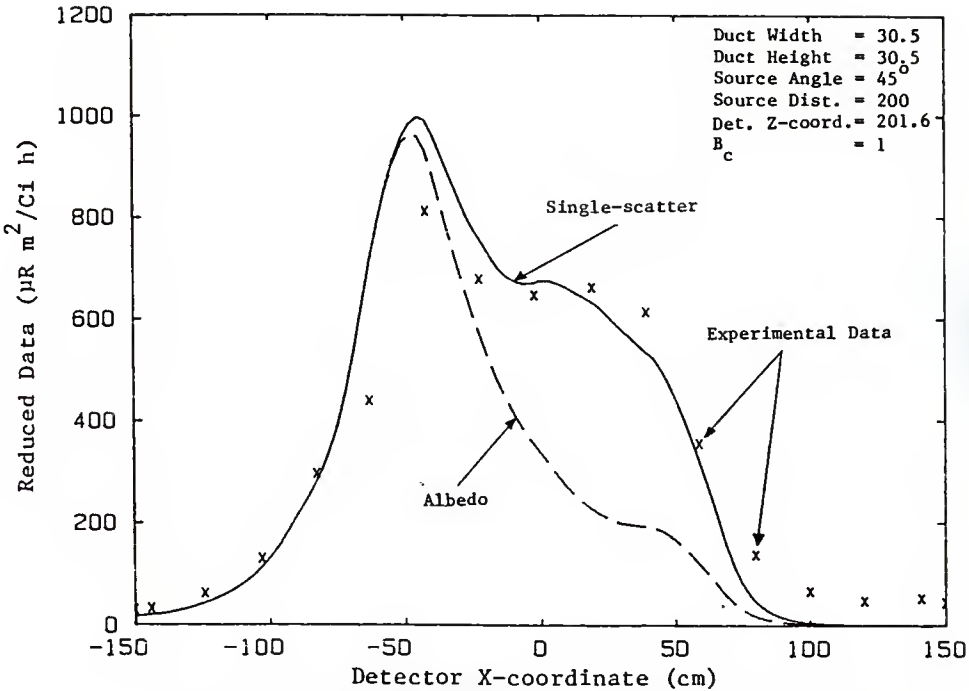

Fig. 4.5. Graphical comparison of the single-scatter based duct wall models vs. the albedo based duct wall models for a 101.6 cm thick duct wall.

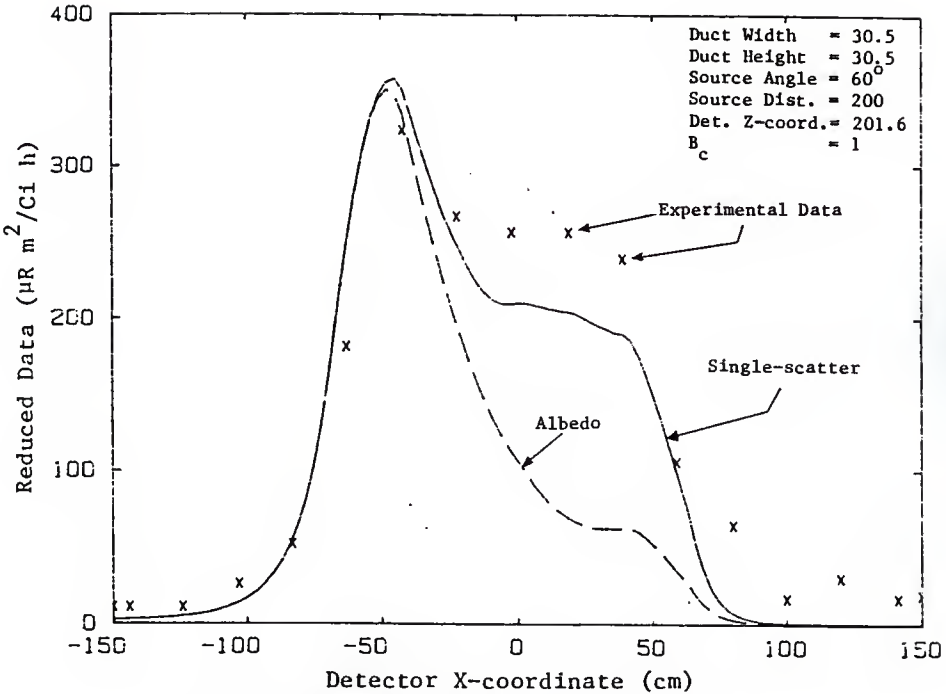

Fig. 4.6. Graphical comparison of the single-scatter based duct wall models vs. the albedo based duct wall models for a 101.6 cm thick duct wall.

field. Figures 4.7 through 4.9 illustrate the shapes of the different reduced exposure rate components generated from the various models and how they contribute to the composite field. The figures were generated for duct configurations with source angles of 33, 45, and 60 degrees. These configurations are representative of the ones studied in this work and present the variations in exposure rate field shape and relative magnitude for the different components.

Figures 4.7 through 4.9 show how the relative contributions of the different components change as the source beam illuminates the duct mouth at increasing angles from the duct axis. The direct-penetration component is very prominant when the source angle is 33 degrees (fig. 4.7). But, as the source angle increases, the effects of the source collimation and increased attenuation cause the direct penetration contribution to decrease until, at a source angle of 60 degrees, there is a negligible direct-penetration contribution.

The duct-lip contributions behave just the opposite of the direct-penetration component. The relative contribution from the near and far duct lips increases with increasing source angle. This increase is to be expected, since the size of the duct lips do not change with increasing source angle whereas the wall scattering area decreases. The far duct-lip model shows very slight relative increases in its contribution as the source angle increases because of the acute scattering angle encountered by photons scattering in the far duct lip.

The only major variation in the duct-wall scatter contributions as the source angle varies is that they extend over a smaller detector traverse area. This smaller spatial range is due to the fact that the scatters are originating closer to the duct entrance and thus are more restricted by the duct exit walls as the source angle increases.

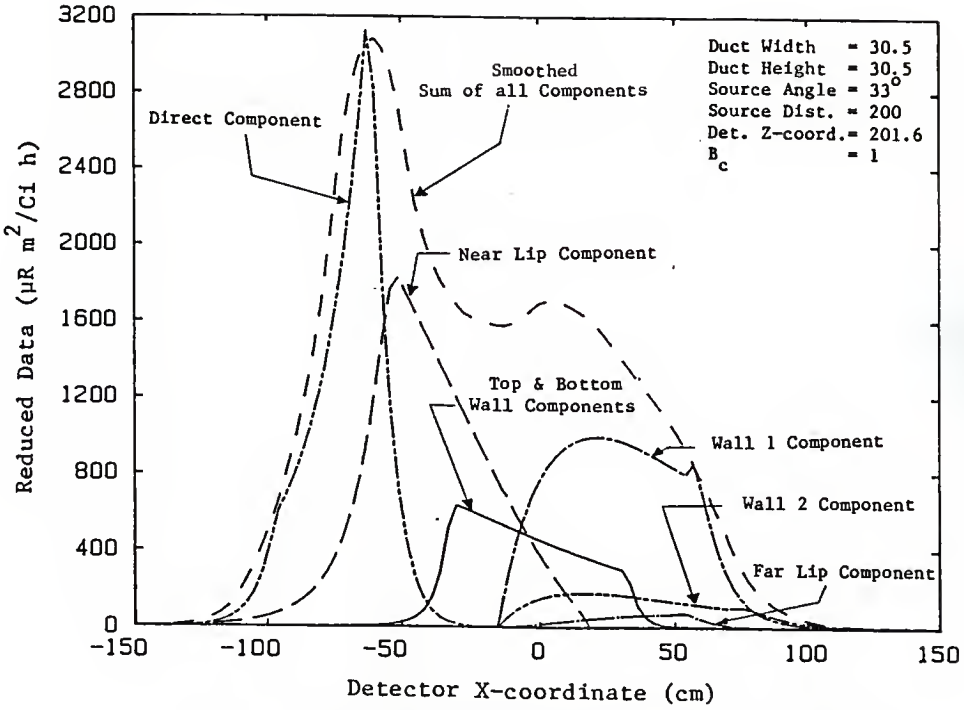

Fig. 4.7. Illustration of the contributions of the various model components (source angle = 33 degrees).

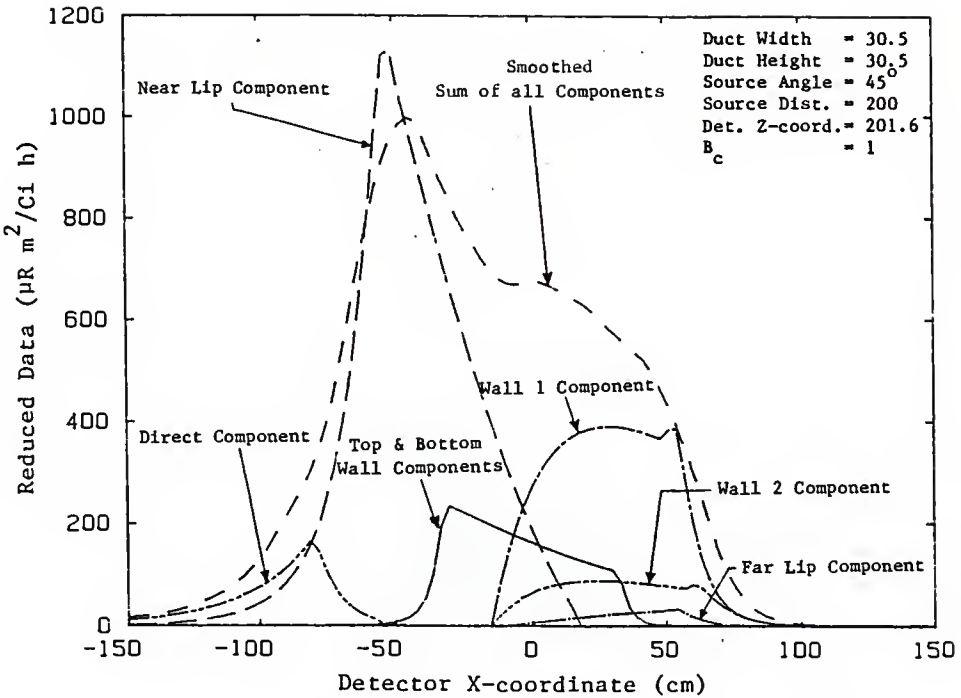

Fig. 4.8. Illustration of the contributions of the various model components (source angle = 45 degrees).

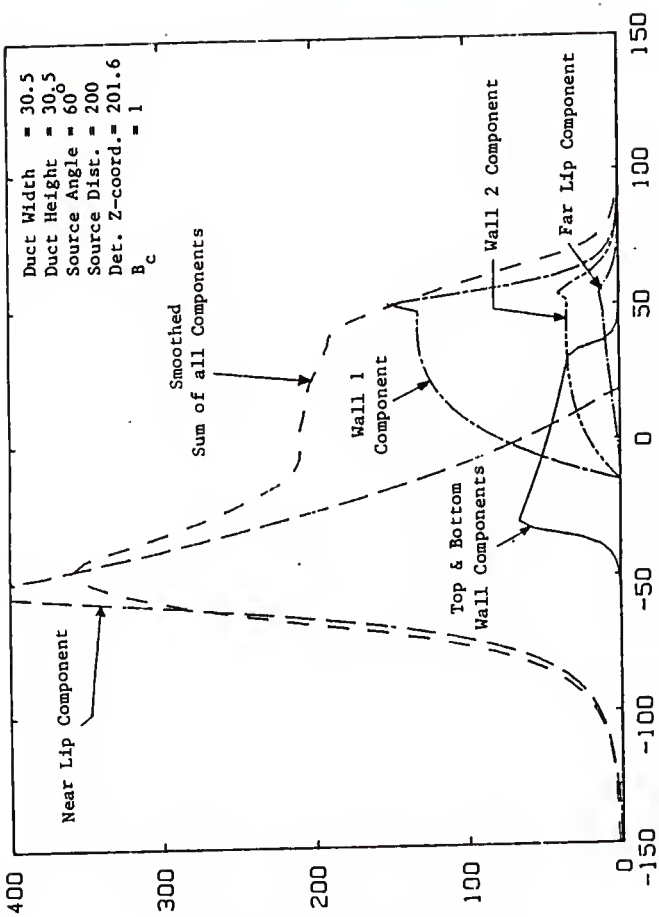

Fig. 4.9. Illustration of the contributions of the various model components (source angle = 60 degrees).

4.7 Comparison of the Models to the Experimental Data

A measure of how well the models fit or compare to the experimental data is difficult to obtain. There appears to be no one ideal method for making such comparisons; however, a measure of agreement between the models and experimental data can be obtained by computing the sample correlation coefficient. A sample correlation coefficient is the measure of the linear association between two variables, such as experimental data and values obtained from the models. When the models provide a perfect fit to the experimental data the degree of linear association is maximized. The sample correlation coefficient can be determined, for a given set of experimental and corresponding model predicted values, from [12]

$$r = \frac{\sum_{i=1}^{n} (Y_i-\bar{Y})\,(\hat{Y}_i-\bar{\hat{Y}})}{\left[\sum_{i=1}^{n} (Y_i-\bar{Y})^2 \sum_{i=1}^{n} (\hat{Y}_i-\bar{\hat{Y}})^2\right]^{1/2}} \tag{4.4}$$

where r is the sample correlation coefficient, n is the number of experimental data points, Y_i are the experimental data, $\hat{Y}_i$ are the values obtained from the models, $\bar{Y}$ is the average or mean of the experimental data, and $\bar{\hat{Y}}$ is the mean of the model predicted values. The values of the sample correlation coefficient can vary from negative one to positive one. A value of positive one indicates a perfect positive correlation between the variables being compared. A value of negative one indicates a perfect negative correlation between the variables. If the sample correlation coefficient is zero, the variables are said to be uncorrelated [12].

Sample correlation coefficients were calculated for detector x-axis traverses in the various experimental duct configurations studied. Seventeen experimental data points and model predicted values were used in the calculation of the sample correlation coefficients. These values are reported in Table 4.2. Graphs of the experimental data and model predictions (detector x-coordinate vs. reduced data) are shown in Figs. A.1 through A.18 in Appendix A. As seen from the sample correlation coefficients and Figs. A.1 through A.18, the models generally provided an excellent fit to the experimental data. The average of the calculated r^2 values was 0.927 with the majority of the individual r^2 values being between 0.9 and 1.0.

The worst r^2 value reported was 0.606. This low value appears to be caused by the use of too large a build up factor in the models for the particular configuration. The general shape of the exposure rate field predicted by the model (see Fig. A.12) agrees with that of the experiment, but the magnitude of the model predicted values are high.

Although the sample correlation coefficient could be used to provide an indication of how well the models predict the experimental data, it must be realized that the r values are insensitive to cases in which there is a constant bias between the experimental and model predicted data. The sample correlation coefficient indicates the degree to which the model predicts the shape of the exposure rate field, not how close the model values compare to the actual experimental values. This is illustrated when Figs. A.9 and A.12 are considered. The r values ($r \approx 0.902$ for Fig. A.9 and $r = 0.606$ for Fig. A.12) seem to indicate that the model fits the experimental data in Fig. A.9 better than in Fig. A.12. This can be misleading since the figures indicate

Table 4.2 Correlation coefficients (see Section 4.6) for the various duct configurations and detector locations. (Duct Width is 30.5 cm for all configurations)

Source Strength (Ci)	Source Angle (degrees)	Source Dist. (cm)	Duct Width (cm)	Duct Height (cm)	Detector Z-coord. (cm)	Correlation Coefficient *
0.5	33	200	30.5	30.5	201.6	0.993
0.5	33	200	30.5	30.5	251.6	0.980
0.5	33	200	30.5	30.5	351.6	0.923
0.5	45	200	30.5	30.5	201.6	0.976
0.5	45	200	30.5	30.5	251.6	0.971
0.5	45	200	30.5	30.5	351.6	0.903
0.5	60	200	30.5	30.5	201.6	0.966
0.5	60	200	30.5	30.5	251.6	0.963
0.5	60	200	30.5	30.5	351.6	0.902
0.5	33	200	30.5	15.25	201.6	0.994
0.5	33	200	30.5	15.25	251.6	0.990
0.5	33	200	30.5	15.25	351.6	0.606
10.0	45	300	30.5	15.25	201.6	0.956
10.0	45	300	30.5	15.25	251.6	0.935
10.0	45	300	30.5	15.25	351.6	0.838
10.0	60	200	30.5	15.25	201.6	0.990
10.0	60	200	30.5	15.25	251.6	0.978
10.0	60	200	30.5	15.25	351.6	0.935
					Average	0.927

* Calculated using Eq. (4.4).

that the model provides a better fit for the duct configuration of Fig. A.12. Thus when evaluating the model comparisons, the sample correlation coefficient should be used in conjunction with the figures in Appendix A. Overall it appears that the model predicted the shape of the exposure rate fields very well for the duct configurations with source angles of 33 and 45 degrees. In the duct configurations with source angles of 60 degrees, however, the model was unable to predict the exposure rate peaks occurring at the positive detector x-coordinates. The author does not know the reason for this model failure, but suggests that further study in this field may lead to an answer.

4.8 Effect of Duct Geometry on Transmitted Radiation

Changes in the duct geometry or configurations have noticeable effects on the reduced exposure rate fields predicted from the models. Below is a discussion of some of the effects encountered for changes in the duct type and detector z-coordinate. The effect of changes in source angle was previously discussed in Section 4.6.

Rectangular ducts (30.5 cm wide x 15.25 cm high) were found to exhibit the same behavior as the square ducts for changes in source angle and detector z-coordinate. However, the magnitudes of the radiation fields predicted for the rectangular ducts were found to be approximately one half of those predicted for the square ducts (except in cases where there is a substantial direct-penetration contribution, i.e., source angle = 33 degrees). This is to be expected since the rectangular ducts were half the height of the square ducts and thus had lip and side wall regions (primary scattering regions) that were one half the size of those in the square ducts. The top and bottom wall

components displayed little change between the rectangular and square ducts. There is no change in the reduced exposure rates calculated for the direct-penetration component for the square and rectangular ducts.

Increases in the detector z-coordinate caused the reduced exposure rate profiles to become flatted and lower in magnitude. As the detector moves farther from the wall (increases z-coordinate), the distances from the source and scatter points to the detector increase. These distances appear in the model formulations as inverse square quantities, thus reducing the model predicted exposure rates as these distances increase.

Figures 4.10 through 4.15 illustrate the changes in the predicted reduced exposure rate field resulting from gamma rays streaming through the square ducts (30.5 cm x 30.5 cm). In Figs. 4.10 through 4.12 the overall effect of changes in source angle are shown for configurations with the detector traversing the x-axis at z-coordinates of 201.6, 251.6, and 351.6 cm, respectively. Figures 4.13 through 4.15 illustrate the effect of changes in the detector z-coordinate for the different source angles that were studied.

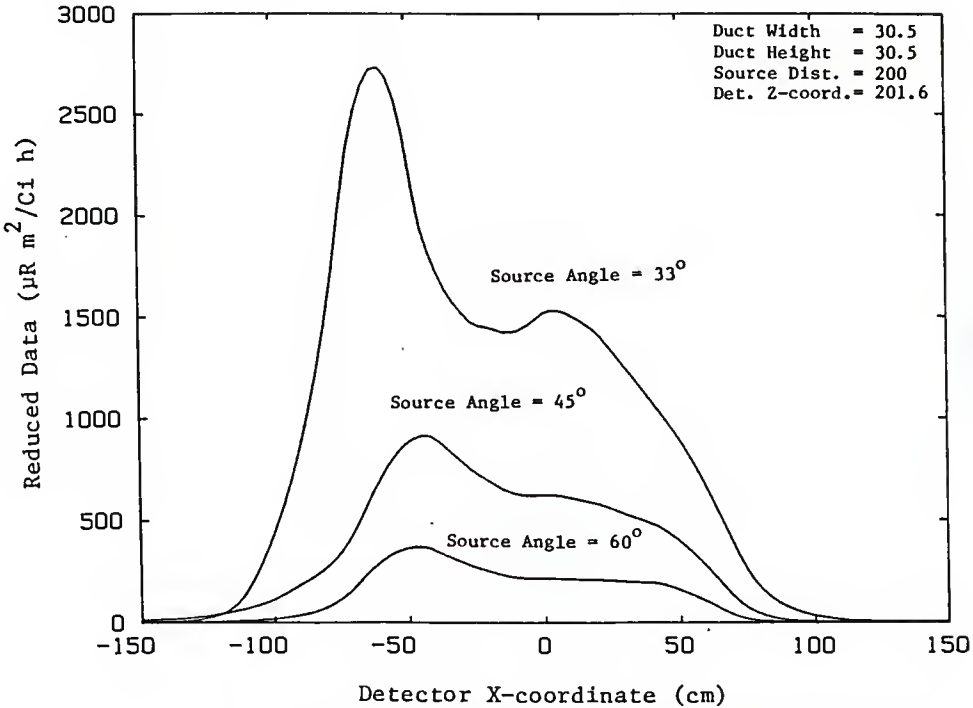

Fig. 4.10. Variation of the reduced data exposure rate fields as a function of the detector x-coordinate and source angle with the detector z-coordinate equal to 201.6 cm.

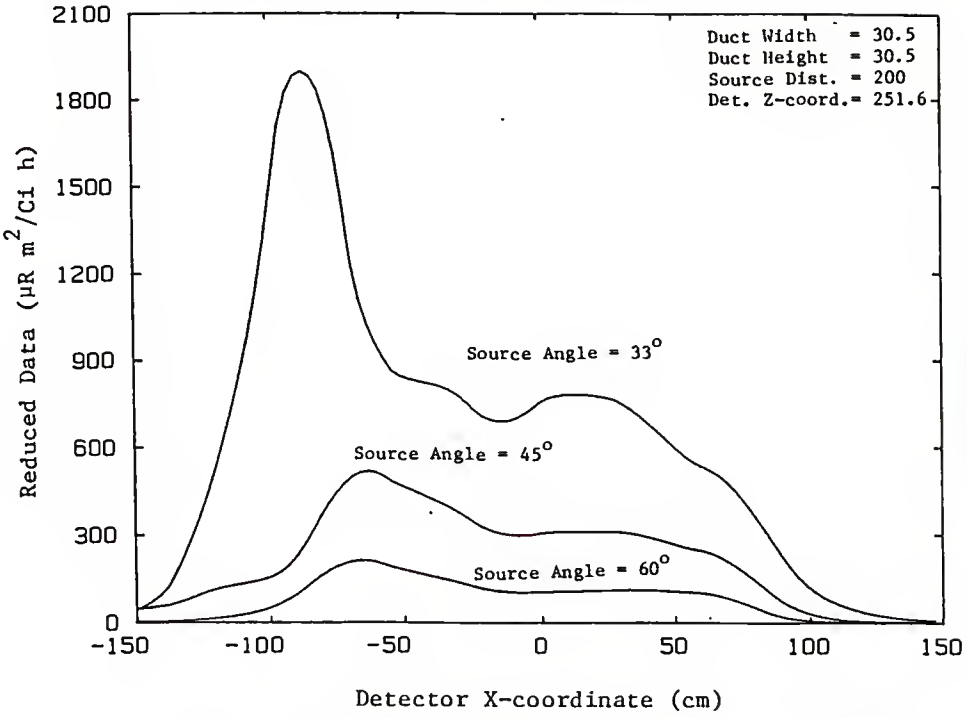

Fig. 4.11. Variation of the reduced data exposure rate fields as a function of the detector x-coordinate and source angle with the detector z-coordinate equal to 251.6 cm.

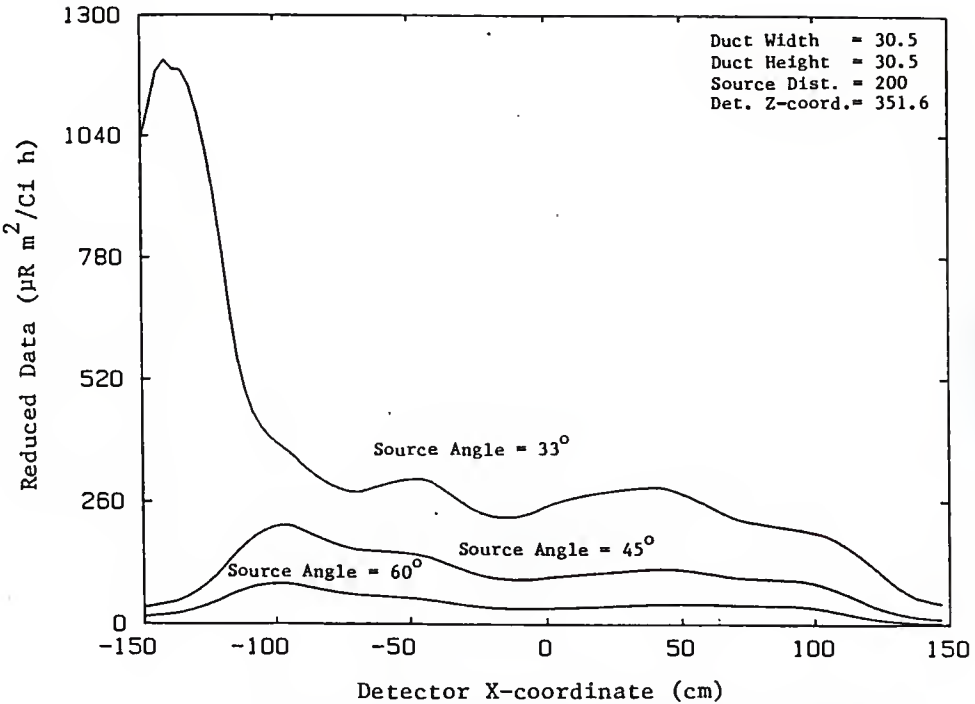

Fig. 4.12. Variation of the reduced data exposure rate fields as a function of the detector x-coordinate and source angle with the detector z-coordinate equal to 351.6 cm.

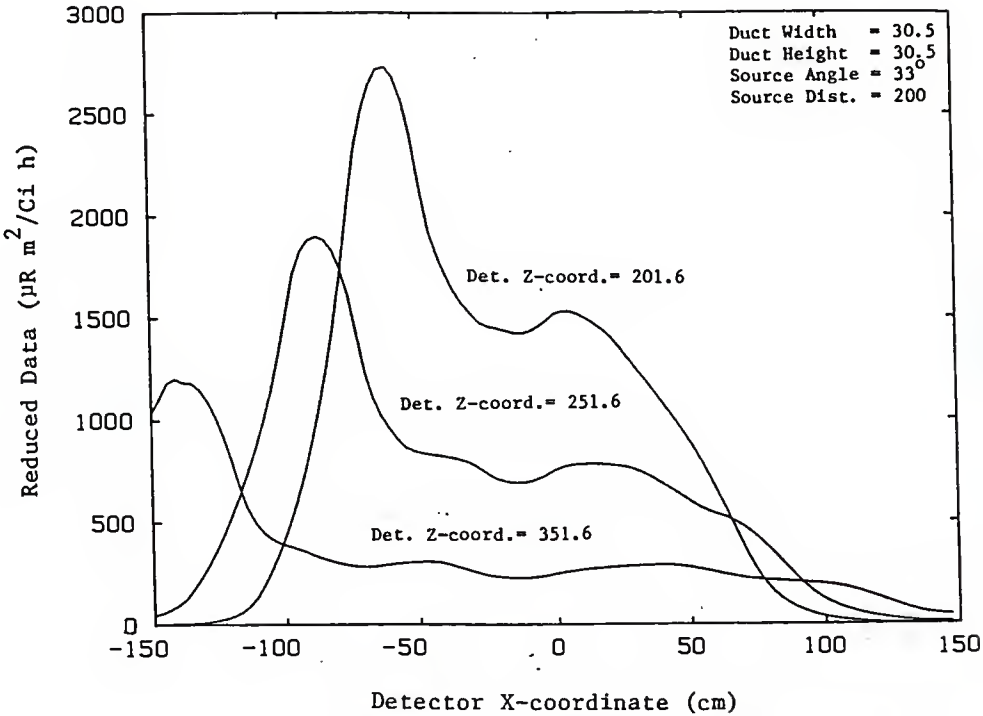

Fig. 4.13. Variation of the reduced data exposure rate fields as a function of the detector x and z-coordinates with the source angle equal to 33 degrees.

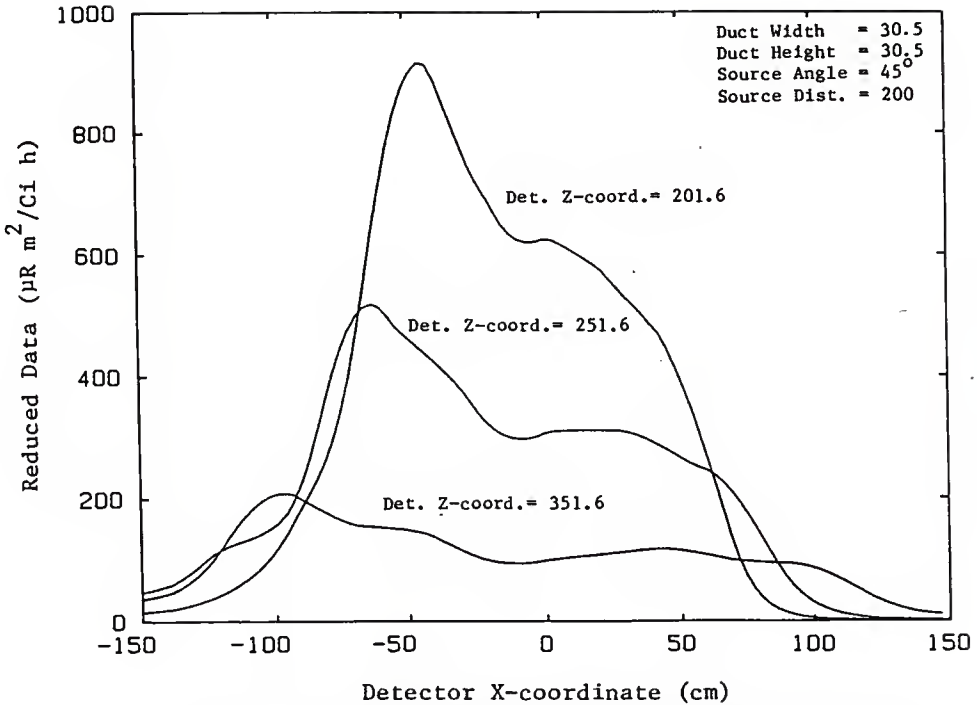

Fig. 4.14. Variation of the reduced data exposure rate field as a function of the detector x and z-coordinates with the source angle equal to 45 degrees.

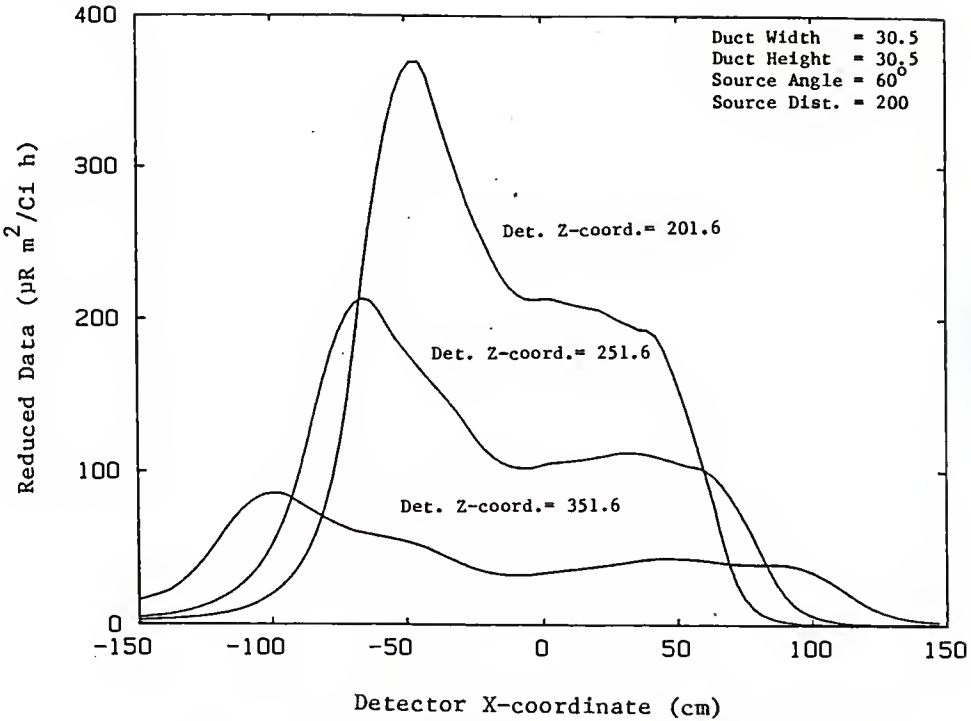

Fig. 4.15. Variation of the reduced data exposure rate fields as a function of the detector x and z-coordinates with the source angle equal to 60 degrees.

CHAPTER 5

CONCLUSIONS, MODEL LIMITATIONS, AND RECOMMENDATIONS FOR FURTHER STUDY

Presented in the following sections are the conclusions obtained from this study, a brief summary of the major limitations of the model, and recommendations for further study.

5.1 Conclusions

The most important result of this work has been finding that the single-scatter method for describing gamma-ray scatters could be used for all the single scattering model. Variations of this approach are commonly used to describe photon scatters in the duct lip regions, but for photons scattering from wall surfaces albedo techniques are generally used. It was found that, for the cases studied, the albedo based models underpredicted the wall scattered dose. Comparison of the models to experimental data showed that the single scatter based models are surprisingly accurate tools for prediction of photons streaming through ducts.

Another important finding was that the scattered-photon buildup factor depends on the detector and source positions in relation to the duct. This finding was substantiated through comparison of experimental data to the model-predicted values using different experimental configurations and different model buildup correction factors. It was found that the models required a lower value of the photon buildup on the scattered photons the farther the detector was from the duct wall. Also, a lower value of the photon buildup factor could generally be used as the source angle increased. The exact relation between buildup and geometry involved is not known from a theoretical standpoint. However, simple empirical formulas applied as buildup correction factors proved effective.

5.2 Model Limitations

The models developed in Chapter 3 and later modified in Chapter 4 were developed for a specific set of conditions. These models were developed to describe the radiation field, at the duct centerline elevation, resulting from gamma rays streaming through ducts. The type of duct allowed in the models was restricted to ones with rectangular cross sections. Also, only concrete ducts were considered. These limitations were imposed upon the models in order that the modeling task could be simplified. These limitations, however, should not be considered as fundamental.

The models can also be adapted to calculate the radiation fields at off-centerline elevations. The scattering models need not be changed, only the calculation of the exit path of the scattered photons after they have left the scattering region needs to be redetermined. In using this method to achieve off-centerline model predictions it must be assumed that the photon paths in the scattering regions do not change appreciably with changes in the detector elevation.

The present form of the models is not designed to handle nonrectangular ducts. Nevertheless, the principles behind the model derivations can be applied to essentially any duct configuration. In applying these principles, however, it might be necessary to subdivide the scattering regions into numerous smaller regions.

Lastly, modifying the models to account for ducts in materials other than concrete should prove fairly simple. All that needs to be done is to replace the empirical formulas for the total attenuation coefficient and buildup factors in concrete with ones developed for the material of interest.

5.3 Recommendations for Further Study

The most interesting recommendation for further research is that of adapting the models to be used for off-centerline detector elevations. This could conceivably be accomplished by using multiple scatter points, at different elevations, for the various models. The major difficulty involved would be the determination of a simple method to calculate the scattered photon's exit path in the duct wall. The KSU gamma ray streaming experiment provided a large amount of data on the off-centerline measurements in addition to the data on the centerline measurements.

A further recommendation is that a comprehensive study of the photon buildup in finite shields be performed. This could lead to a more accurate calculation of the buildup correction factor, or possibly an empirical formula describing buildup in finite shields. Another result of this type of study could be a better understanding of the regions of importance in the duct wall.

Finally, a study of whether models developed to describe gamma-ray streaming through rectangular ducts could be used for cylindrical ducts or vice versa. This question needs to be addressed in order to develop truly general models describing how gamma rays stream through ducts.

CHAPTER 6

ACKNOWLEDGEMENTS

The author wishes to express his appreciation to Professor J. K. Shultis for his guidance and suggestions throughout the course of this research. The technical support provided by Professor R. E. Faw was also much appreciated.

Additionally, the author wishes to thank the Nuclear Engineering graduate students at KSU for their assistance and support.

Lastly, the author wishes to express his deepest appreciation to his wife for her support and understanding.

CHAPTER 7

REFERENCES

1. Rockwell, T. III ed., Reactor Shielding Design Manual, pp. 290-292, D. Van Nostrand Company, Inc., Princeton, New Jersey, 1956.

2. LeDoux, J. C., and A. B. Chilton, "Attenuation of Gamma Radiation Through Two-Legged Rectangular Ducts and Shelter Entranceways--An Analytical Approach," NCEL-TN-383, U.S. Naval Civil Engineering Laboratory, Port Hueneme, California, 1961.

3. Kitazume, M., and J. Miyakoshi, "Gamma-Ray Streaming Through a Straight Cylindrical Duct," Nuclear Science and Engineering, 27, pp. 450-463, 1967.

4. Clifford, C. E., "Gamma-Ray Streaming in Concrete Ducts Model Development and Benchmark Experiments," Final Report, RRA-T8003, Radiation Research Associates, Fort Worth, Texas, February, 1980.

5. Simons, G. G., R. E. Faw, J. K. Shultis, and D. L. Stucker, Benchmark Gamma-Ray Streaming Experiments Final Report, Department of Nuclear Engineering, Kansas State University, Manhattan, Kansas, January, 1980.

6. Stucker, D. L., "Measurement and Analysis of Gamma-Ray Streaming through Concrete Lined Ducts," M.S. Thesis, Kansas State University, 1980.

7. De Campo, J. A., H. L. Beck, and P. D. Raft, "High Pressure Argon Ion Chamber Systems for the Measurement of Environmental Exposure Rates," USAEC Report HASL-260, December, 1972.

8. Storm, E., and H. I. Israel, Photon Cross Sections from 0.001 to 100 MeV for Elements 1 through 100, Report LA-3753 Los Alamos Scientific Laboratory, Los Alamos, New Mexico, 1967.

9. Chilton, A. B., J. K. Shultis, and R. E. Faw, Principles of Radiation Shielding, pp. 38, 41, 266, 270, and 276, Prentice-Hall, Inc., Englewood Cliffs, New Jersey, 1984.

10. Eishenhauer, C. M., and G. L. Simmons, "Point Isotropic Gamma-Ray Buildup Factors in Concrete," Nuclear Science and Engineering, 56, pp. 263-270, 1975.

11. Chilton, A. B., and C. M. Huddleston, "A Semiempirical Formula for Differential Dose Albedo for Gamma Rays on Concrete," Nuclear Science and Engineering, 17, pp. 419-424, 1963.

12. Draper, N. R., H. Smith, "Applied Regression Analysis," pp. 43 and 44, John Wiley and Sons, New York, New York, 1966.

APPENDIX A

The figures presented in this section were generated on a Hewlett Packard 9816 computer using a HP7470A plotter. Each figure has a legend in the upper right hand corner identifying the duct configuration corresponding to the plotted data. Table A.1 presents a summary of the various figures and their figure numbers. All configurations listed below are for 101.6 cm thick walls with duct widths of 30.5 cm.

Table A.1

Source Strength (Ci)	Source Angle (degrees)	Source Dist. (cm)	Duct Height (cm)	Detector Z-coord. (cm)	Figure Number
0.5	33	200	30.5	201.6	A.1
0.5	33	200	30.5	251.6	A.2
0.5	33	200	30.5	351.6	A.3
0.5	45	200	30.5	201.6	A.4
0.5	45	200	30.5	251.6	A.5
0.5	45	200	30.5	351.6	A.6
0.5	60	200	30.5	201.6	A.7
0.5	60	200	30.5	251.6	A.8
0.5	60	200	30.5	351.6	A.9
0.5	33	200	15.25	201.6	A.10
0.5	33	200	15.25	251.6	A.11
0.5	33	200	15.25	351.6	A.12
10.0	45	300	15.25	201.6	A.13
10.0	45	300	15.25	251.6	A.14
10.0	45	300	15.25	351.6	A.15
10.0	60	200	15.25	201.6	A.16
10.0	60	200	15.25	251.6	A.17
10.0	60	200	15.25	351.6	A.18

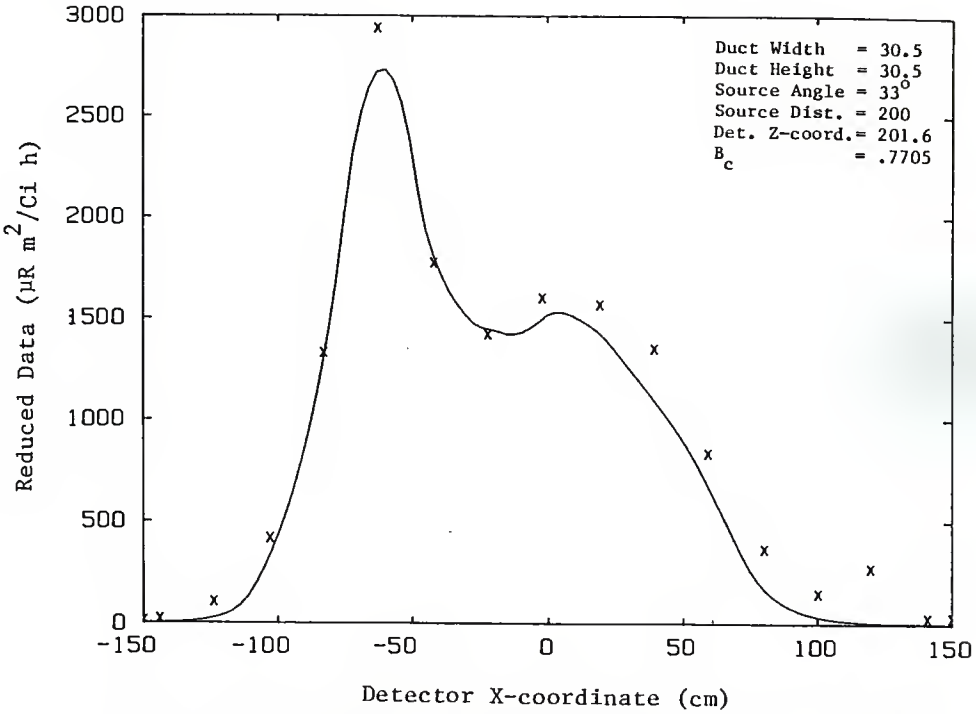

Fig. A.1. Comparison of the duct streaming model to the experimental data. (Solid line = model predicted values, X's = experimental data)

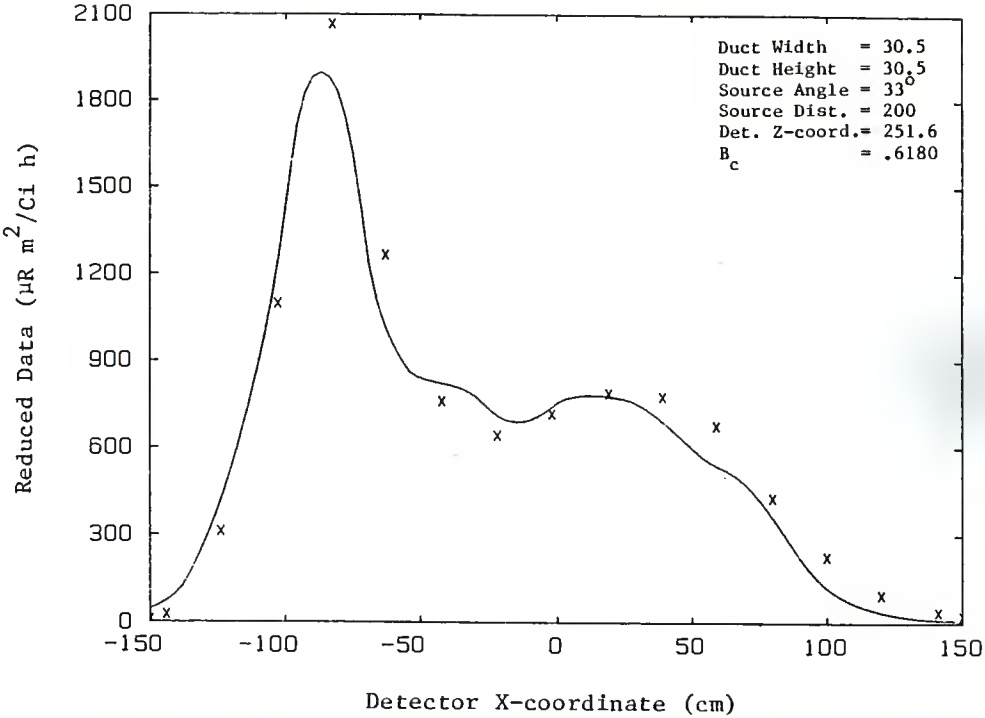

Fig. A.2. Comparison of the duct streaming model to the experimental data. (Solid line = model predicted values, X's = experimental data)

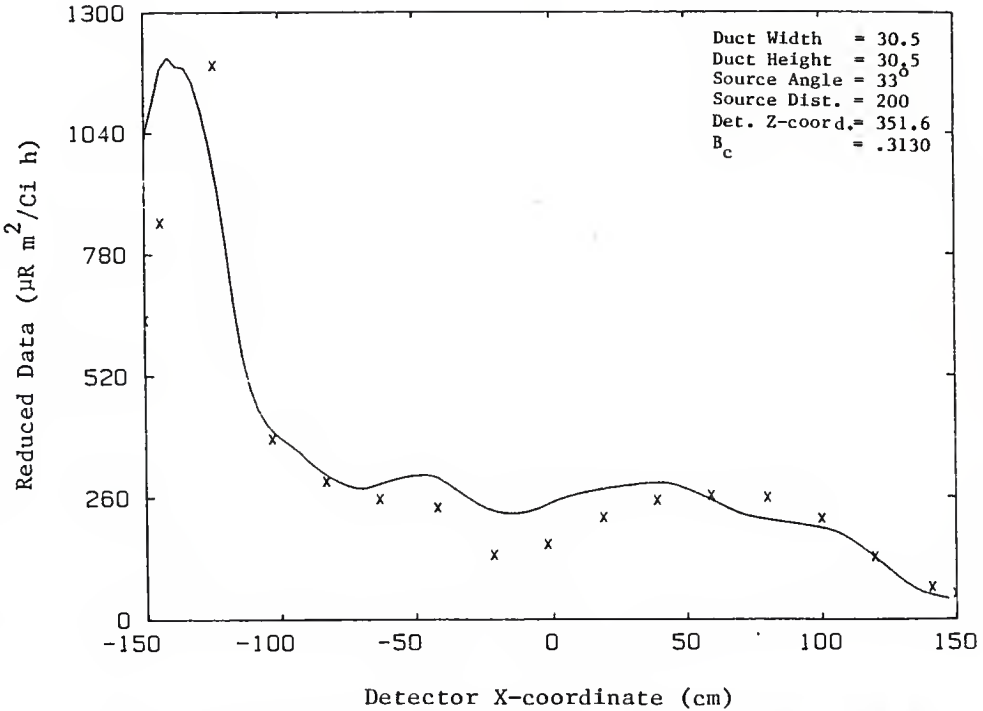

Fig. A.3. Comparison of the duct streaming model to the experimental data. (Solid line = model predicted values, X's = experimental data)

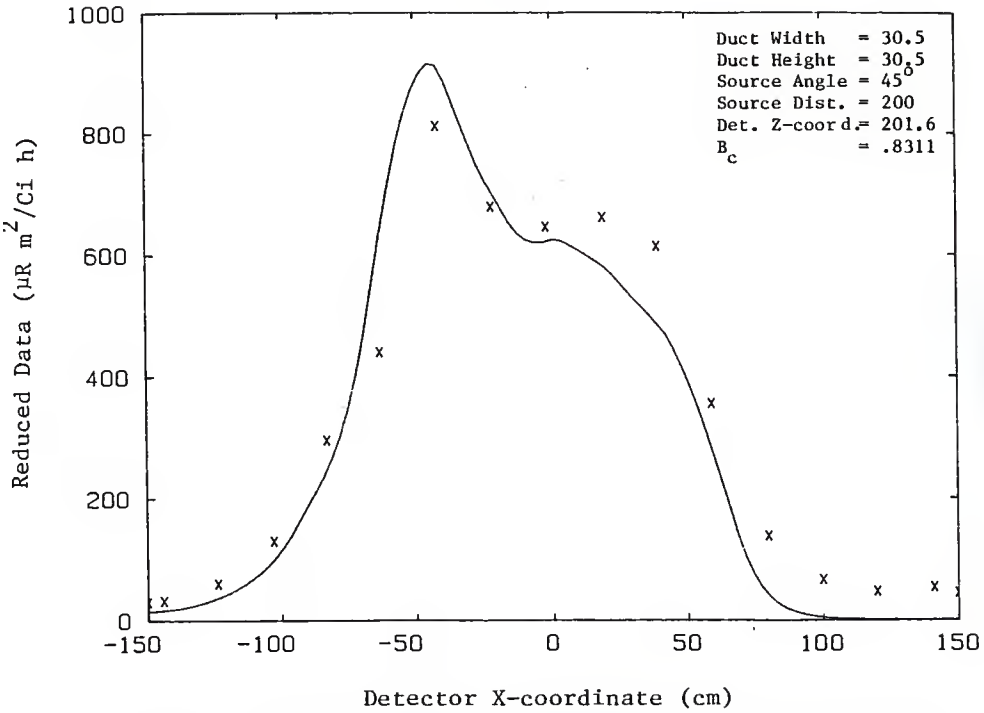

Fig. A.4. Comparison of the duct streaming model to the experimental data. (Solid line = model predicted values, X's = experimental data)

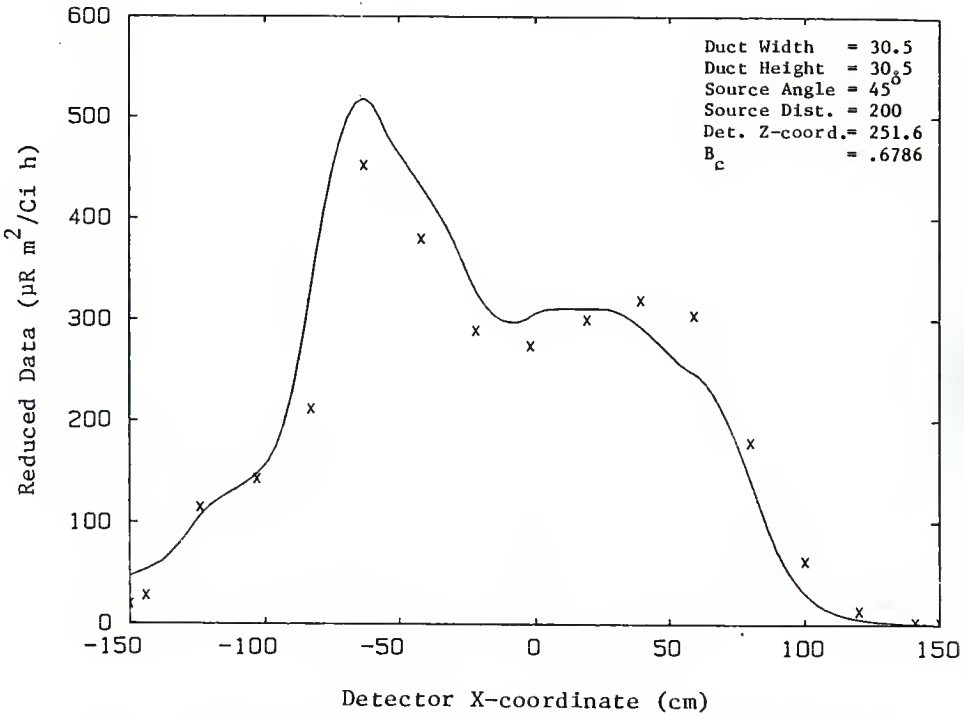

Fig. A.5. Comparison of the duct streaming model to the experimental data. (Solid line = model predicted values, X's = experimental data)

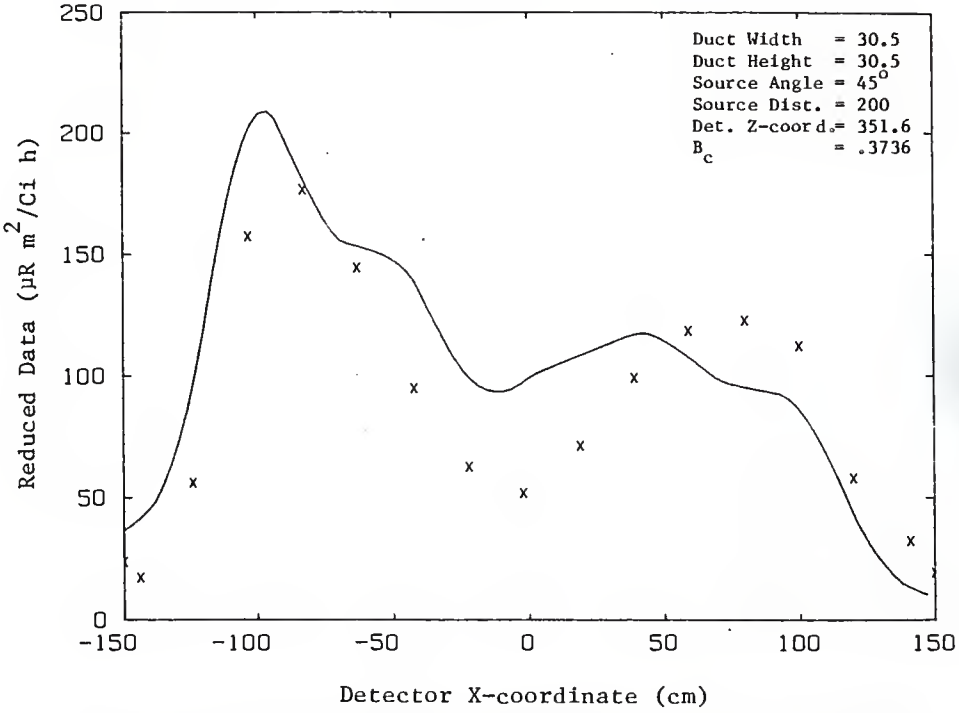

Fig. A.6. Comparison of the duct streaming model to the experimental data. (Solid line = model predicted values, X's = experimental data)

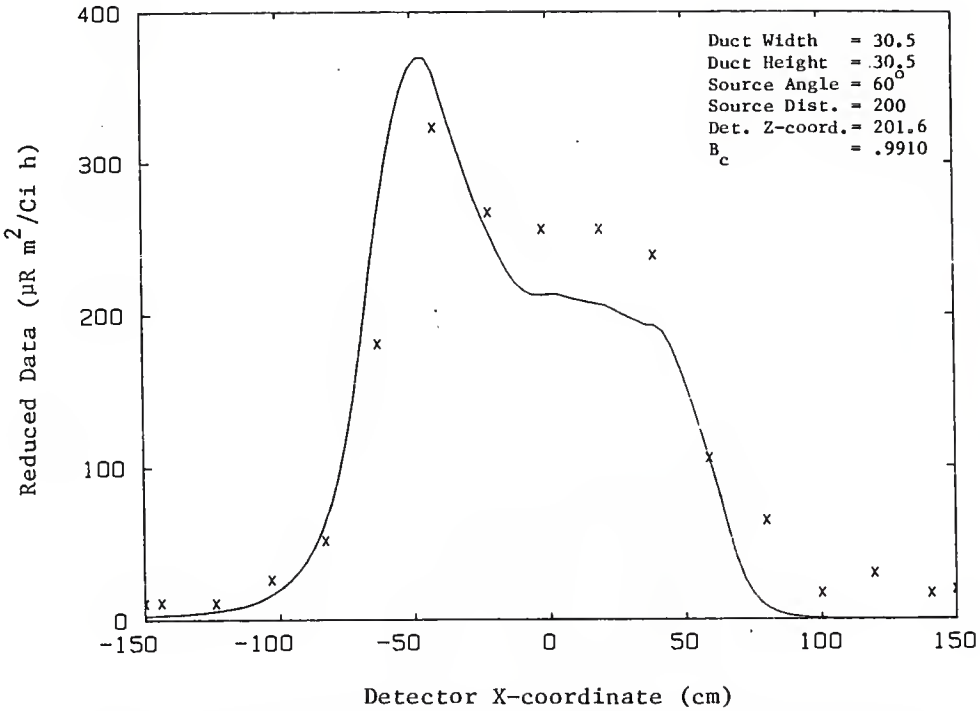

Fig. A.7. Comparison of the duct streaming model to the experimental data. (Solid line = model predicted values, X's = experimental data)

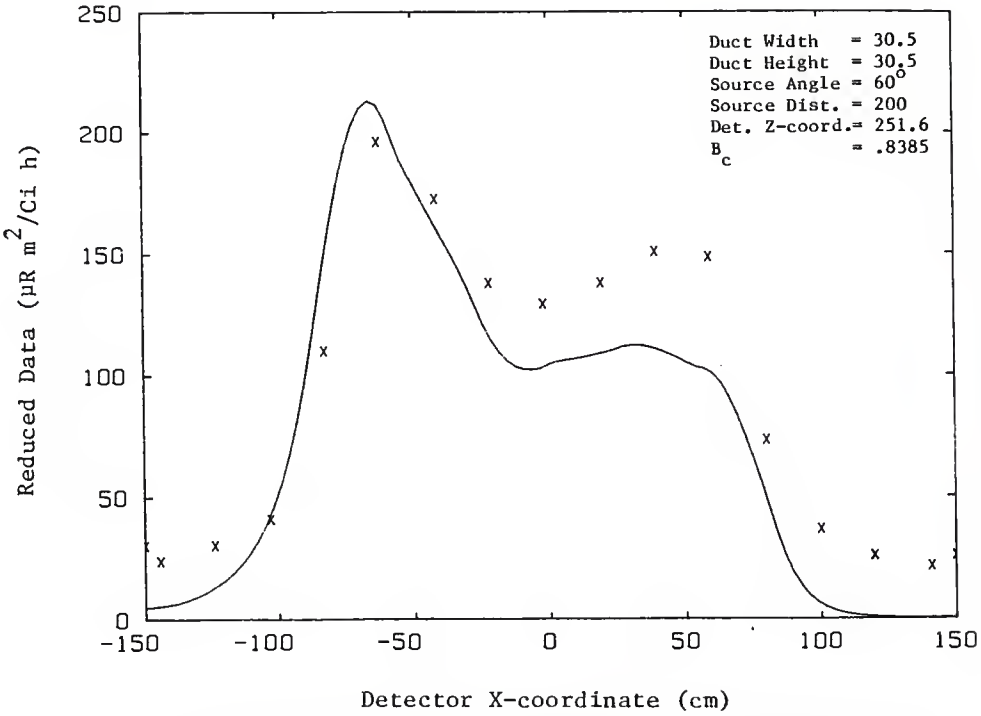

Fig. A.8. Comparison of the duct streaming model to the experimental data. (Solid line = model predicted values, X's = experimental data)

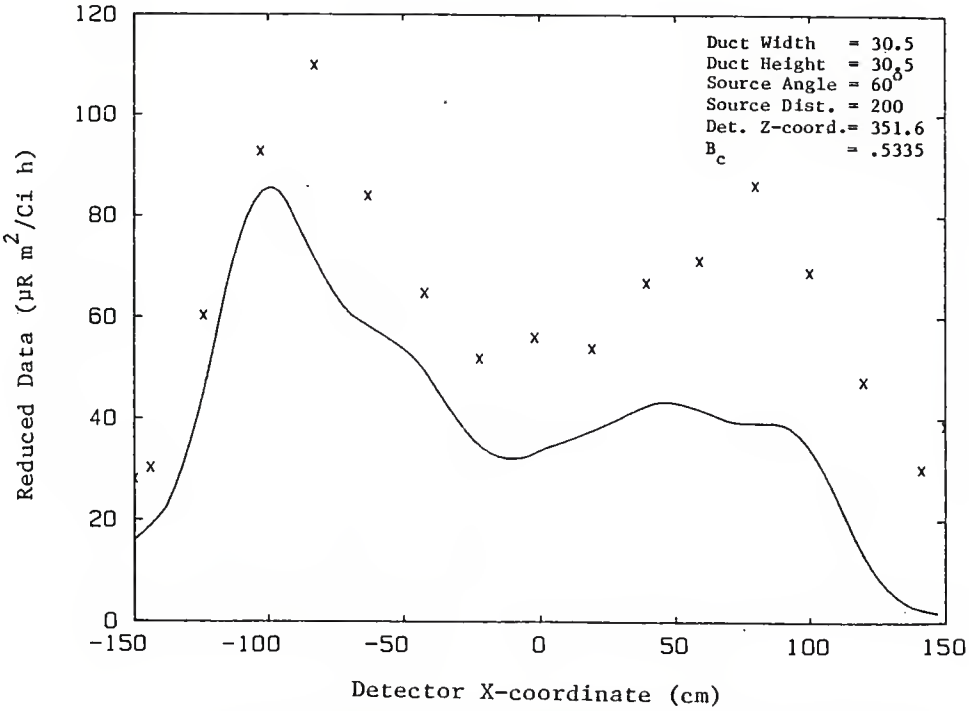

Fig. A.9. Comparison of the duct streaming model to the experimental data. (Solid line = model predicted values, X's = experimental data)

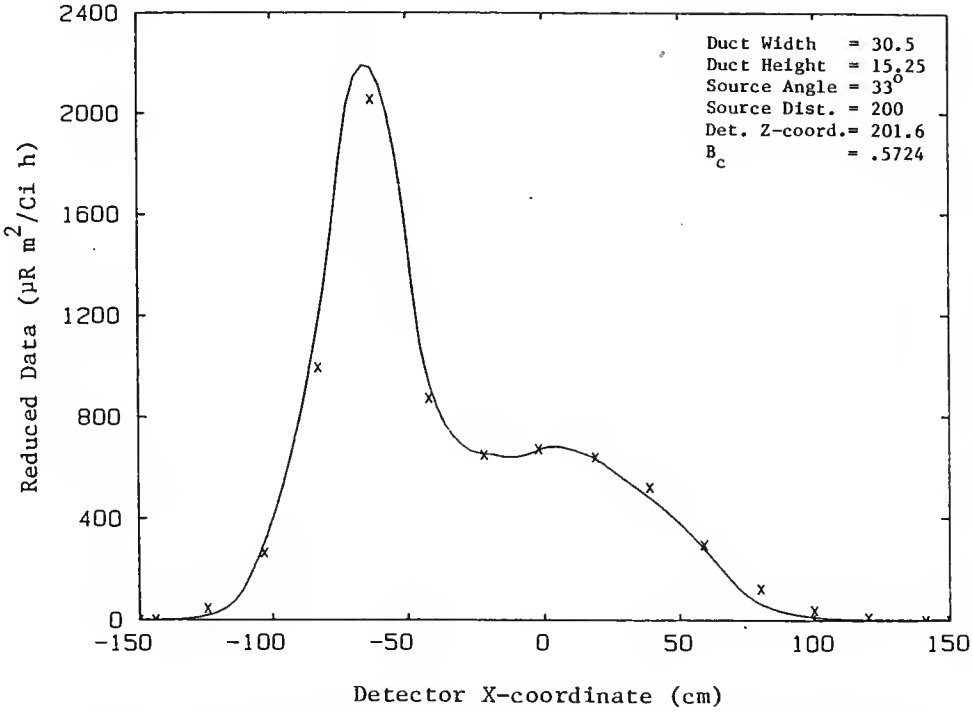

Fig. A.10. Comparison of the duct streaming model to the experimental data. (Solid line = model predicted values, X's = experimental data)

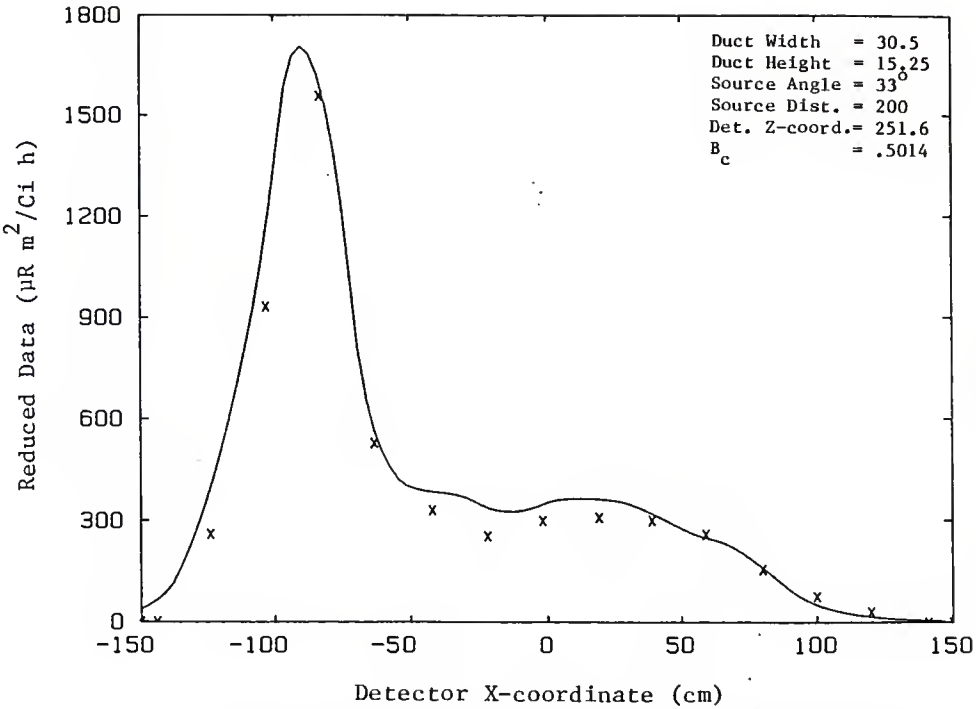

Fig. A.11. Comparison of the duct streaming model to the experimental data. (Solid line = model predicted values, X's = experimental data)

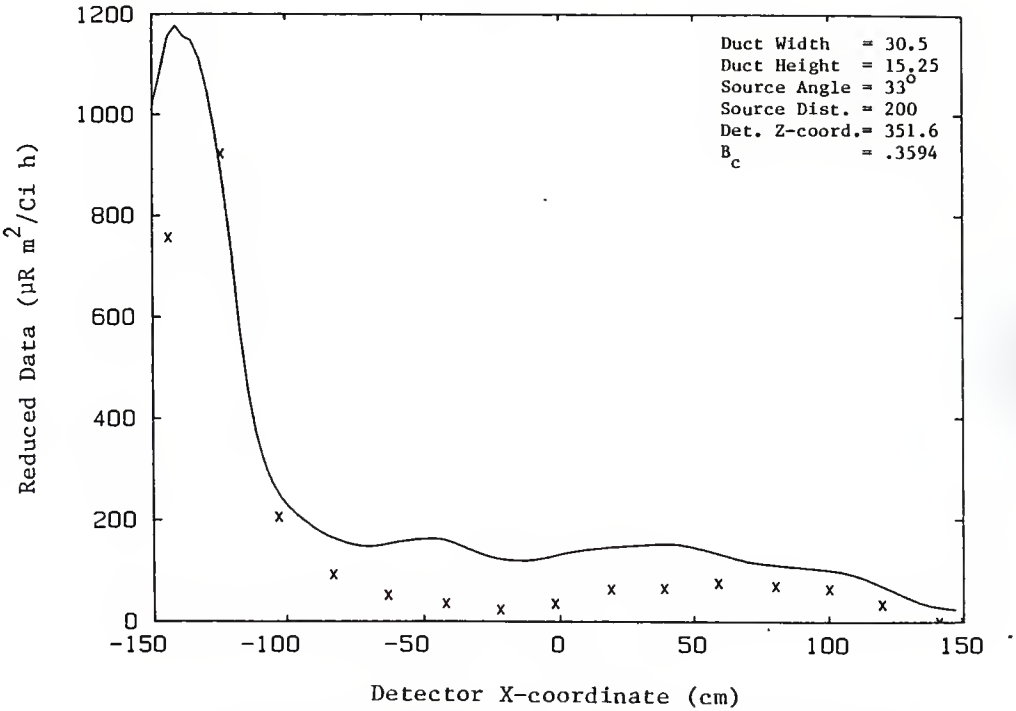

Fig. A.12. Comparison of the duct streaming model to the experimental data. (Solid line = model predicted values, X's = experimental data)

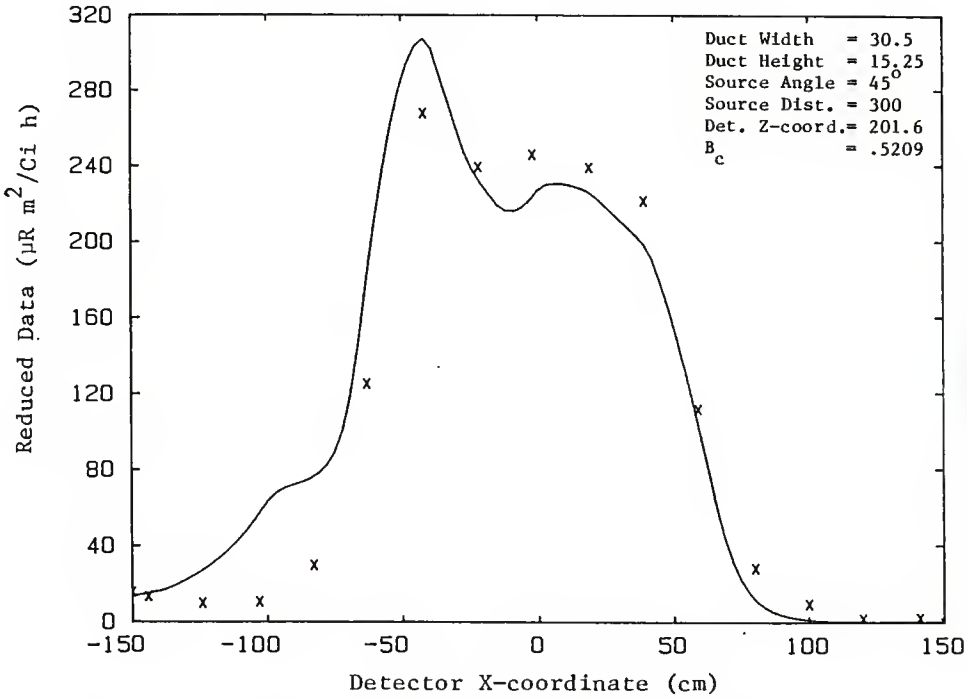

Fig. A.13. Comparison of the duct streaming model to the experimental data. (Solid line = model predicted values, X's = experimental data)

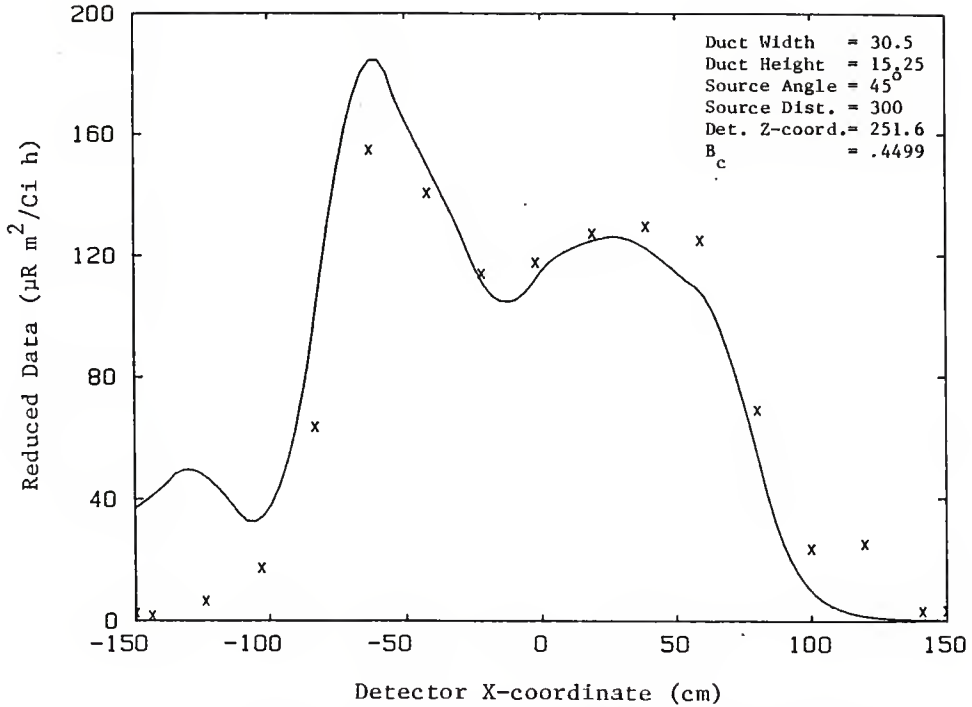

Fig. A.14. Comparison of the duct streaming model to the experimental data. (Solid line = model predicted values, X's = experimental data)

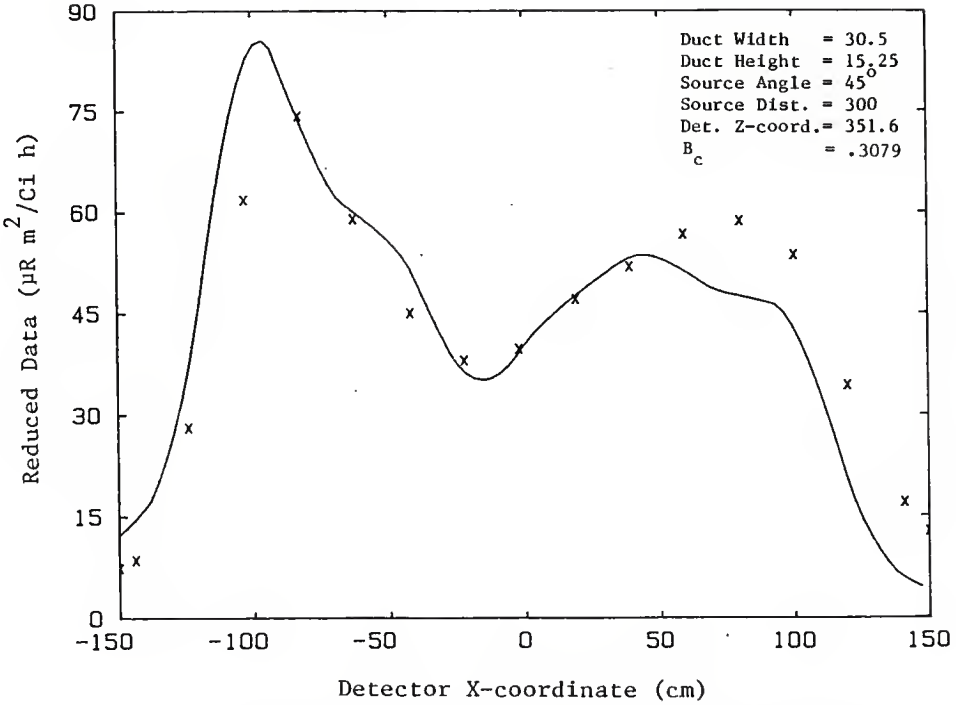

Fig. A.15. Comparison of the duct streaming model to the experimental data. (Solid line = model predicted values, X's = experimental data)

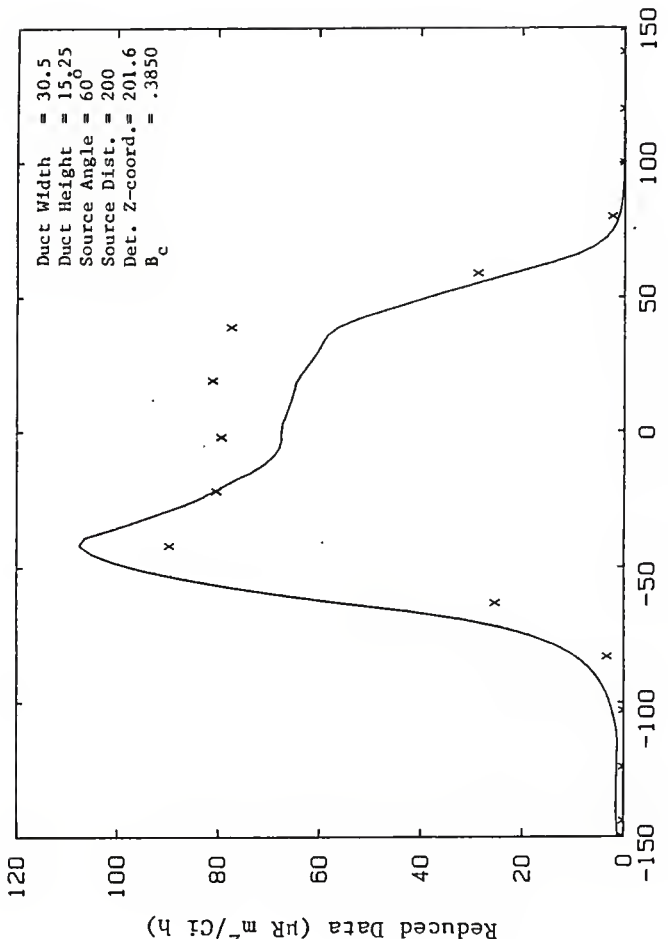

Fig. A.16. Comparison of the duct streaming model to the experimental data. (Solid line = model predicted values, X's = experimental data)

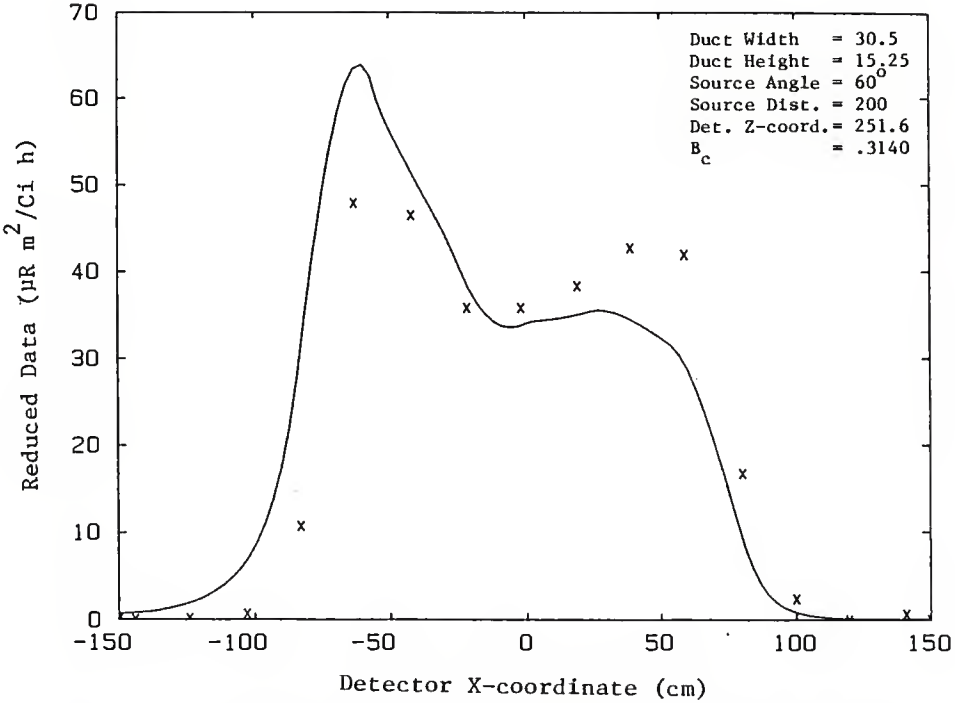

Fig. A.17. Comparison of the duct streaming model to the experimental data. (Solid line = model predicted values, X's = experimental data)

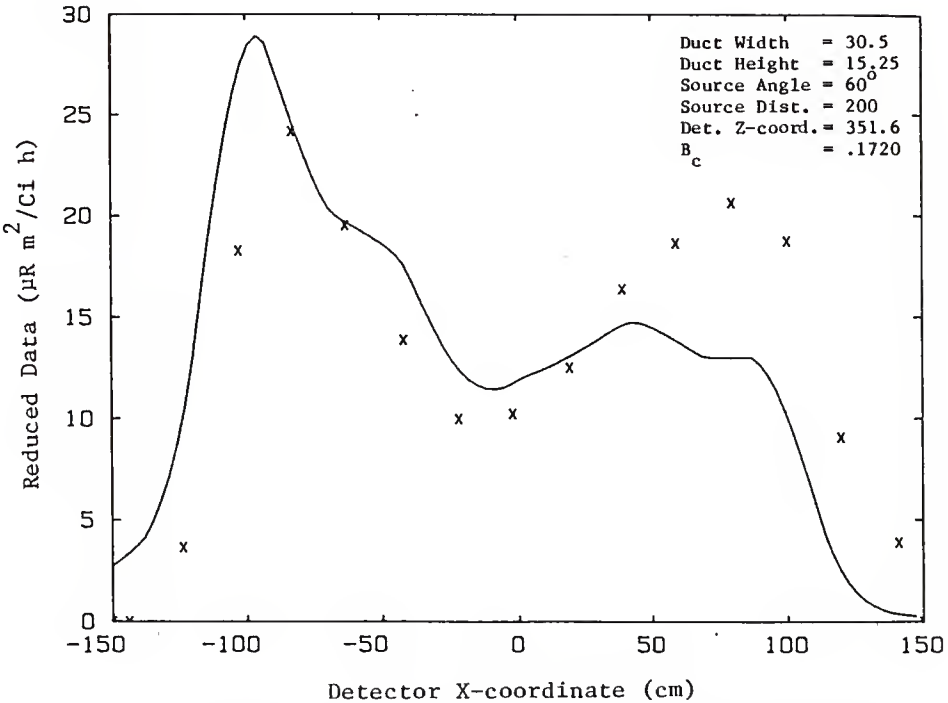

Fig. A.18. Comparison of the duct streaming model to the experimental data. (Solid line = model predicted values, X's = experimental data)

APPENDIX B

Presented in this section is the computer code used to evaluate the single scatter models developed in Chapter 3. This code was written for a Hewlett Packard Model 9816 computer. The code is written in Hewlett Packard BASIC, version 2.1.

The input data consists of the duct dimensions, source location and strength, and the detector distance from the duct wall. These quantities are input interactively at the start of the program execution. The parameters describing the duct, as well as the calculated model components, are then displayed on the screen.

Reduced data values are generated for detector X-coordinates ranging from -150 cm to 150 cm. The calculated values and descriptive data are then stored on a 3½" mini-diskette under a file name input by the user.

Plots of the data were obtained used an earlier written utility plotter code. This plotter code accessed the data files and produced the plots on a Hewlett Packard 7470A Plotter.

```
10    !  ************************************************************************
20    !  *  This program calculates the radiation field resluting from gamma   *
30    !  *  rays streaming through straight rectangular ducts in a concrete    *
40    !  *  wall.  The method of calculation is based upon simplified single   *
50    !  *  scatter scattering points .  The following program was designed    *
60    !  *  to satisfy conditions of the gamma ray streaming experiment con-   *
70    !  *  ducted by the Department of Nuclear Engineering at Kansas State    *
80    !  *  University (see reference 2 of this thesis).                       *
90    !  *                                                                     *
100   !  *  Written by:  Kyle R. Thompson                                      *
110   !  *                                  Spring Semester, 1985              *
120   !  *                                  Department of Nuclear Engineering  *
130   !  *                                  Kansas State University            *
140   !  ************************************************************************
150   !  Definition of variables:
160   !           Dosnl = Array variable representing the dose from the near lip
170   !           Dosfl = Array variable representing the dose from the far lip
180   !           Dosw1 = Array variable representing the dose from wall1
190   !           Dosw2 = Array variable representing the dose from wall2
200   !           Dostw = Array variable representing the dose from the top wall
210   !          Dosdir = Array variable representing the dose from the
220   !                   directly penetrating radiation
230   !      Duct_width = Width of the duct (cm)
240   !     Duct_height = Height of the duct (cm)
250   !     Duct_length = Length of the duct (cm)
260   !    Source_angle = Angle formed by a line from the source to the center
270   !                   of the duct entrance and the Z-axis
280   !     Source_dist = Distance from the source to the center of the duct
290   !                   mouth
300   ! Source_strength = Source strength (Curies)
310   !               N = Gamma ray yield of the source
320   !          Energy = Energy of the source gamma rays (MeV)
330   !     X0,Y0, & Z0 = Source location
340   !     Xd,Yd, & Zd = Detector location
350   !               C = Distance from the back of the duct wall to the
360   !                   detector
370   !      Collimator = Angle of collimation nearest the duct wall (measured
380   !                   from the collimator centerline)
390   !              Bc = Buildup correction factor
400   !  ************************************************************************
410       PRINTER IS 1
420       OPTION BASE 1
430       DEG
440       DIM Dosnl(101),Dosfl(101),Dosw1(101),Dosw2(101),Dostw(101),Dosdir(101)
450       DIM Dostot(101),Xxx(101)
460       COM /Main/ Source_angle,Source_strength,Energy,N,Duct_width,Duct_height
           ,Duct_length,X0,Y0,Z0,Xd,Yd,Zd,Bc,Reduction
470       INPUT "What is the duct width (cm) ?",Duct_width
480       INPUT "What is the duct height (cm) ?",Duct_height
490       INPUT "What is the duct length (cm) ?",Duct_length
500       INPUT "What is the source angle (degrees) ?",Source_angle
510       INPUT "What is the source distance to the duct entrance (cm) ?",Source_
           dist
520       INPUT "What is the Co-60 nominal source strength (Curies) ?",Source_str
           ength
530       N=2
```

```
540       Energy=1.25
550       ! Days since experimental source calibration.
560       INPUT "How days since May 31 was the source used ?",Date
570       XO=Source_dist*SIN(Source_angle)
580       YO=0
590       ZO=-Source_dist*COS(Source_angle)
600       Yd=0
610       INPUT "What is the detector distance from the duct wall (cm) ?",C
620       Zd=C+Duct_length
630       Wall_density=2.2
640   !   ***Determination of horizontal collimator angle nearest the duct wall**
650   !   ****   Collimation angle is different for the different sources.   ****
660       Collimator=5
670       IF Source_strength=.5 THEN Collimator=15
680   !   ****  Determination of actual source strength used in experiment   ****
690       IF Source_strength=10 THEN Source_strength=8.116*EXP(-.000361*(Date-1))
700       IF Source_strength=.5 THEN Source_strength=.4741*EXP(-.000361*(Date-1))
710       Reduction=(Source_dist/100) 2/Source_strength
720 Format:IMAGE 5D,X,4D.3D,X,4D.3D,X,4D.3D,X,4D.3D,X,4D.3D,X,4D.3D,X,4D.3D
730   !   ****                Calculate buildup correction factors            ****
740       IF Duct_height=30.5 THEN
750            Bc=.75+.273/COS(Source_angle)-.305*C/Duct_length
760       ELSE
770            Bc=.991-.232/COS(Source_angle)-.142*C/Duct_length
780       END IF
790       ASSIGN @Road TO 1
800       CALL Prt_info(Collimator,@Road)
810       ASSIGN @Road TO *
820       Source_strength=Source_strength*N*3.7E+10
830   !   ****      Calculate the gamma ray streaming radiation field        ****
840       PRINT
850       PRINT TAB(13);"Values predicted from models (microR m^2/Ci h)"
860       PRINT "  XX      NLip      FLip      Wall1     Wall2     TWall    Direct    To
           tal"
870       PRINT " (cm)"
880       FOR Xd=-150 TO 150 STEP 3
890            I=I+1
900            Xxx(I)=Xd
910            Dosn1(I)=FNNlip
920            Dosf1(I)=FNFlip
930            Dosw1(I)=FNWall1
940            Dosw2(I)=FNWall2
950            Dostw(I)=FNTwall*2
960            Dosdir(I)=FNDir(.10,Collimator)
970            Dostot(I)=Dosn1(I)+Dosf1(I)+Dosw1(I)+Dosw2(I)+Dostw(I)+Dosdir(I)
980            PRINT USING Format;Xd,Dosn1(I),Dosf1(I),Dosw1(I),Dosw2(I),Dostw(I)
           ,Dosdir(I),Dostot(I)
990       NEXT Xd
1000      Source_strength=Source_strength/N/3.7E+10
1010  !   ****                        Smooth and store data                   ****
1020      CALL Smooth(Dosn1(*),Dosf1(*),Dosw1(*),Dosw2(*),Dostw(*),Dosdir(*),Dost
           ot(*),I,Xxx(*),Bc,Collimator)
1030      END
1040  !   ************************************************************************
1050  !   ************             START OF SUBROUTINES              *************
1060  !   ************************************************************************
```

```
1070     DEF FNNlip
1080  !  ************************************************************************
1090  !  ***Subroutine to calculate the dose contribution from the near lip1.***
1100  !  Definition of variables:
1110  !       X,Y,Z = Location of scatter point
1120  !      Alpha1 = Angle between incident photon path and X-axis
1130  !      Alpha2 = Angle between scattered photon path and Z-axis
1140  !          R1 = Distance between source and scatter point
1150  !          R2 = Distance between scatter point and detector
1160  ! Theta_scat = Scatter angle
1170  !       Escat = Energy of the scattered photon (MeV)
1180  !       Klein = Klein-Nishina cross section
1190  !    Response = Dosimetric response function
1200  !          P2 = Exit path length in concrete of the scattered photon
1210  !        Dose = Dose from lip1 ( microR m^2/Ci h)
1220  !  ************************************************************************
1230          COM /Main/ Source_angle,Source_strength,Energy,N,Duct_width,Duct_h
      eight,Duct_length,X0,Y0,Z0,Xd,Yd,Zd,Bc,Reduction
1240          COM /Bup/ K1,K2,K3,K4
1250          IF Xd)=Duct_width/2 THEN RETURN 0
1260          X=Duct_width/2+4
1270          Y=0
1280          Z=4
1290          Alpha1=ATN((Z-Z0)/(X0-X))
1300          Alpha2=ATN((X-Xd)/(Zd-Z))
1310          R1=SQR((X-X0)^2+(Y-Y0)^2+(Z-Z0)^2)
1320          R2=SQR((X-Xd)^2+(Y-Yd)^2+(Z-Zd)^2)
1330          Sd=(X-X0)*(Xd-X)+(Y-Y0)*(Yd-Y)+(Z-Z0)*(Zd-Z)
1340          Theta_scat=ACS(Sd/(R1*R2))
1350          Klein=FNKlein(Energy,Theta_scat,Escat,0)
1360          Response=FNResponse(Escat)
1370          P2=(Duct_length-Z-X/TAN(Alpha2)-Duct_width/TAN(Alpha2)/2)/COS(Alph
      a2)
1380          IF Xd)Duct_width/2 OR P2(0 THEN P2=0
1390          Constant=SIN(Alpha1)*SIN(Alpha2)*EXP(-FNMu(Escat)*P2)*FNBup(Bc,Esc
      at,P2)
1400          Constant=Constant*(1+K1*Escat^K2/(K3*EXP(K4*Escat)-1) 2)
1410          Dose=Duct_height*Source_strength*Response*Klein/(4*PI*R1^2*R2^2*FN
      Mu(Energy)*FNMu(Escat))*Constant*Reduction
1420          RETURN Dose
1430     FNEND  ! **********              End of Subroutine              **********
1440     DEF FNFlip
1450  !  ************************************************************************
1460  !  ***Subroutine to calculate the dose contribution from the far lip2.****
1470  !  Definition of variables:
1480  !       X,Y,Z = Location of scatter point
1490  !      Alpha1 = Angle between incident photon path and X-axis
1500  !      Alpha2 = Angle between scattered photon path and Z-axis
1510  !          R1 = Distance between source and scatter point
1520  !          R2 = Distance between scatter point and detector
1530  ! Theta_scat = Scatter angle
1540  !       Escat = Energy of the scattered photon (MeV)
1550  !       Klein = Klein-Nishina cross section
1560  !    Response = Dosimetric response function
1570  !          P2 = Exit path length in concrete of the scattered photon
1580  !          Mu = Attenuation coefficient in concrete for photons @ Energy
```

```
1590 !        Mus = Attenuation coefficient in concrete for photons @ Escat
1600 !       Dose = Dose from lip2 (microR m^2/Ci h)
1610 ! ************************************************************************
1620         COM /Main/ Source_angle,Source_strength,Energy,N,Duct_width,Duct_h
     eight,Duct_length,X0,Y0,Z0,Xd,Yd,Zd,Bc,Reduction
1630         COM /Bup/ K1,K2,K3,K4
1640         IF Xd(=-Duct_width/2 THEN RETURN 0
1650         X=-Duct_width/2-4
1660         Y=0
1670         Z=4
1680         Alpha1=ATN((Z-Z0)/(X0-X))
1690         Alpha2=ATN((Xd-X)/(Zd-Z))
1700         R1=SQR((X-X0)^2+(Y-Y0)^2+(Z-Z0)^2)
1710         R2=SQR((X-Xd)^2+(Y-Yd)^2+(Z-Zd)^2)
1720         Sd=(X-X0)*(Xd-X)+(Y-Y0)*(Yd-Y)+(Z-Z0)*(Zd-Z)
1730         Theta_scat=ACS(Sd/(R1*R2))
1740         Klein=FNKlein(Energy,Theta_scat,Escat,0)
1750         Response=FNResponse(Escat)
1760         P2=(Duct_length-Z+X/TAN(Alpha2)-Duct_width/TAN(Alpha2)/2)/COS(Alph
     a2)
1770         IF Xd(-Duct_width/2 OR P2(0 THEN P2=0
1780         Mu=FNMu(Energy)
1790         Mus=FNMu(Escat)
1800         Constant=EXP(-Mus*P2)*FNBup(Bc,Escat,P2)
1810         Constant1=SIN(Alpha1)*SIN(Alpha2)/(Mu*Mus)-SIN(Alpha1)*SIN(Alpha2)
     *COS(Alpha1)/(Mus*Mu*COS(Alpha1)+Mu*Mu*SIN(Alpha2))
1820         Constant2=Constant1+SIN(Alpha1)*SIN(Alpha2)/(Mu*Mus)*K1*Escat^K2/(
     K3*EXP(K4*Escat)-1)^2
1830         Constant3=Constant2-SIN(Alpha1)*Mus/(SIN(Alpha2)*Mu)*K1*Escat^K2/(
     Mus/SIN(Alpha2)*(K3*EXP(K4*Escat)-1)-Mu/COS(Alpha1))^2
1840         Constant=Constant*Constant3
1850         Dose=Duct_height*Source_strength*Response*Klein/(4*PI*R1^2*R2^2)*C
     onstant*Reduction
1860         RETURN Dose
1870       FNEND  ! **********              End of Subroutine              **********
1880       DEF FNWall1
1890 ! ************************************************************************
1900 ! ****   Subroutine to calculate the dose contribution from wall1.   ****
1910 ! Definition of variables:
1920 !      X,Y,Z = Location of scatter point
1930 !     Alpha1 = Angle between incident photon path and X-axis
1940 !     Alpha2 = Angle between scattered photon path and Z-axis
1950 !         R1 = Distance between source and scatter point
1960 !         R2 = Distance between scatter point and detector
1970 ! Theta_scat = Scatter angle
1980 !      Escat = Energy of the scattered photon (MeV)
1990 !      Klein = Klein-Nishina cross section
2000 !   Response = Dosimetric response function
2010 !         P2 = Exit path length in concrete of the scattered photon
2020 !         Mu = Attenuation coefficient in concrete for photons @ Energy
2030 !        Mus = Attenuation coefficient in concrete for photons @ Escat
2040 !       Dose = Dose from wall1 (microR m^2/Ci h)
2050 ! ************************************************************************
2060         COM /Main/ Source_angle,Source_strength,Energy,N,Duct_width,Duct_h
     eight,Duct_length,X0,Y0,Z0,Xd,Yd,Zd,Bc,Reduction
2070         COM /Bup/ K1,K2,K3,K4
```

```
2080          IF Xd<=-Duct_width/2 THEN RETURN 0
2090          X=-Duct_width/2
2100          Y=0
2110          Z=Duct_width/TAN(Source_angle)/2
2120          Alpha1=ATN((Z-Z0)/(X0-X))
2130          Alpha2=ATN((Xd-X)/(Zd-Z))
2140          R1=SQR((X-X0)^2+(Y-Y0)^2+(Z-Z0)^2)
2150          R2=SQR((X-Xd)^2+(Y-Yd)^2+(Z-Zd)^2)
2160          Sd=(X-X0)*(Xd-X)+(Y-Y0)*(Yd-Y)+(Z-Z0)*(Zd-Z)
2170          Theta_scat=ACS(Sd/(R1*R2))
2180          Klein=FNKlein(Energy,Theta_scat,Escat,0)
2190          Response=FNResponse(Escat)
2200          P2=(Duct_length-Z-Duct_width/TAN(Alpha2))/COS(Alpha2)
2210          IF Xd<-Duct_width/2 OR P2<0 THEN P2=0
2220          Mu=FNMu(Energy)
2230          Mus=FNMu(Escat)
2240          Constant=EXP(-Mus*P2)*FNBup(Bc,Escat,P2)*TAN(Alpha1)*Duct_width
2250          Constant1=SIN(Alpha2)*COS(Alpha1)/(Mus*COS(Alpha1)+Mu*SIN(Alpha2))
2260          Constant2=Constant1+Mus/SIN(Alpha2)*K1*Escat^K2/(Mus/SIN(Alpha2)*(
         K3*EXP(K4*Escat)-1)-Mu/COS(Alpha1))^2
2270          Constant=Constant*Constant2
2280          Dose=Duct_height*Source_strength*Response*Klein/(4*PI*R1^2*R2^2)*C
         onstant*Reduction
2290          RETURN Dose
2300        FNEND  ! **********              End of Subroutine              **********
2310        DEF FNWall2
2320    ! ************************************************************************
2330    ! ****   Subroutine to calculate the dose contribution from wall2.   ****
2340    ! Definition of variables:
2350    !      X,Y,Z = Location of scatter point
2360    !     Alpha1 = Angle between incident photon path and X-axis
2370    !     Alpha2 = Angle between scattered photon path and Z-axis
2380    !         R1 = Distance between source and scatter point
2390    !         R2 = Distance between scatter point and detector
2400    ! Theta_scat = Scatter angle
2410    !      Escat = Energy of the scattered photon  MeV
2420    !      Klein = Klein-Nishina cross section
2430    !   Response = Dosimetric response function
2440    !         P2 = Exit path length in concrete of the scattered photon
2450    !         Mu = Attenuation coefficient in concrete for photons @ Energy
2460    !        Mus = Attenuation coefficient in concrete for photons @ Escat
2470    !       Dose = Dose from wall2 (microR m^2/Ci h)
2480    ! ************************************************************************
2490          COM /Main/ Source_angle,Source_strength,Energy,N,Duct_width,Duct_h
         eight,Duct_length,X0,Y0,Z0,Xd,Yd,Zd,Bc,Reduction
2500          COM /Bup/ K1,K2,K3,K4
2510          IF Xd<=-Duct_width/2 THEN RETURN 0
2520          X=-Duct_width/2
2530          Y=0
2540          Z=Duct_width/TAN(Source_angle)
2550          Alpha1=ATN((Z-Z0)/(X0-X))
2560          Alpha2=ATN((Xd-X)/(Zd-Z))
2570          R1=SQR((X-X0)^2+(Y-Y0)^2+(Z-Z0)^2)
2580          R2=SQR((X-Xd)^2+(Y-Yd)^2+(Z-Zd)^2)
2590          Sd=(X-X0)*(Xd-X)+(Y-Y0)*(Yd-Y)+(Z-Z0)*(Zd-Z)
2600          Theta_scat=ACS(Sd/(R1*R2))
```

```
2610          Klein=FNKlein(Energy,Theta_scat,Escat,0)
2620          Response=FNResponse(Escat)
2630          P2=(Duct_length-Z-Duct_width/TAN(Alpha2))/COS(Alpha2)
2640          IF Xd(-Duct_width/2 OR P2(0 THEN P2=0
2650          Mu=FNMu(Energy)
2660          Mus=FNMu(Escat)
2670          Cc=Duct_height*Source_strength*Response*Klein/(4*PI*R1^2*R2^2)*EXP
         (-Mus*P2)*FNBup(Bc,Escat,P2)
2680          Aa=-Mu/COS(Alpha1)-Mus/SIN(Alpha2)
2690          Bb=K1*Escat^K2*Mus/SIN(Alpha2)
2700          Dd=Mus/SIN(Alpha2)*K3*EXP(K4*Escat)
2710          Part1=(FNExp((Duct_length/TAN(Alpha1)-3*Duct_width/2)*Aa)-1)/Aa
2720          Part2=Bb/(Dd+Aa)*(FNExp((Duct_length/TAN(Alpha1)-3*Duct_width/2)*(
         Dd+Aa))*(Duct_length/TAN(Alpha1)-3*Duct_width/2-1/(Dd+Aa))+1/(Dd+Aa))
2730          Dose=Cc*SIN(Alpha1)/Mu*(Part1+Part2)*Reduction
2740          RETURN Dose
2750      FNEND  ! **********              End of Subroutine              **********
2760      DEF FNTwall
2770    ! ************************************************************************
2780    ! ***Subroutine to calculate the dose contribution from the top wall3.***
2790    ! Definition of variables:
2800    !      X,Y,Z = Location of scatter point
2810    !     Alpha1 = Angle between incident photon path and X-axis
2820    !     Alpha2 = Angle between scattered photon path and Z-axis
2830    !      Beta1 = Angle between the X-axis and a line from the source to the
2840    !              edge of near duct lip (lip1)
2850    !      Beta2 = Angle between the Y-axis and a line from the source to the
2860    !              top lip of the duct
2870    !         R1 = Distance between source and scatter point
2880    !         R2 = Distance between scatter point and detector
2890    ! Theta_scat = Scatter angle
2900    !      Escat = Energy of the scattered photon 'MeV
2910    !      Klein = Klein-Nishina cross section
2920    !   Response = Dosimetric response function
2930    !         P2 = Exit path length in concrete of the scattered photon
2940    !         Mu = Attenuation coefficient in concrete for photons @ Energy
2950    !        Mus = Attenuation coefficient in concrete for photons @ Escat
2960    !       Dose = Dose from wall3 [microR m^2/Ci h]
2970    ! ************************************************************************
2980          COM /Main/ Source_angle,Source_strength,Energy,N,Duct_width,Duct_h
         eight,Duct_length,X0,Y0,Z0,Xd,Yd,Zd,Bc,Reduction
2990          COM /Bup/ K1,K2,K3,K4
3000          IF Yd)=Duct_height/2 THEN RETURN 0
3010          X=0
3020          Y=Duct_height/2
3030          Z=0
3040          R1=SQR((X-X0)^2+(Y-Y0)^2+(Z-Z0)^2)
3050          R2=SQR((X-Xd)^2+(Y-Yd)^2+(Z-Zd)^2)
3060          Sd=(X-X0)*(Xd-X)+(Y-Y0)*(Yd-Y)+(Z-Z0)*(Zd-Z)
3070          Alpha1=ASN((Y-Y0)/R1)
3080          Alpha2=ASN((Y-Yd)/R2)
3090          Beta1=ATN(-Z0/(X0-Duct_width/2))
3100          Beta2=ATN(-Z0*2/Duct_height)
3110          Theta_scat=ACS(Sd/(R1*R2))
3120          Klein=FNKlein(Energy,Theta_scat,Escat,0)
3130          Response=FNResponse(Escat)
```

```
3140          Gamma=ATN(ABS(Xd)/Zd)
3150          IF Gamma=0 THEN
3160               P2=0
3170          ELSE
3180               P2=(Duct_length/COS(Gamma)-Duct_width/SIN(Gamma)/2)/COS(Alpha
        2)
3190          END IF
3200          IF P2<0 THEN P2=0
3210          Mu=FNMu(Energy)
3220          Mus=FNMu(Escat)
3230          Bb=Duct_width*TAN(Beta1)/2
3240          Cc=Duct_width*Source_strength*Response*Klein/(4*PI*R1^2*R2^2)*EXP(
        -Mus*P2)*FNBup(Bc,Escat,P2)
3250          Dd=K1*Escat^K2*Mus/SIN(Alpha2)
3260          Ee=Mus/SIN(Alpha2)*K3*EXP(K4*Escat)
3270          Ff=-Mu/SIN(Alpha1)-Mus/SIN(Alpha2)
3280          Part1=(FNExp(Bb*TAN(Beta2)*Ff)-1)/(TAN(Beta2)*Ff*Ff)-Bb/Ff
3290          Part2=Dd/(Ee+Ff) 2*(FNExp(Bb*TAN(Beta2)*(Ee+Ff))*(Bb-2/(TAN(Beta2)
        *(Ee+Ff)))+Bb+2/(TAN(Beta2)*(Ee+Ff)))
3300          Dose=Cc*(Part1+Part2)*Reduction
3310          RETURN Dose
3320     FNEND  ! **********              End of Subroutine              **********
3330     DEF FNDir(Dbc,Collimator)
3340   ! ******************************************************************************
3350   !Subroutine to calculate the dose contribution from the direct penetration.
3360   !  Definition of variables:
3370   !    Alpha = Angle formed between the X-axis and the photon path
3380   !        R = Distance between source and detector
3390   ! Response = Dosimetric response function
3400   !   Dapath = Path length traveled in concrete by the photons with the duct
3410   !            absent
3420   !     Path = Path length traveled in concrete by the photons with the duct
3430   !            present
3440   !       Mu = Attenuation coefficient in concrete for photons @ Energy
3450   !      Dbc = Buildup correction factor for the direct radiation component
3460   !     Dose = Dose [microR m^2/Ci h]
3470   ! ******************************************************************************
3480          COM /Main/ Source_angle,Source_strength,Energy,N,Duct_width,Duct_h
        eight,Duct_length,X0,Y0,Z0,Xd,Yd,Zd,Bc,Reduction
3490          Test=ATN((Zd-Z0)/(X0-Xd))
3500   ! ****     Test to see if direct beam is within collimated width      ****
3510          IF Test<(90-Source_angle+Collimator) THEN RETURN 0
3520          R=SQR((X0-Xd)^2+(Y0-Yd)^2+(Z0-Zd)^2)
3530          IF X0>Xd THEN
3540               Alpha=ATN((Zd-Z0)/(X0-Xd))
3550               X=X0+Z0/TAN(Alpha)
3560          ELSE
3570               RETURN 0
3580          END IF
3590          Dapath=Duct_length/SIN(Alpha)
3600          Z=(X-Duct_width/2)*TAN(Alpha)
3610          IF Z>=Duct_length THEN
3620               RETURN 0
3630          END IF
3640          Path1=Z/SIN(Alpha)
3650          IF X<=Duct_width/2 THEN Path1=0
```

```
3660          Z1=(X+Duct_width/2)*TAN(Alpha)
3670          Path2=(Duct_length-Z1)/SIN(Alpha)
3680          IF Z1>=Duct_length THEN Path2=0
3690          Path=Path1+Path2
3700          Mu=FNMu(Energy)
3710          Dose=EXP(-Mu*Path)*FNBup(Dbc,1.25,Path)-EXP(-Mu*Dapath)*FNBup(Dbc,
         1.25,Path)
3720          Dose=Dose*Source_strength*FNResponse(1.25)/(4*PI*R*R)*Reduction
3730          RETURN Dose
3740      FNEND  ! **********              End of Subroutine              **********
3750      SUB Prt_info(Collimator,@Road)
3760    ! ************************************************************************
3770    ! ****      Subroutine to print duct configuration information.      ****
3780    ! ************************************************************************
3790          COM /Main/ Source_angle,Source_strength,Energy,N,Duct_width,Duct_h
         eight,Duct_length,X0,Y0,Z0,Xd,Yd,Zd,Bc,Reduction
3800          ALLOCATE Data$ 256
3810          ASSIGN @Line TO BUFFER  256
3820          OUTPUT @Line USING "20X,""***** Duct Configuration *******"
3830          ENTER @Line;Data$
3840          OUTPUT @Road;Data$
3850          OUTPUT @Line USING """Duct Width = "",36X,4D.4D,2X,""cm""";Duct_wi
         dth
3860          ENTER @Line;Data$
3870          OUTPUT @Road;Data$
3880          OUTPUT @Line USING """Duct Height = "",35X,4D.4D,2X,""cm""";Duct_h
         eight
3890          ENTER @Line;Data$
3900          OUTPUT @Road;Data$
3910          OUTPUT @Line USING """Duct Length = "",35X,4D.4D,2X,""cm""";Duct_l
         ength
3920          ENTER @Line;Data$
3930          OUTPUT @Road;Data$
3940          OUTPUT @Line USING """Source Elevation = "",30X,4D.4D,2X,""cm""";Y
         0
3950          ENTER @Line;Data$
3960          OUTPUT @Road;Data$
3970          OUTPUT @Line USING """Source Angle = "",34X,4D.4D,2X,""degrees""";
         Source_angle
3980          ENTER @Line;Data$
3990          OUTPUT @Road;Data$
4000          OUTPUT @Line USING """Source Distance = "",31X,4D.4D,2X,""cm""";X0
         /SIN(Source_angle)
4010          ENTER @Line;Data$
4020          OUTPUT @Road;Data$
4030          OUTPUT @Line USING """Detector Elevation = "",28X,4D.4D,2X,""cm"""
         ;Yd
4040          ENTER @Line;Data$
4050          OUTPUT @Road;Data$
4060          OUTPUT @Line USING """Detector Distance from Wall = "",19X,4D.4D,2
         X,""cm""";Zd-Duct_length
4070          ENTER @Line;Data$
4080          OUTPUT @Road;Data$
4090          OUTPUT @Line USING """Collimator Angle = "",30X,4D.4D,2X,""degrees
         """;Collimator
4100          ENTER @Line;Data$
```

```
4110          OUTPUT @Road;Data$
4120          OUTPUT @Line USING "21X,""Cobalt-60 Gamma Ray Source"""
4130          ENTER @Line;Data$
4140          OUTPUT @Road;Data$
4150          OUTPUT @Line USING """Source Strength = "",31X,4D.4D,2X,""Curies""
          ";Source_strength
4160          ENTER @Line;Data$
4170          OUTPUT @Road;Data$
4180          OUTPUT @Line USING """Gamma Ray Yield of the Source = "",17X,4D.4D
          ";N
4190          ENTER @Line;Data$
4200          OUTPUT @Road;Data$
4210          OUTPUT @Line USING """Energy of the Gamma Ray (average) = "",13X,4
          D.4D,2X,""MeV""";Energy
4220          ENTER @Line;Data$
4230          OUTPUT @Road;Data$
4240          OUTPUT @Line USING """Buildup Correction Factor = "",21X,4D.4D,2X"
          ;Bc
4250          ENTER @Line;Data$
4260          OUTPUT @Road;Data$
4270          OUTPUT @Line USING """Reduction Factor = "",30X,4D.4D,2X,""m 2/Cur
          ie""";Reduction
4280          ENTER @Line;Data$
4290          OUTPUT @Road;Data$
4300          ASSIGN @Line TO *
4310          DEALLOCATE Data$
4320      SUBEND ! **********              End of Subroutine              **********
4330      SUB Smooth(Dosnl(*),Dosfl(*),Dosw1(*),Dosw2(*),Dostw(*),Dosdir(*),Dosto
          t(*),I,Xxx(*),Bc,Collimator)
4340    ! ********************************************************************
4350    ! ****            Subroutine to Smooth and Store the Data           ****
4360    ! ********************************************************************
4370    ! ****              Start of data smoothing section                 ****
4380    ! ********************************************************************
4390          ALLOCATE Sm1(I)
4400          Step=ABS(Xxx(1)-Xxx(2))    ! Distance between data values
4410          Dstep=INT(12/Step)
4420          FOR Ii=1 TO I
4430               IF Ii<=Dstep THEN
4440                    A=1-Ii
4450               ELSE
4460                    A=-Dstep
4470               END IF
4480               IF Ii+Dstep>=I THEN
4490                    Bb=I-Ii
4500               ELSE
4510                    Bb=Dstep
4520               END IF
4530               Summ1=0
4540               Summm1=0
4550               FOR Jj=A TO Bb
4560                    Summ1=Summ1+1
4570                    Summm1=Summm1+Dostot(Ii+Jj)
4580               NEXT Jj
4590               Sm1(Ii)=Summm1/Summ1
4600          NEXT Ii
```

```
4610  !  ************************************************************************
4620  !  ****                  Start of data storage section                 ****
4630  !  ************************************************************************
4640          DISP "PRESS CONTINUE TO STORE DATA"
4650          PAUSE
4660          ALLOCATE Data$(3) 256
4670          INPUT "WHAT IS THE NAME OF YOUR ASCII FILE",Name$
4680 I0:      IMAGE 18X,"Values predicted from models (microR m^2/Ci h)"
4690 I1:      IMAGE "  XX      NLip      FLip      Wall1     Wall2     TWall    Direct
             Total  Smoothed"
4700 I3:      IMAGE " (cm)"
4710 Format:  IMAGE 5D,X,4D.3D,X,4D.3D,X,4D.3D,X,4D.3D,X,4D.3D,X,4D.3D,X,4D.3D,X
      ,4D.3D
4720          ASSIGN @Buf TO BUFFER  256
4730          CREATE ASCII Name$,I/3+22
4740          ASSIGN @Path TO Name$
4750          CALL Prt_info(Collimator,@Path)
4760          OUTPUT @Path;"NUMBER OF DATA POINTS IS "&VAL$(I)
4770          OUTPUT @Buf USING I0
4780          ENTER @Buf;Data$(1)
4790          OUTPUT @Path;Data$(1)
4800          OUTPUT @Buf USING I1
4810          ENTER @Buf;Data$(1)
4820          OUTPUT @Path;Data$(1)
4830          FOR J=1 TO I
4840               Counter=Counter+1
4850               OUTPUT @Buf USING Format;Xxx(J),Dosn1(J),Dosf1(J),Dosw1(J),Do
      sw2(J),Dostw(J),Dosdir(J),Dostot(J),Sm1(J)
4860               ENTER @Buf;Data$(Counter)
4870               IF Counter=3 THEN
4880                    OUTPUT @Path;Data$(1),Data$(2),Data$(3)
4890                    Counter=0
4900               END IF
4910          NEXT J
4920          FOR K=1 TO Counter
4930               OUTPUT @Path;Data$(K)
4940          NEXT K
4950          ASSIGN @Path TO *
4960          ASSIGN @Buf TO *
4970     SUBEND ! **********            End of Subroutine            **********
4980     DEF FNKlein(Energy,Theta_scat,Escat,Opt)
4990  !  ************************************************************************
5000  !  ****   Subroutine to calculate the Klein-Nishina cross section.    ****
5010  !  Definition of variables:
5020  !      Energy = Energy of incident photon (MeV)
5030  !       Escat = Energy of scatter photon (MeV)
5040  ! Theta_scat = Scatter angle  degrees
5050  !         Opt = Option variable
5060  !               Opt=0 --> Regular Klein-Nishina Cross Section
5070  !               Opt=1 --> Energy Klein-Nishina Cross Section
5080  !       Klein = Value for the Klein-Nishina Cross Section
5090  !  ************************************************************************
5100          Escat=Energy/(1+Energy/.511*(1-COS(Theta_scat)))
5110          P=Escat/Energy
5120          Klein=.01196*P*(1+P*P-P*(1-COS(Theta_scat)^2))*2.2
5130          IF Opt THEN
```

```
5140              RETURN Klein*P/(.01196*2.2)*.5*(2.818E-13)^2
5150          ELSE
5160              RETURN Klein
5170          END IF
5180      FNEND  ! **********              End of Subroutine              **********
5190      DEF FNBup(Bc,Energy,Path)
5200   !  ************************************************************************
5210   !  ****          Subroutine to calculate the buildup factor.          ****
5220   !  Definition of variables:
5230   !               Bc = Buildup Correction Factor
5240   !           Energy = Energy of photon  MeV
5250   !             Path = Path length photon travels (cm)
5260   !           Lambda = Number of mean free paths traveled by the photon
5270   ! K1,K2,K3, & K4 = Constants used in the buildup factor formula
5280   !  ************************************************************************
5290          COM /Bup/ K1,K2,K3,K4
5300          Lambda=Path*FNMu(Energy)
5310          K1=1.2858*Bc
5320          K2=-.456
5330          K3=.09739
5340          K4=-.8319
5350          RETURN (1+Lambda*K1*Energy^K2*EXP(Lambda*K3*EXP(K4*Energy)))
5360      FNEND  ! **********              End of Subroutine              **********
5370      DEF FNMu(Energy)
5380   !  ************************************************************************
5390   !  ****   Subroutine to calculate the total attenuation coefficient.  ****
5400   !  Definition of variables:
5410   ! Energy = Energy of the photon (MeV)
5420   !  ************************************************************************
5430          RETURN 2.2*.06381*Energy^(-.41851)
5440      FNEND  ! **********              End of Subroutine              **********
5450      DEF FNResponse(Energy)
5460   !  ************************************************************************
5470   !  ****   Subroutine to calculate the dosimetric response function.   ****
5480   !  Definition of variables:
5490   ! Energy = Energy of the photon (MeV)
5500   !  ************************************************************************
5510          RETURN (.01933+.04397*Energy-.05492*Energy^2+.01889*Energy^3)*Ener
       gy*66.04
5520      FNEND  ! **********              End of Subroutine              **********
5530      DEF FNExp(Arg)
5540   !  ************************************************************************
5550   !  *Subroutine to evaluate exponentials with arguments of large magnitude*
5560   !  ************************************************************************
5570          IF ABS(Arg)<700 THEN RETURN EXP(Arg)
5580          IF Arg<0 THEN RETURN 0
5590          RETURN 1.E+300
5600      FNEND  ! **********              End of Subroutine              **********
```

MODELING OF GAMMA RAYS STREAMING THROUGH STRAIGHT RECTANGULAR DUCTS

by

KYLE RICHARD THOMPSON

B. S., Kansas State University, 1983

AN ABSTRACT OF A MASTER'S THESIS

submitted in partial fulfillment of the

requirements for the degree

MASTER OF SCIENCE

Department of Nuclear Engineering

KANSAS STATE UNIVERSITY
Manhattan, Kansas

1985

ABSTRACT

A common problem encountered in radiation shielding is to determine the effect of penetrations through a shield. Current approaches to this duct streaming problem usually involve large computer codes based on Monte Carlo and/or albedo techniques. Often these large codes provide an accuracy (at considerable expense) not needed for many preliminary shielding analyses, and a need for simpler methods to analyze gamma rays streaming through ducts is apparent.

Simple approximate models were developed in this study to describe the spatial variation in the radiation field transmitted through a straight rectangular duct that is obliquely illuminated by gamma photons. These models take into account single and multiple scattering from the duct walls, as well as direct penetration by the photons. It was found that the gamma-ray streaming could be adequately described by considering only the directly penetrating photons and photons that scatter in the lips at the duct entrance and in the duct walls. Two techniques are presented for modeling the contribution of photons reflected once from the duct walls, namely a method based on the use of an empirical albedo formula and a method in which scattering volumes in the duct walls are represented by single effective scattering points.

The composite model was compared to experimental benchmark streaming data both to test the validity and to evaluate an empirical correction factor incorporated into the model. These comparisons showed that the simple models can provide a suitable description of the radiation fields resulting from gamma rays streaming through straight rectangular ducts, and are appropriate for use in preliminary shielding and design calculations.